Grant Agreement No: 227579

EuCARD

European Coordination for Accelerator Research and Development

Seventh Framework Programme, Capacities Specific Programme, Research Infrastructures,
Combination of Collaborative Project and Coordination and Support Action

DELIVERABLE REPORT

DIPOLE MODEL TEST WITH ONE SUPERCONDUCTING COIL; RESULTS ANALYSED

PART I: DESIGN REPORT FOR THE DIPOLE MAGNET

DELIVERABLE: D7.3.1 (PART I)

Document identifier:	EuCARD-Del-D7.3.1.a-v1.0
Due date of deliverable:	End of Month 48
Report release date:	31/05/2013
Work package:	WP7: HFM: Superconducting High Field Magnets for higher luminosities and energies
Lead beneficiary:	CERN/CEA
Document status:	Final

Abstract:

This report is the Part I of the deliverable report 7.3.1 “Dipole model test with one superconducting coil; results analysed”. The four parts of the deliverable report will be joined into one single document at a later date.

The EuCARD-HFM task aims at realizing a 13 Tesla dipole magnet with an aperture of 100 mm, which is a challenging step towards very high field accelerator magnets. This dipole, utilizing Nb_3Sn superconductor, will be used to upgrade the Fresca test facility at CERN. It is known as FRESCA2 magnet.

This report lists the project inputs and constraints. It describes the four-year process of conceptual and engineering design of the dipole and its mechanical structure. It justifies the technical choices that have been made on the base of quantitative arguments and experimental results.

The research presented here has been supported by the European FP7 EuCARD program (grant agreement: 227579).

The European Coordination for Accelerator Research and Development (EuCARD) is a project co-funded by the European Commission in its 7th Framework Programme under the Grant Agreement no 227579. EuCARD began in April 2009 and will run for 4 years.

Delivery Slip

	Name	Partner	Date
Authored by	Edited by: Pierre Manil Magnet Design Working Group: B. Baudouy, C. Berriaud, L. Bottura, S. Caspi, S. Clément, M. Devaux, M. Durante, P. Fazilleau, P. Ferracin, P. Fessia, J-E Muñoz Garcia, R. Gauthier, F. Kircher, P. Manil, A. Milanese, J-F. Millot, L. Oberli, J-C Perez, S. Pietrowicz, J-M Rifflet, G. de Rijk, F. Rondeaux, E. Todesco	CEA/CERN	31/05/13
Reviewed by	G. de Rijk, J.-M. Rifflet	CERN/CEA	03/06/13
Approved by WP Coordinator	G. de Rijk	CERN	04/06/13
Approved by Project coordinator	Jean-Pierre Koutchouk		dd/mm/yy

Content

Executive summary

The EuCARD-HFM task aims at realizing a 13 Tesla dipole magnet with an aperture of 100 mm, which is a challenging step towards very high field accelerator magnets. This dipole, utilizing Nb_3Sn superconductor, will be used to upgrade the Fresca test facility at CERN. It is known as FRESCA2 magnet.

This report lists the project inputs and constraints. It describes the four-year process of conceptual and engineering design of the dipole and its mechanical structure. It justifies the technical choices that have been made on the base of quantitative arguments and experimental results.

The research presented here has been supported by the European FP7 EuCARD program: http://cern.ch/eucard (grant Agreement: 227579).

Introduction

The LHC is at present employing the highest field accelerator magnets that exist. This generation of magnets is based on Nb-Ti conductors, which poses a practical field limit of about 10 Tesla (T). To construct accelerator magnets with a higher field, other conductors are needed with higher critical fields. Nb_3Sn is today the right candidate to meet those objectives, because of its superconducting properties and its industrial availability. However, the usage of Nb_3Sn in practical coils is non-trivial due to the brittle nature of this A15 intermetallic compound and to its strain-sensitivity after reaction[1].

For this, a High Field Magnet (HFM) R&D program was started in Europe in 2004 in the framework of FP6-CARE-NED. The idea of NED (Next European Dipole) was to develop the basic technologies for such a new type of magnet. The first application was thought to be to upgrade the cable test station at CERN with a magnet that provides a background field above 12 T. In the NED program, conductor, insulation, cooling schemes and design concepts were developed. In 2009 NED was succeeded by FP7-EuCARD-WP7-HFM with as aim to build: a 13 T Nb_3Sn dipole, a 6 T High Temperature Superconductor (HTS) insert, a HTS superconductor link prototype and a Nb_3Sn helical undulator. The 13 T dipole is intended to be used for upgrading the CERN cable test facility Fresca, hence the name of the magnet, FRESCA2. For the qualification of the superconducting cables for the LHC luminosity upgrade and possible future accelerators (like High Energy LHC, the HE-LHC) a cable test facility is needed where the magnet can provide a background field on the cable of at least 13 T. It would be an advantage if the background field could reach 15 T for special measurements. Such a test facility magnet needs a large bore to allow for a cable sample holder for high current cables. The aperture requirement for FRESCA2 magnet was thus fixed at 100 mm clear bore. Twelve institutes, universities and industrial firms form the FP7-EuCARD-WP7-HFM collaboration. The actual construction of FRESCA2 magnet is jointly done by CEA-Saclay and CERN. All in all, FRESCA2 specification is for a very ambitious dipole magnet, which, once build and working at 15 T, will constitute a new performance level for dipole magnets.

The end of the EuCARD contract in July 2013 does not end the project as the collaborating institutes are determined to complete the magnet. Thus the work will continue until completion in a different collaborating framework.

This report focuses on the design of the FRESCA2 Nb_3Sn dipole magnet and its support structure. Design of the HTS insert is reported separately [0.1].

[1] The reaction is a thermal treatment at high temperature (around 650°C) which aims at forming the superconducting Nb_3Sn intermetallic compound from its precursors. In that case, the coil is wound before the strand has become fragile because of the reaction (this is the “wind-and-react” route).

1. Context

1.1 Scope of the study and deliverables

The goal of the EuCARD task 7.3 ("High Field Magnet") is to design and build the FRESCA2 magnet, with operational field of 13 T and short sample field of ~15 T at 1.9 K. The specified dipole length is 1.5 m. This meets the Fresca test facility upgrade requirements that also imply field homogeneity of 2% within a reference radius of 33 mm (2/3 of the bore aperture) over a sample length. Operation in the facility involves additional constraints in terms of space, power supply and stray field [1.1].

Interaction with the HTS insert introduces additional constraints at the interfaces. They are addressed in the detailed study, but they don't determine the layout. In particular, the mechanical structure of the insert must be removable, self-supporting and indexed longitudinally.

The goal of this study is to propose a relevant design (on the magnetic, mechanical and thermal levels) in order to meet those objectives. As superconducting magnet technology is very sensitive to details, the scope of this program includes conceptual and detailed engineering design. Even if it focuses on achieving the target field and aperture, the accelerator magnet requirements must be kept in mind. Task 7.3 has been divided into three working groups:

- Specification (SWG),
- Cable Design (CDWG),
- Magnet Design (MDWG) – initially: Magnet Pre-design (MPWG).

This study is in the framework of the MDWG, which gathers people from CERN and CEA-Saclay plus external contributors. Specification and cable data are considered as inputs.

The four years of the EuCARD-HFM project didn't allow for FRESCA2 magnet to be completed and tested over that period of time. The deliverable for this task is "Dipole model test with one superconducting coil; results analysed". It is due in month 48. We propose to redefine it with a report in four parts in order to highlight the large amount of progress toward project completion and to show the commitment of the partners to continue the work until completion.

- Deliverable EuCARD 7.3.1 (Part I): **Design report for the dipole magnet**. This is the present document.
- Deliverable EuCARD 7.3.1 (Part II): **Dipole magnet structure tested in liquid nitrogen**. The goal of this test is to demonstrate the efficiency of the mechanical loading of the magnet using bladders, keys and differential thermal shrinkage between materials.
- Deliverable EuCARD 7.3.1 (Part III): **Nb_3Sn conductor** procured for one dipole magnet.
- Deliverable EuCARD 7.3.1 (Part IV): **One test double-pancake copper coil** made.

1.2 Project history

1.2.1 Outline

The FP6 CARE-NED European program, from 2004 to 2007, has developed a new superconducting wire capable of achieving very high intensities (1400 A) in very high magnetic fields (12 T) [1.2].

Based on this development, a collaborative program has been set between CERN, LBNL, CEA-Saclay and CCLRC-RAL, named “Short Model Coil” (SMC). It helped to handle the principle of "bladders and keys" loading for the mechanical structure [1.3-1.5] in order to apply sufficient mechanical pre-stress to a prototype coil so that it could withstand the large magnetic forces.

The FP7 EuCARD-HFM European project officially started on 1st April 2009. Due to overload at CERN (consolidation after LHC incident in tunnel at the end of 2008) and at CEA, effective work began after the summer 2009 with the definition of the magnet specification and of the superconducting strand and cable layouts. A comparative analysis between different magnetic layouts was then carried out. The necessity to reduce the technical risk has driven us to concentrate on two possible options: cos-θ or block configurations. Solutions requiring more development, such as hybrid or graded coils, have been discarded. Indeed, these options would suppose longer development phases with less flexibility on the conductor use. This analysis is reported in [1.6]. It has led to select the block configuration during a collaboration meeting at Geneva University in June 2010.

On that base, the conception of the magnet and its support structure has been a four-year iterative process relying on strong and continuous collaboration between partners. Conceptual and detailed design of the dipole magnet itself, of its mechanical structure and of the related features (instrumentation, protection, cryostat…) was done. Experimental test campaigns have been led in parallel with numerical modeling and design activities. All of them are described in the present report.

Today, conceptual and technical design phases are completed. The mechanical structure of the magnet has been delivered, assembled and successfully tested. The first type of superconducting cable has been delivered and qualified. Magnet fabrication tooling has been designed and most of it has been fabricated. A full-size coil prototype is under winding (May 2013) using dummy copper cable.

Fabrication of the superconducting coils and magnet assembly will go on after the end of EuCARD. Dipole delivery is scheduled in late 2015.

1.2.2 Version-tracking

A strategy for version-tracking has been set in order to follow easily the evolution of the models, CAD geometries, drawings and reports.

The assembly {Coil and Structure} is tracked by a reference of this form: “C.S”. The first number (C) refers to the coil version; the second one (S) refers to the structure version, starting from the Baseline (#1). These values have been updated along the project history.

A comprehensive list of the design evolutions can be found in [1.7]. The present report relies on the latest version: #4.4.

Table 1.2.a – FRESCA2 DIPOLE VERSION TRACKER

Date	Version	Status
June 2012	**4.4**	**Structure has been realized and assembled successfully** **Winding tests will be done on this version**
October 2011	3.4	Last corrections before realization of the structure
July 2011	2.3	Call-for-tenders of Coil pack mockup + Structure
March 2011	2.2	“Optimized” coil/structure geometry
February 2011	1.1	“Baseline” version

1.3 External scientific reviews

At the start of the EuCARD project, the WP7-HFM collaboration formed an External Scientific Advisory Committee (ESAC) consisting of seven magnet and superconductivity experts from seven different laboratories in Europe, the US and Japan. The committee did in total four reviews during the EuCARD contract period.

The first review was held on January 20th to 21st 2011 at CEA-Saclay on the basic design of FRESCA2 dipole.

The second review was held on December 12th 2011 via video link on the subject of the Short Model Coil program, which is run as a preparation for FRESCA2 design and construction.

The third review was held on March 28th to 29th 2012 at CERN on FRESCA2 dipole.

The fourth and final EuCARD review was held on February 27th to March 1st 2013 at CEA-Saclay and was a combined review on FRESCA2 dipole (task 3) and the HTS insert (task 4).

The four reviews had a useful function at steering the design and construction process of the dipole. Under the pressure of the project schedule as dictated by EuCARD it has proven very useful to have a group of experts who every year review the work done and the outstanding challenges and urge the workers to take the necessary intermediate steps and not to skip essential development phases. Thus in the first dipole review the ESAC urged the project to insert many more development steps into the program as they were of the opinion that tasks of constructing this type of magnet posed big challenges without the presence of sufficient experience on several key topics. For the third review, which is the second one on the dipole, ESAC recognized that significant progress had been made but, given the difficulty, recommended to introduce an intermediate step with a mirror test on one coil only and to first analyze these results before continuing the coil construction. In the last review the committee stressed the importance of the tests on the dimensional changes of the cable during reaction and reiterated the need for a dedicated test with limited conductor usage of flared end coils before building the full magnet.

As the project will continue until completion after the end of the EuCARD project, the ESAC will continue to exist and will be called on a regular basis to help guiding the construction of FRESCA2 magnet.

2. Specification and constraints

The following table summarizes the inputs for FRESCA2 dipole: specification, external constraints and data from the other Working Groups. Specification is based on [1.1] (version 3.1, 10 October 2011). Additional sources are mentioned.

Additionally to this table, there are implicit cost and resource constraints.

Table 2.a – EuCARD-HFM DIPOLE SPECIFICATIONS AND CONSTRAINTS

Parameter name	Symbol	Unit	Value	Sources	Remarks
MAGNETIC SPECIFICATION					
Central field	B_0	T	13	EuCARD/FRESCA	at 4.2 K
Clear bore aperture diameter	Φ	mm	100	EuCARD/FRESCA/DWIIIG	Interface with HTS insert
Magnetic field homogeneity	$\Delta B/B_0$	%	2	FRESCA/De Rijk	within 2/3 of aperture over a sample length
Stray magnetic field	B_{out}	T	≤ 0.5	CERN safety rule	at personnel location
Operational temperature	T	K	1.8 to 4.2	Test station	
Pre-cooling tubes temperature	T_{tube}	K	300 to 70	Test station	at 16 bars
Operational current	I_{max}	kA	≤ 20	Test station	
DIMENSIONAL CONSTRAINTS					
Magnet length	L_{pole}	mm	= 1500	EuCARD	Coil end-to-end
Magnet pole width	w_{pole}	mm	≤ 600	Furnace	Reaction tooling included
Magnet pole height	h_{pole}	mm	≤ 500	Furnace	Reaction tooling included
Magnet straight section length	L_{ss}	mm	≥ 700	FRESCA/MPWG #14	Layer jump not included
Cold mass outer diameter	Φ_{ext}	mm	≤ 1300	Test station	
Cold mass length	L_{tot}	mm	≤ 2500	Test station/Furnace	

Table 2.a – EuCARD-HFM DIPOLE SPECIFICATIONS AND CONSTRAINTS – *CONTINUED*						
Parameter name		Symbol	Unit	Value	Source	Remarks
Nb_3Sn CONDUCTOR FEATURES | PIT (192) and RRP (132/169) [see § 3.2]						
Number of strands		N_{str}	/	40	CDWG	
Keystone angle		α	°	0	CDWG	
Strand diameter		Φ_{str}	mm	1.00	CDWG	± 0.1 mm
Cu / non Cu ratio		$r_{Cu/nCu}$	/	1.28	CDWG/Oberli	
Cable width		w_{cbl}	mm	20.9	CDWG/Oberli	Bare, unreacted
Cable thickness at 50 MPa		t_{cbl}	mm	1.82	CDWG/Oberli	Bare, unreacted
Transposition pitch		p	mm	120	CDWG/Oberli	Left-handed screw thread direction
Critical current with field normal to broad face	at 15 T	$I_{ss,\ 15T}$	A	15 710	CDWG/Oberli	at 4.2 K
	at 12 T	$I_{ss,\ 12T}$	A	31 420	CDWG/Oberli	at 4.2 K
Minimum critical current of extracted strand	at 15 T	$I^*_{ss,15T}$	A	437	CDWG/Oberli	at 4.2 K
	at 12 T	$I^*_{ss,12T}$	A	873	CDWG/Oberli	at 4.2 K
Growth during reaction	Width	$\delta_{HT,w}$	%	4	MDWG #24	(by convention)
	Thick.	$\delta_{HT,t}$	%	2	MDWG #24	(by convention)
CABLE INSULATION FEATURES [see § 3.3]						
Insulation type		/	/	Fiberglass + epoxy	MDWG #24	Braided
Insulation thickness		t_{ins}	µm	150 - 200	MDWG #24	Per conductor face (measurements on-going)
Insulation growth during reaction		/	%	0	MDWG #24	(by convention)

3. Conductor design

The parameters driving the definition of the Nb_3Sn strand for FRESCA2 cable have been identified. The main one is the current transported by the cable, which must be high enough to achieve a central field of 13 T at 4.2 K with sufficient margin in a large aperture dipole. This requirement implies that the critical current density of the strand is quite high and that the strand diameter is greater than 0.8 mm. On the other hand, this diameter shall not be too high for stability reasons, as detailed below.

A second requirement is to have enough cable flexibility to allow the winding of the coils. This puts a constraint on the strand diameter which has to be smaller than 1.3 mm.

The third requirement is related to magneto-thermal instabilities. High critical current density in Nb_3Sn strands may lead to premature quenches, which can reduce severely the magnet performance. To prevent self-field instability, the strand diameter must be small enough and the residual resistivity ratio (RRR) of the strand must be greater than 150. In order to control the instabilities induced by magnetization, the strand must have a relatively small effective sub-element size. Magnetization stability can be maintained at low magnetic field using sub-element diameters lower than 50 µm.

On the base of these requirements, **the strand diameter is fixed to 1.0 mm**. This is the best compromise between the need to have a high transport current and the necessity to avoid magneto-thermal instabilities.

3.1 Strand

3.1.1 Main parameters of the Nb_3Sn strand

The required parameters of the Nb_3Sn strand are summarized in Table 3.1.a:

Parameter name		Symbol	Unit	Value	Remarks
Table 3.1.a – SPECIFICATION OF THE Nb_3Sn STRANDS					
Strand diameter		Φ_{str}	mm	1.000	± 0.004 mm
Nominal sub-element diameter		$\Phi_{s/e}$	µm	$\lesssim$ 50	according to billet design
Cu / non Cu ratio		$r_{Cu/nCu}$	/	1.25	± 0.10
Strand twist pitch		p^*	mm	24	± 3; right-handed screw thread direction
Minimum critical current of extracted strand*	at 15 T	$I^*_{ss,15T}$	A	437	at 4.2 K (this is the acceptance criterion)
	at 12 T	$I^*_{ss,12T}$	A	873	at 4.2 K
Residual resistivity ratio		RRR	/	> 150	after full heat treatment
n-value		n	/	> 30	at 15 T, 4.2 K

Critical current values are based on a non-copper critical current density of 1250 A/mm^2 at 15 T and 4.2 K (2500 A/mm^2 at 12 T). Acceptance criterion for the critical current of the strand is defined at 15 T and 4.2 K. See § 3.1.4 for numerical parameterization.

3.1.2 Strand procurement and performance

In order to develop Nb_3Sn strand meeting the specification given in Table 3.1.a, qualification orders were placed to two suppliers: Bruker-EAS and Oxford Superconductors Technology (OST). These companies have the technological ability to produce long enough unit lengths of 1.0 mm-diameter strand, with sub-element diameter smaller than 50 µm and achieving both a high critical current density and a high RRR.

During the qualification phase, **Bruker-EAS** has fabricated Nb_3Sn strand with 192 sub-elements of a diameter around 48 µm, using the Powder in Tube (PIT) technique. As a first development step, two billets were fabricated using hexagonal sub-elements and one billet using round sub-elements. This is illustrated on Figure 3.1.1.

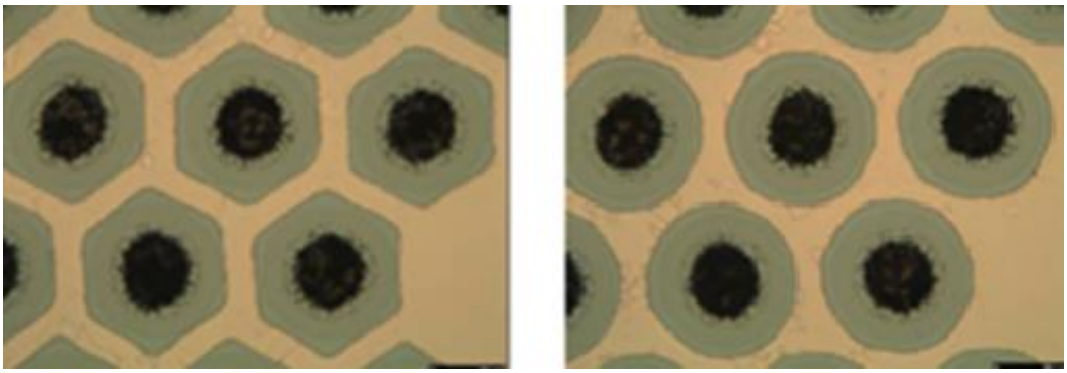

Fig. 3.1.1 – Cross-section of the PIT strands with hexagonal (left) and round (right) sub-elements.

Critical current densities above 1370 A/mm^2 (at 15 T) and 2450 A/mm^2 (at 12 T) were obtained at 4.2 K for both types of billets with the following heat treatment: a first plateau at 620°C during 120 hours and a second plateau at 660°C during 100 hours. Nevertheless, the billet with round sub-elements reached much higher critical current densities, up to 1450 A/mm^2 at 15 T. The RRR values of both billets using hexagonal sub-elements were below 100, while they were systematically higher than 180 for the billet using round sub-elements.

As a second qualification step before full production, Bruker-EAS has fabricated seven additional billets, all of them using round sub-elements. The heat treatment sequence was optimized further by them. RRR values between 170 and 280 were obtained with the following heat treatment: a first plateau at 620°C during 100 hours and a second plateau at 640°C during 120 hours. Critical current density was kept around 2450 A/mm^2 at 12 T and 1400 A/mm^2 at 15 T. The results of the measurements performed to qualify the seven billets produced by Bruker-EAS are given in Table 3.1.b.

Table 3.1.b – CRITICAL CURRENT DENSITY AND RRR OF THE PIT STRAND			
Strand identification code	Critical current density measured by CERN at 12 T [A/mm^2]	Critical current density measured by Bruker-EAS at 15 T [A/mm^2]	RRR measured by Bruker-EAS
DE10S10503	2518	1399	276
DE10S11201	2440	1410	227/231
DE10S11302	2467	1337	192
DE10S11403	2510	1484	195/213/214
DE10S23448	2427	1418	168/176
DE10S23258	2436	1382	208/216/219
DE10S23728	2548	1520	177/215

During the qualification phase, **OST** has fabricated Nb_3Sn strand with 132 sub-elements of a diameter around 58 µm, using the Rod Restack Process (RRP) technique. Critical current densities of 1650 A/mm^2 (at 15 T) and 2840 A/mm^2 (at 12 T) were obtained at 4.2 K with the first two billets with the standard heat treatment with three plateaus: 210°C during 48 hours, then 400°C during 48 hours and then 665°C during 50 hours. In this case, the RRR reaches values between 140 and 200. For the next four billets, OST decreased the temperature of the third plateau to 650°C so that to get more margin on the RRR value. Consequently, RRR values greater than 200 were obtained with very small loss of critical current (below 1%). The results of the measurements performed to qualify the seven billets produced by OST are given in Table 3.1.c.

Table 3.1.c – CRITICAL CURRENT DENSITY AND RRR OF THE RRP STRAND			
Strand identification code	Critical current density measured by CERN at 12 T [A/mm^2]	Critical current density measured by OST at 15 T [A/mm^2]	RRR measured by OST
Heat treatment: 48 hours at 210°C + 48 hours at 400°C + 50 hours at 665°C			
HO10S14108	2848	1648	142/157/152
HO10S14163	2828	1687	192/199/201
Heat treatment: 48 hours at 210°C + 48 hours at 400°C + 50 hours at 650°C			
HO10S14108	2770	1618	202/224/254
HO10S14310	2882	1608	243/248/256
HO10S14311	2837	1650	258/269/278
HO10S14312	2796	1571	245/268/273
HO10S14393	2836	1635	193/213/229

Both suppliers succeeded to produce Nb_3Sn strand meeting the specification of the FRESCA2 cable. Bruker-EAS has been quite successful with a very good strand piece length distribution: only 7% of the piece lengths were below 1 km. OST has reached a distribution with 40% of the piece lengths below 1 km.

3.1.3 Strand stability

To guarantee that FRESCA2 dipole will not be limited in performance by magneto-thermal instabilities,

- V-I measurements were performed on virgin strands for a wide range of magnetic field in order to detect self-field instabilities;
- V-H measurements were performed at low field to determine the stability current of the strand.

The results obtained with PIT strand (DE10S00904A24U) are presented on Figure 3.1.2. V-I measurements at 4.3 K (square markers) don't show any self-field instabilities above 6 T, while premature quenches occur at 2.0 K (triangle markers) in a field range between 5 T and 9 T with a quench current above 1500 A. The stability current determined by the V-H measurements is 1600 A at 4.3 K and 1400 A at 2.0 K.

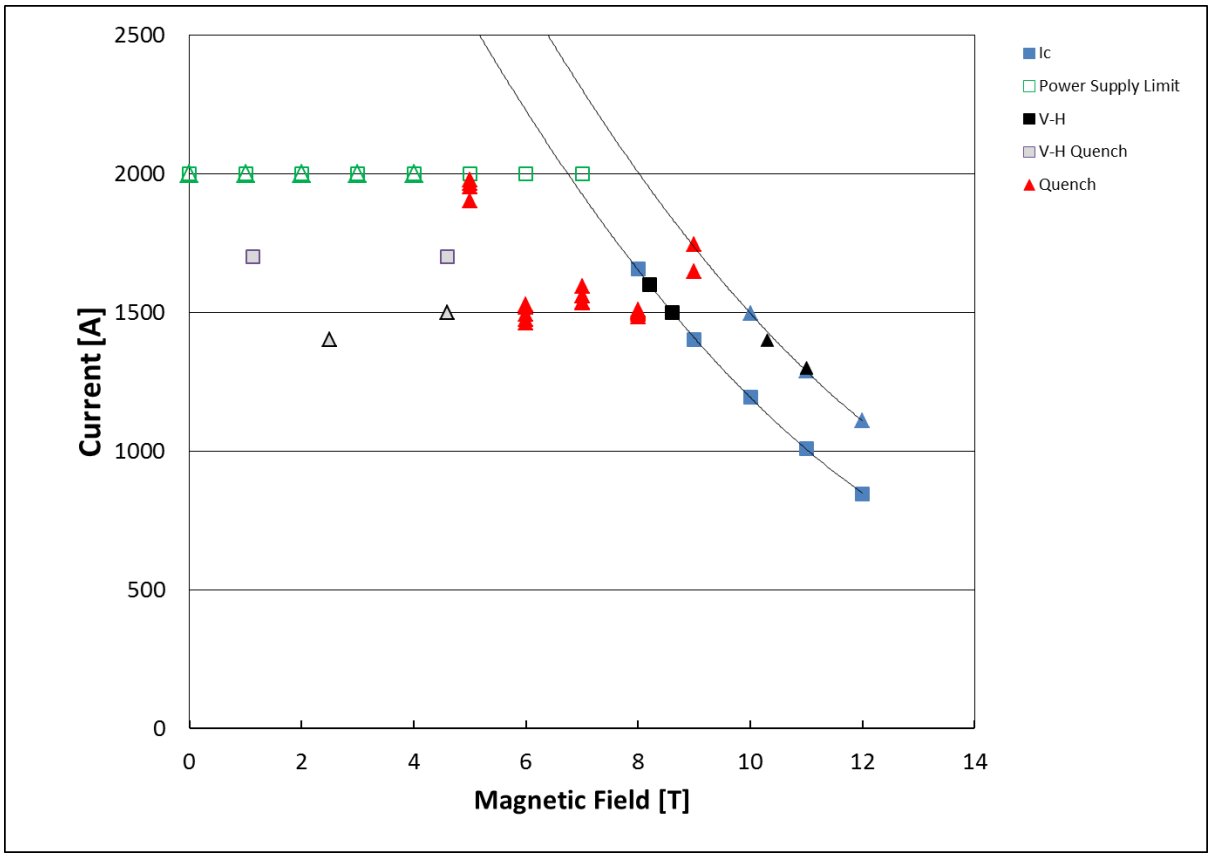

Fig. 3.1.2 – V-I and V-H measurements performed at 4.3 K (square markers) and 2.0 K (triangle markers) on PIT strand.

The results obtained with RRP strand (HO10S14311A06U) are presented on Figure 3.1.3. V-I measurements show that self-field instabilities start at much higher field at 2.0 K than at 4.3 K. Premature quenches occur at 4.3 K in an induction range between 0 and 6 T, and at 2.0 K in an induction range between 0 and 9 T with a quench current above 1900 A. The stability current determined by the V-H measurements is 1500 A at 4.3 K and 1400 A at 2.0 K.

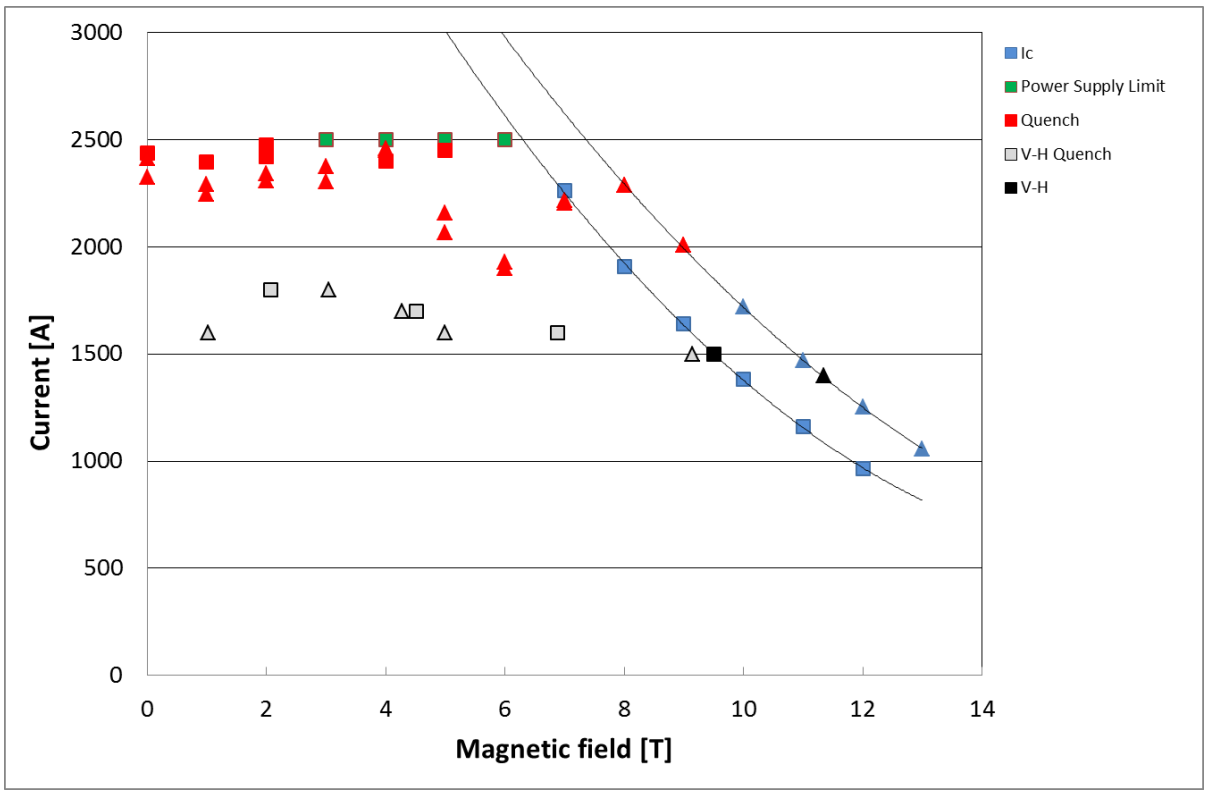

Fig. 3.1.3 – V-I and V-H measurements performed at 4.3 K (square markers) and 2.0 K (triangle markers) on RRP strand.

These results show that RRP and PIT strands are similarly affected by magneto-thermal instabilities, even though RRP strand shows much higher critical current density than PIT strand. With such high stability current, FRESCA2 dipole should not be affected by magneto-thermal instabilities.

3.1.4 Parameterization of the strand performance

Parameters and properties used in the magnetic design (see § 4) refer to the PIT strand, which has been qualified first.

In the following analysis, experimental data were fitted by parameterization curves, extrapolated to 1.9 K and compared with the magnet load-line. The critical current surface of the strand is modeled using the *Summers I* critical current fit [3.1], as:

$$J_c(B,T) = \frac{C}{\sqrt{B}}\left(1-\frac{B}{B_{c2}(T)}\right)^2 \cdot \left[1-\left(\frac{T}{T_{c0}}\right)^2\right]^2,$$

$$B_{c2}(T) = B_{c20}\left[1-\left(\frac{T}{T_{c0}}\right)^2\right]\left\{1-0.31\left(\frac{T}{T_{c0}}\right)^2\left[1-1.77\ln\left(\frac{T}{T_{c0}}\right)\right]\right\},$$

where T is the temperature and B the magnetic field. This curve has been fit with 2450 (3150) A/mm² at 12 T, 4.2 K and 1400 (1600) A/mm² at 15 T, 4.2 K for PIT (RRP) strands. Self-field correction has been considered [3.2]. Consistent with the results presented in § 3.1, cabling degradation of 5% (PIT) and 4% (RRP) has been assumed for extracted strands. The resulting fits are presented on Figure 3.1.4 and 3.1.5.

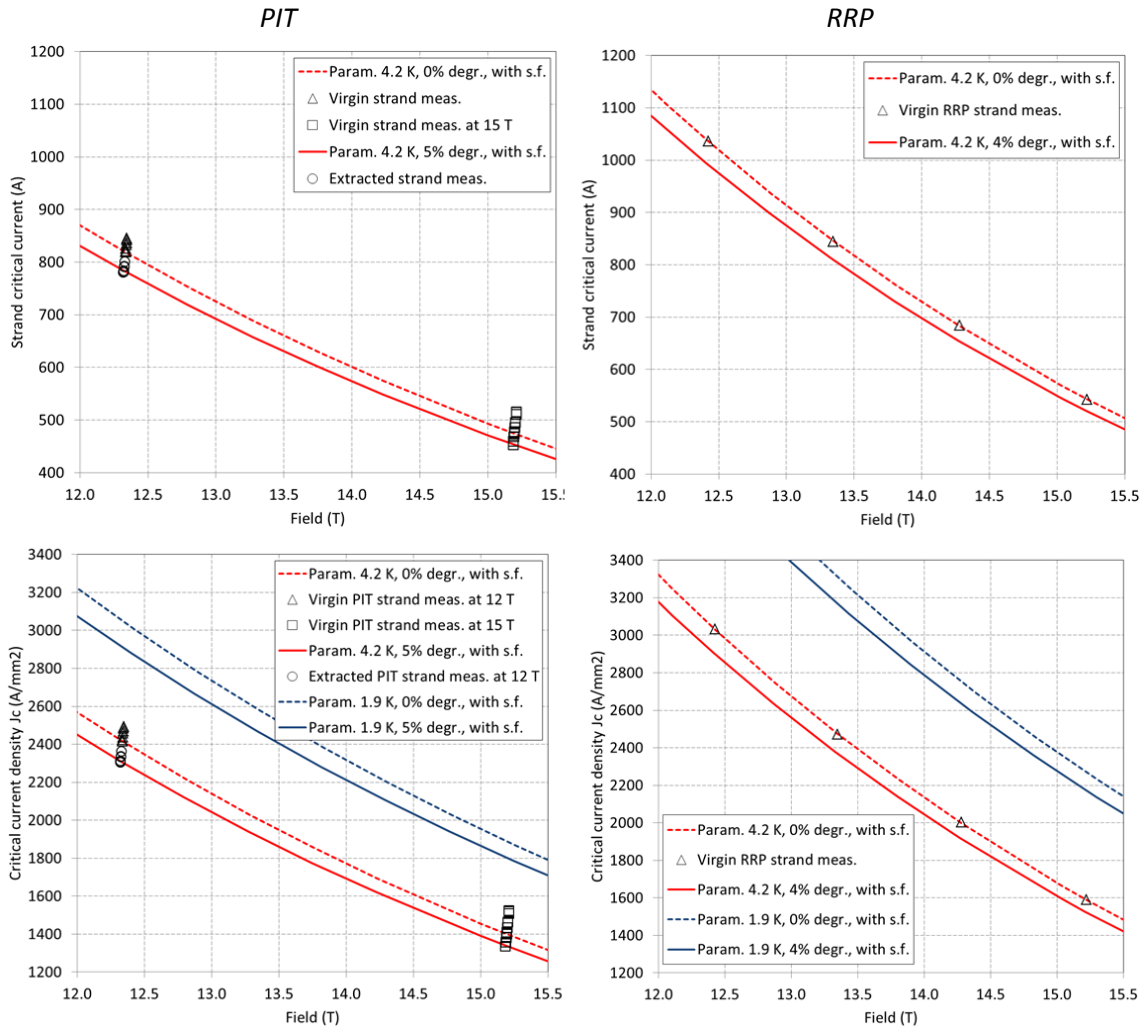

Fig. 3.1.4 – Strand critical current (top) and critical current density (bottom) vs. total magnetic field: measurements and parameterization curves of virgin strands (no degradation) and extracted strands with 5% (PIT) or 4% (RRP) degradation.

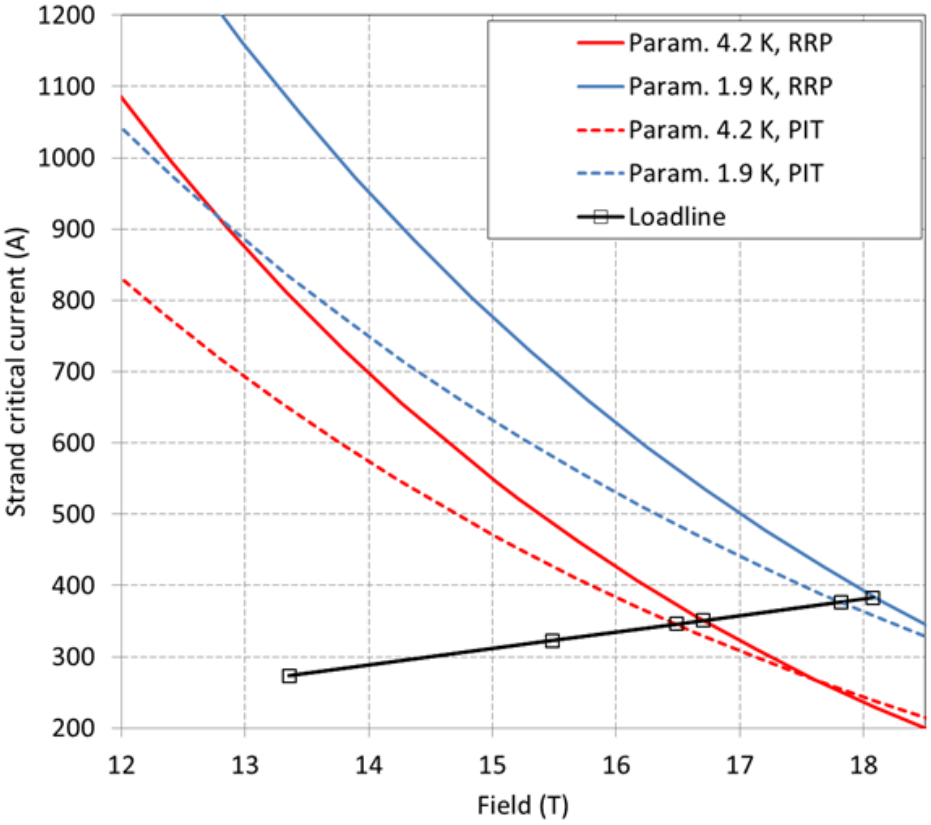

Fig. 3.1.5 – Strand critical current vs. total magnetic field: measurements and parameterization curves of virgin strands (no degradation) and extracted strands, together with the magnet load-line (see chapter 4).

3.2 Cable

3.2.1 FRESCA2 cable design

FRESCA2 cable is a rectangular Rutherford-type cable, consisting of 40 strands with a diameter of 1.0 mm. A typical cross-section is shown on Figure 3.2.1. The operation of cabling strands into a Rutherford cable results inevitably in large strand deformation around the cable edges. It causes severe distortions of the sub-elements inside of the strands. In order to minimize these deformations and to control the compaction of strands at the edges, the cable width has been fixed initially to 21.4 mm, using the following empirical formula:

$$w_{cbl} = \frac{N_{str}\emptyset_{str}}{2\cos p_{(°)}} + 0.72\emptyset_{str}\ ,$$

where N_{str} is the number of strands in the cable, Φ_{str} is the strand diameter and $p_{(°)}$ is the pitch *angle* of the cable. Cable thickness has been set independently to 1.82 mm. The transposition pitch length has been fixed to 160 mm.

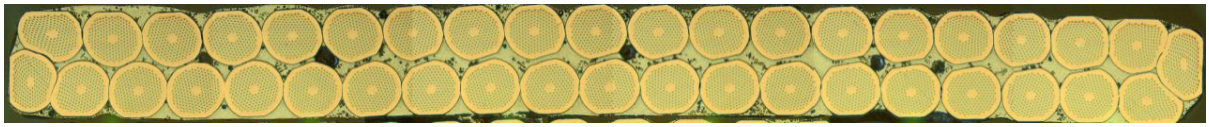

Fig. 3.2.1 – Cross-section of the FRESCA2 cable made of 40 strands of 1.0 mm diameter.

3.2.2 FRESCA2 Cable development

First phase of cable development with PIT strands

During the first cable development phase, using PIT strands from Bruker-EAS, focus was mainly put on the mechanical stability of the cable. Good mechanical stability is mandatory for coils winding. Additionally, it limits critical current degradation due to cabling. During that phase, CERN fabricated cables with four different widths, using ethanol as lubricant. As mentioned above, the first cable had a **width of 21.4 mm**. The pitch length was reduced from 160 mm to 120 mm in order to close the gaps observed between the strands in the midplane of the cable and to improve mechanical stability. Metallographic observations have shown that several strands undergo shear at some locations. Critical current measurements have been performed on one virgin strand and five extracted strands after the heat treatment sequence described in Table 3.2.a. The extracted strands have shown an average critical current reduction of 19% compared to the virgin strand. Following this result, a second cable was fabricated with a width of 22 mm, in order to decrease the strands deformation at the edges of the cable. This cable was fabricated with a pitch length of 120 mm. Gaps between strands have been observed again. They have been suppressed by reducing the pitch length to 100 mm. Critical current measurements on virgin and extracted strands from the cable fabricated with a pitch length of 120 mm have shown a significant increase of the degradation up to 26%. This is opposite to what was expected.

Table 3.2.a – HEAT TREATMENT SEQUENCE				
Cable	Heat treatment	Step 1	Step 2	Step 3
RRP	Temperature [°C]	210	400	665
	Duration [h]	48	48	50
PIT	Temperature [°C]	620	650	-
	Duration [h]	120	90	-

Metallographic observation of the edges of the cable shows that the shear regions are larger on some strands. Thus, considering the large increase of the critical current degradation, next cables were fabricated with a smaller width. A small reduction in width is expected to prevent part of the shear effect by providing better mutual support between neighboring strands during their flattening in the cabling machine.

A third cable was then fabricated with a **width of 20.9 mm** and a transposition length of either 120 mm or 140 mm. They both met all the quality requirements, having no gaps between strands. The critical current measurements on the strands extracted from the cable have shown an average degradation of 15% for the pitch length of 120 mm and 18.5% for the pitch length of 140 mm.

This suggests that the degradation could be decreased further by fabricating a narrower cable. Indeed, the average critical current degradation of the cable fabricated with a **width of 20.4 mm** has been reduced to 10% with a pitch length of either 120 mm or 150 mm. The thickness here had been increased to 1.86 mm. Metallographic observation around the edges of the cable shows three highly deformed strands per side but a limited number of distorted sub-elements, as shown in Figure 3.2.2. The high level of deformation of these strands indicates that they are already too much compacted and that further reduction of the cable width can no longer be envisaged.

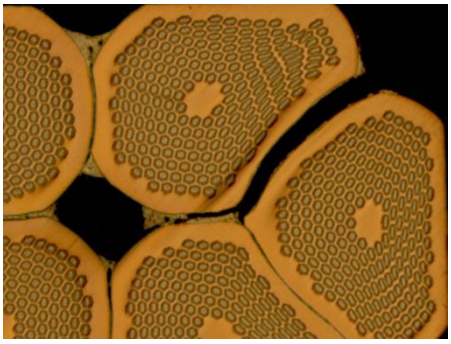

Fig. 3.2.2 – Cross-section of the 20.4 mm-wide cable fabricated with PIT strands, with a thickness of 1.86 mm and a transposition pitch of 120 mm (close-up on the edge).

Following these results, next cable was fabricated with a **width of 20.9 mm**. The width of the mandrel was also slightly decreased. To improve strand wrapping around the mandrel, ethanol was replaced by oil as a lubricant on the part of the mandrel which is in contact with the strands. Critical current measurements on virgin and extracted strands from the 1.82 mm-thick cable have shown an average critical current reduction of 9% with ethanol and 5.5% with oil. It is interesting to point out that the distribution of the critical current values between extracted strands is also influenced by the lubricant. This distribution is characterized by a sigma of 1% with oil and 2.8% with ethanol.

Second phase of cable development with RRP strands

During the second cable development phase, two cables were fabricated using RRP strands from OST. The cables were fabricated using oil or butanol as lubricant during cabling. Transposition pitch length was fixed to 120 mm and mid-thickness to 1.82 mm. Metallographic observation on both cables shows severe distortions of the sub-elements inside the three strands located near the edge, as shown in Figure 3.2.3. The sub-elements that are highly impacted by shear stress during cabling are circled in the figure.

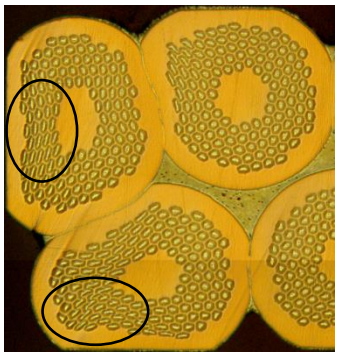

Fig. 3.2.3 – Cross-section of the 20.9-mm wide cable fabricated with RRP strands, with a thickness of 1.82 mm and a transposition pitch of 120 mm (close-up on the edge).

Even though, critical current measurements performed on strands extracted from both cables have shown an average degradation of 4% after the heat treatment sequence described in Table 3.2.a. The distribution of the critical current values between extracted strands is characterized by a sigma of 1.4%.

Following the successful fabrication of the cable using RRP strands and butanol as lubricant, a new cable was fabricated using PIT strand and butanol. Critical current measurements on six extracted PIT strands shown an average degradation of 7.8%. They can be compared to the previous ones of 9% with ethanol and 5.5% with oil. From these results, we can conclude that butanol gives better results than ethanol. Cross-sections of the edge of three cables fabricated using ethanol, oil or butanol are compared on Figure 3.2.4.

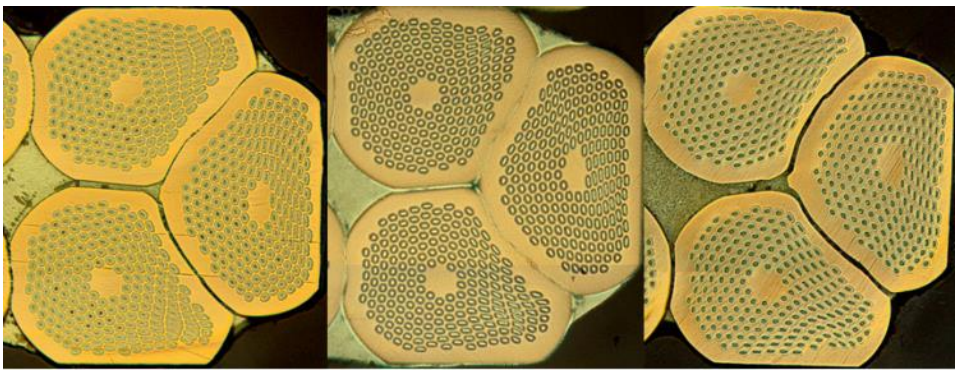

Fig. 3.2.4 – Cross-section of the edge of cables fabricated with PIT strands using either ethanol (left), oil (middle) or butanol (right) as lubricant.

PIT strands appear to be less deformed when oil is used as lubricant instead of butanol. This is not the case with RRP strands, as shown on Figure 3.2.5.

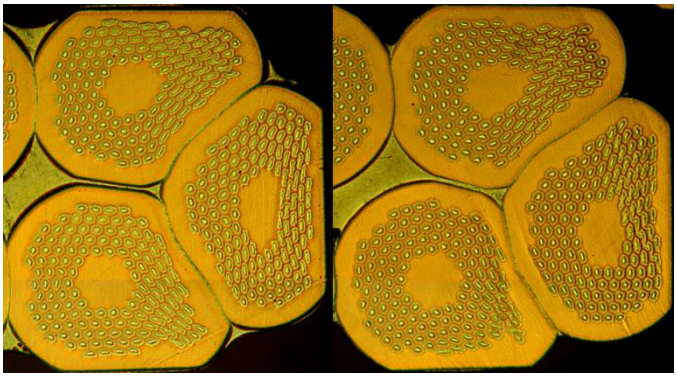

Fig. 3.2.5 – Cross-section of the edge of cables fabricated with RRP strands using either oil (left) or butanol (right) as lubricant.

Conclusion regarding the cable development phase

During the FRESCA2 cable development phase, the cable transposition pitch length originally fixed to 160 mm has been reduced to 120 mm in order to improve the mechanical stability of the cable and to close the gaps appearing between the strands in the midplane of the cable. The width of the cable was optimized until a critical current degradation smaller than 10% occurs during cabling. This objective was achieved with a **transposition pitch length of 120 mm, a width of 20.9 mm and a thickness of 1.82 mm**. Lubrication during cabling has been identified as an important parameter for the cable fabrication. Using oil, the critical current degradation due to cabling was reduced to 5.5%, instead of 9% with ethanol.

Main parameters of FRESCA2 cable

The main parameters of FRESCA2 cable are summarized in Table 3.2.b.

Parameter name		Symbol	Unit	Value	Remarks
Table 3.2.b – MAIN PARAMETERS OF FRESCA2 CABLE					
Number of strands		N_{str}	/	40	
Keystone angle		α	°	0	
Cable width		w_{cbl}	mm	20.9	Bare, unreacted
Cable thickness at 50 MPa		t_{cbl}	mm	1.82	Bare, unreacted, in the midplane
Transposition pitch		*p*	mm	120	Left-handed screw thread direction
Critical current with field normal to broad face	at 15 T	$I_{ss,15T}$	A	15710	at 4.2 K
	at 12 T	$I_{ss,12T}$	A	31420	at 4.2 K
n-values		*n*	/	20	at 15 T, 4.2 K
Residual resistivity ration		RRR	/	> 120	after full heat treatment
Minimum cable unit length		L_{min}	m	260	

3.3 Cable insulation

3.3.1 Principle

High strength fibres that withstand temperatures up to 700°C are used for the electrical insulation and structural reinforcement of Nb_3Sn superconducting magnet coils. Nevertheless, the fibre alone doesn't ensure structural reinforcement after reaction. It must be filled with epoxy resin during an impregnation phase. Hence, the fibre principally plays a role of space filler. E-glass fibre, for example, loses almost 100% of its mechanical properties during reaction. S-glass fibre, which is currently considered, loses 75% of its strength after heat treatment.

S-glass is 10 to 15% better than E-glass in terms of strength at room temperature. It has an additional advantage since it can withstand higher operating temperatures than E-glass. S- and S-2 glass fibres (S-2 is a product variant) have the same glass composition but different coating. Good internal structural uniformity (high strength) is achieved with these boron-free and alkali-free glasses. Their forming temperatures are higher than the one of E-glass.

A thermal de-sizing may induce further degradation of the mechanical properties. If used, a ceramic binder may also have impact the degradation of the mechanical properties of the fibre by bonding its glass filaments. The absence of strong structural fibres inside the epoxy matrix could promote fractures inside the insulation.

3.3.2 Fabrication

Continuous fibres of S-2 glass yarns are twisted together to provide strand integrity. These yarns consist in numerous filaments of various diameters twisted together. A chemical sizing protects the glass filaments from abrasion during processing. It is generally removed after processing before the fabric is treated with a resin-compatible finish (*i.e.* epoxy). The filaments forming the yarn have the same diameter, usually between 4 and 13 µm. In the following, the "tex" unit will be used. It is a unit of linear density corresponding to the mass (in grams) of 1,000 m of fiber. Usual values range between 5 to 400. Fiberglass of grade 66 tex is braided around the cable (S-2 Glass from AGY, starch sizing, Figure 3.3.1) in order to obtain the configuration shown in Figure 3.3.2**Erreur ! Source du renvoi introuvable.**.

Fig. 3.3.1 – S-grade fibre-glass braided around a cable.

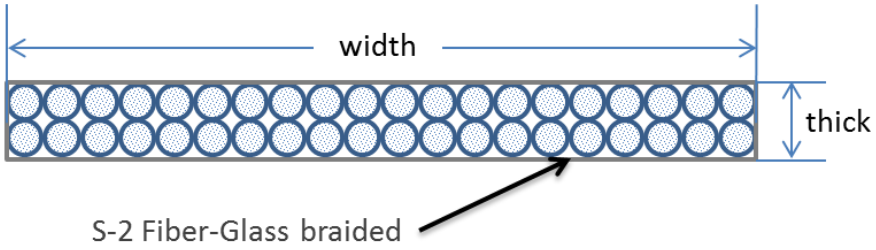

Fig. 3.3.2 –Cable insulation scheme.

3.3.3 Dimensioning

The insulation is made of two layers of braided S-2 fiberglass per face, with a thickness around 0.1mm per layer. The turns per meter (TPM) and nominal twist is Z40 (Figure 3.3.3) with a nominal filament of Ø9 µm and an approximate yarn diameter of 0.19 mm using 66 tex (Figure 3.3.4).

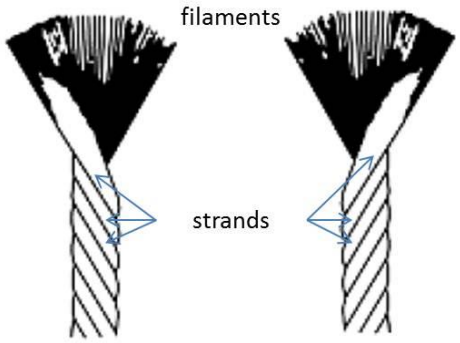

Fig. 3.3.3 – Yarns: 'S' twist and 'Z' twist.

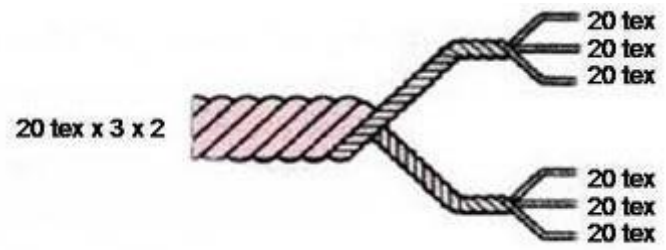

Fig. 3.3.4 – Example of tex measurement:
20 tex x 3 (three bundles of 20 g/1000 m each) in two 'Z' strands, into a 'S' yarn.

The following studies and tests were done at the polymer lab of CERN/TE-MSC:

- Impact of thermal de-sizing and reaction on S-2 glass as a function of the reaction cycle;
- Study of the thermal stability of 933 AGY chemical sizing + epoxy compatibility (after reaction);
- Evaluation of the influence of different ceramic binders (they tend to weaken the fiber by bonding the filaments);
- Traction tests on S-2 type fiberglass before reaction, after de-sizing and after reaction;
- Re-sizing with palmitic acid using a dedicated station assembled at CERN.

3.4 Thermo-mechanical characterization

For computation and detailed design purposes, we need to know the evolution of the cable and insulation dimensions along the successive phases of the magnet lifecycle, from coil winding to magnet cool-down and operation at 4 K.

Cable and insulation samples representative of those different phases are needed:

- unreacted insulated cables representative of the winding phase,
- reacted insulated cables representative of the heat-treated coil,
- reacted and impregnated cables representative of impregnated coil.

In order to limit the errors, dimensional measurements are performed on stacks of ten conductors, called “ten-stacks”, compressed on their large face while their height variation is measured. They can be bare or insulated.

The ten-stacks are prepared following a manufacturing process representative of the coils’ one. Reaction and impregnation molds have been designed and manufactured in order to treat up to four stacks at the same time.

Conductor reference height is determined on the base of compression tests performed at low pressure (5 MPa) on one, two or three unreacted bare conductor stacks.

In order to quantify the growth of the cable section induced by heat treatment, compression tests up to 5 MPa are performed on reacted bare conductor stacks inside a free cavity (which is 26% larger than the nominal stack height). The expansion rate of the conductor (with respect to its nominal unreacted dimension) is measured. This value is applied to a second series of bare conductor stacks and a series of insulated ones.

Insulation thickness is determined by difference between compression tests up to 5 MPa on bare and insulated conductor stacks, before and after heat treatment.

Additional mechanical tests are carried out on insulated, reacted and impregnated ten-stacks, representative from the final coil. The test program includes:

- room temperature compression tests up to 100 MPa on at least three samples,
- 4 K compression tests up to 100 MPa on at least two samples,
- thermal contraction measurement between room temperature and 77 K on at least three samples,
- thermal contraction measurements between room temperature and 4 K on at least two samples.

Table 3.4.a summarizes the thermo-mechanical cable characterization program. All the tests included in this program must be performed on both types of cables foreseen for FRESCA2 coils (see §3.1, 3.2), using PIT or RRP strands.

Table 3.4.a – SUMMARY OF THE THERMO-MECHANICAL CABLE CHARACTERIZATION PROGRAM							
Ten-stack name*	Insulation	Heat-treatment	Impregnation	Test	Goal	Quantity	Cable need
ExNNN	-	no	no	RT: comp. 5 MPa	non reacted bare cable thickness	1	8.5 m (bare)
ExNTN	-	yes (26.5%)	no	RT: comp. 5 MPa	thickness of the bare cable reacted in a large cavity → optimal reacted cavity size (+x%) for each cable type	3	
ExNTN	-	yes (x%)	no	RT: comp. 5 MPa	reacted bare cable thickness verification	2	
ExINN	S-2 66 tex	no	no	RT: comp. 5 MPa	non reacted insulated cable thickness → non reacted insulation thickness	1	1.5 m (ins.)
ExINN	*Final*	no	no	RT: comp. 5 MPa	non reacted insulated cable thickness → non reacted insulation thickness	2	13.6 m (ins.)
ExITN	*Final*	yes (x%)	no	RT: comp. 5 MPa	reacted insulated cable thickness → reacted insulation thickness	2	
ExITI	*Final*	yes (x%)	yes	RT : comp. cycles, thermal shrinkage, 4K : comp.cycles	impregnated cable mechanical behavior	4	
					** x = R for RRP cable, P for PIT cable*	**15**	**23.6 m**

Real cable was not available during the conceptual and detailed design phases. Hence, the cable growth during reaction has been estimated from the feedback of previous projects [refs needed]. The values indicated in Table 3.4.b have been considered. This leads to the theoretical evolution of the cable section presented on Figure 3.4.1. Assuming an insulation thickness of 150 µm and a nominal cable thickness comprised between 1.82 and 1.86 mm, **it has been decided to perform the CAD design** (§ 5, 7) **on the base of a reacted insulated cable section of 21.8 x 2.22 mm**.

Table 3.4.b – ASSUMED GROWTH DURING REACTION			
Cable growth during reaction	Width	%	4
	Thickness	%	2
Insulation growth during reaction		%	0

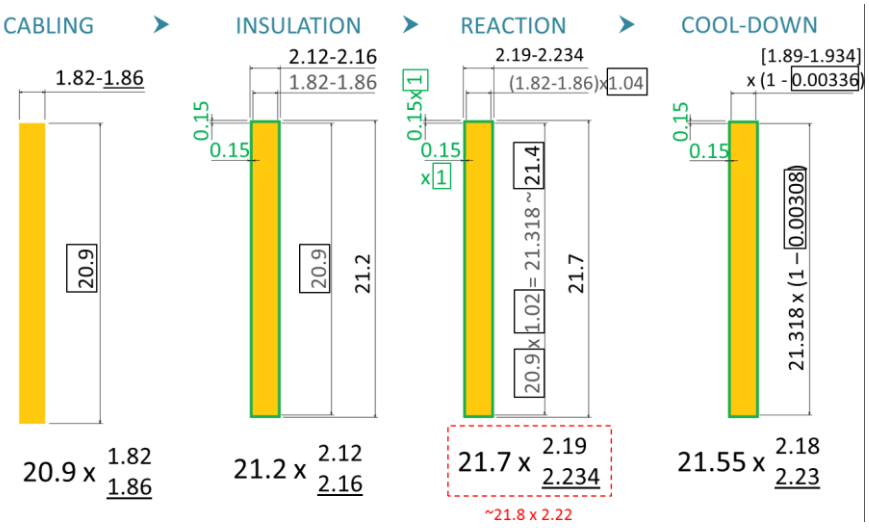

Fig. 3.4.1 – Assumed evolution of the cable section along magnet lifecycle (values in mm).

4. Magnetic design

4.1 Evolution of the cross-section design

The main steps undertaken during the design of FRESCA2 cross-section, from the early conceptual phases on, are recalled next. The focus is on the "block design", leaving the cos-Θ layout – that has been explored in parallel for a certain period [1.6] – aside (see § 1.2).

1. In the first meetings, the nominal characteristics of the conductor (geometry of the Rutherford cable, insulation thickness and critical current density) have been defined. These numbers have been kept constant, exception done for dedicated sensitivity studies (see § 4.3), in particular regarding the size of the cable.

2. At the same time, analytical estimates were done on the total amount of conductor needed in the cross-section (see § 4.2). That was evaluated at about 156 turns of cable per pole.

3. The first design involving two double-pancakes (*i.e.*, four layers) was presented at the end of August 2009. Back then, the two double blocks were separated by means of a spacer. This was introduced mainly to have an additional parameter to optimize the field quality.

4. Several layouts were studied, varying in particular the number of turns in the different layers and the 2D position of the blocks. Aside from reaching the target central field of 13 T, the objective was to improve the field quality at high current. Several configurations able to minimize the harmonics up to b_{11} [1] were found.

5. Out of these attempts, a first reference cross-section was defined, so-called "41-41-37-37", from the number of turns in the various layers (counting them from the midplane outwards, see Figure 4.3.1).

6. The feasibility of splitting the top double-pancake in two by means of a spacer was explored. Again, this was more for field quality reasons than for mechanical ones, as no effective way to perform some sort of stress management was envisaged.

7. The effect of ferromagnetic material around the coil was studied, addressing in particular the influence of:

   a. iron in the yoke,

   b. iron in the vertical / horizontal pads,

   c. iron in the top pole (for layers 3-4).

8. The relative importance of field quality became less and less predominant over time. Therefore, several studies were done to assess how much the strength could be increased if the field quality requirements became less stringent.

9. Mechanically, the first cross-section involved the presence of a high resistance stainless steel support tube in the bore (see § 5). This component was meant to provide rigidity to the bottom pole and to present a clear interface for the HTS insert. It was then realized that its presence was not mechanically essential for the FRESCA2 magnet, and that the interface with the insert could be resolved in other ways. Therefore, this tube has been withdrawn from the cross-section.

[1] b_i is defined as $b_i = \frac{Bi}{B0} . 10^{-4}$.

10. The convenience of having double-pancakes with one turn difference in the two layers has been explored. This was suggested to simplify the layer jump region (see § 4.3.2). At the end, a different solution has been proposed for that jump, and a design with the same number of turns in the two layers of a double-pancake was retained.

11. A rather comprehensive screenshot of the cross-section was prepared at the beginning of 2011 for the ESAC design review. This includes the so-called “36-36-42-42” design, in which the conductors are nominally aligned on the external faces (away from the pole) in the four layers, and no spacer is present between the two double-pancakes. This configuration presents a single lateral surface, which simplifies the application of lateral pre-load.

12. Later on, the cross-section was partially slimmed, with the external radius of the yoke decreased from 500 mm to 450 mm, on the basis of magnetic and mechanical considerations (see § 4.3.1).

13. The basic philosophy for the structure was constant throughout the design. It corresponds to a bladders-and-keys scheme aiming at providing partial pre-stress on the coil at room temperature, complemented by an additional pre-stress at cryogenic temperature coming from the differential shrinkage of an aluminum alloy cylinder. Parametric analyses of the effects of the geometry (in particular the outer radius of the iron yoke and the thickness of the shell) and materials (aluminum alloy and stainless steel for the cylinder, for example) were considered (see § 5).

14. In August 2011, a sensitivity analysis of the harmonics considering different insulation thicknesses was performed. This can be used as a basis to assess how much a change of geometry of the cable would affect the field in the bore.

15. A reference cross-section has been presented and commented at the MT22 conference in September 2011. Small changes since then involved the change of space around the double-pancakes allocated for the traces (carrying instrumentation and protection heaters).

4.2 Analytical estimates

Before embarking on a detailed magnetic design of the cross section, the amount of conductor needed can be estimated using the analytical approach of [4.1,4.2]. In this method, it is assumed that the coil is a sector coil, as shown in Figure 4.2.1. In particular, a [0-60°] layout and a [0-48, 60-72°] layout are used: the latter has a better field quality that is traded for some field strength.

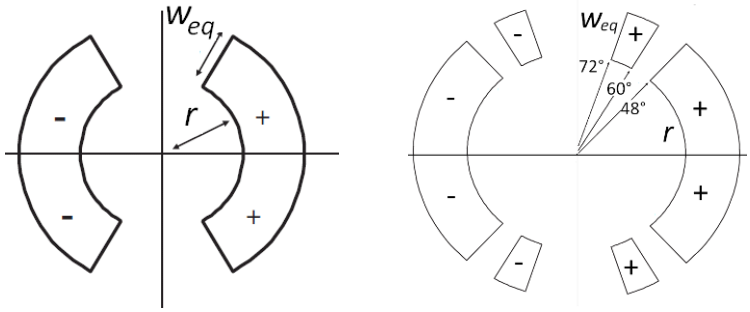

Fig. 4.2.1 – Schematic layout of a 60° sector coil (left) and a [0-48, 60-72°] sector coil (right) for a dipole of aperture radius r and coil width w_{eq}

The magnet aperture radius is specified to 50 mm. The radius *r* in this analysis is set to 60 mm because it is envisaged that some material in between the coil and the bore is necessary to hold the necessary pre-stress.

The ratio λ between peak field on the coil and central field scales with the aspect ratio as

$$\lambda(w,r) = 1 + a\frac{r}{w_{eq}},$$

where a = 0.06. This hyperbolic fit is obtained for sector coils and is adequate for cos-θ dipoles. In the case of a block design as we have, λ is likely to be higher for the same radius and equivalent width.

The short sample field at 4.2 K (noted $B_{ss,\,4.2\,K}$) is obtained from

$$B_{ss,4.2K} = \frac{\kappa c \gamma_0 w_{eq}}{2}\left(\sqrt{\frac{4b}{\kappa c \lambda \gamma_0 w_{eq}} + 1} - 1\right)$$ with the parameters:

- filling factor κ = 0.289 (from cable specification, § 2),

- c = 3375 A/mm^2, b = 20 T for the hyperbolic critical surface fit at 4.2 K,

- c = 3625 A/mm^2, b = 21.5 T for the fit at 1.9 K,

- γ_0 = 6.928·10^{-7} Tm/A for the [0-60°] sector coil and γ_0 = 6.625·10^{-7} Tm/A for the [0-48, 60-72°] one.

Table 4.2.a contains a parametric analysis performed varying the amount of conductor. The width w_{eq} of the sector coil is computed from the number of turns of cable per pole. The short sample fields are reported at 4.2 K and 1.9 K for the two sector geometries considered.

Table 4.2.a – ANALYTICAL ESTIMATES OF SHORT SAMPLE FIELDS BASED ON SECTOR COILS (WITHOUT IRON)						
Number of turns (per pole) [/]	w_{eq} [mm]	λ [/]	[0-60°] sector coil		[0-48, 60-72°] sector coil	
			$B_{ss,\ 4.2\ K}$ [T]	$B_{ss,\ 1.9\ K}$ [T]	$B_{ss,\ 4.2\ K}$ [T]	$B_{ss,\ 1.9\ K}$ [T]
70	40.3	1.09	12.6	13.5	12.0	12.9
80	44.9	1.08	13.0	13.9	12.4	13.3
90	49.2	1.07	13.3	14.3	12.7	13.7
100	53.3	1.07	13.6	14.6	13.0	14.0
110	57.3	1.06	13.9	14.9	13.2	14.2
120	61.2	1.06	14.1	15.1	13.5	14.5
130	65.0	1.06	14.3	15.4	13.7	14.7
140	68.6	1.05	14.5	15.6	13.8	14.9
150	72.2	1.05	14.6	15.7	14.0	15.1
156	74.2	1.05	14.7	15.8	14.1	15.2
160	75.6	1.05	14.8	15.9	14.2	15.2
170	79.0	1.05	14.9	16.1	14.3	15.4
180	82.3	1.04	15.1	16.2	14.4	15.5
190	85.5	1.04	15.2	16.3	14.5	15.6
200	88.6	1.04	15.3	16.4	14.6	15.7

From this analysis, a tentative number of 156 turns of cable per pole has been selected. This is based on the following arguments:

- $B_{ss,\ 1.9\ K}$ for a [0-48, 60-72°] sector coil dipole without iron is in the 15 T region for 150-160 turns,
- the iron is likely to increase this value by about 5% (see § 4.2),
- the peak field over central field ratio (λ) may be less favorable than assumed, thus equaling out the contribution of the iron.

The equivalent width w_{eq} for 156 turns is w_{eq} = 74.2 mm. For a cos-θ configuration, assuming that about 15% is used up for wedges, a physical width of w = 85.3 mm is needed. Thus, using a cable about 21 mm wide, four layers are needed per pole. This is a convenient number because it corresponds to two double-pancakes per pole. This analysis can be roughly extended to a block layout. Following a comprehensive comparative analysis, it has been decided to work with four layers per pole, corresponding to two double pancakes, comprising 156 turns in total.

4.3 2D magnetic design

Thanks to the previous analytical estimates, the number of turns has been fixed to 156 per pole, shared between four blocks that are divided into two double-pancakes [1.6]. In order to facilitate the winding, it has been decided to have the same number of turns in both layers of each double-pancake coil. In the cross-section, it means that the number of turns is identical for the two lower layers (1 and 2) and for the two upper ones (3 and 4). Figure 4.3.1 indicates how the layers are numbered (in one quadrant).

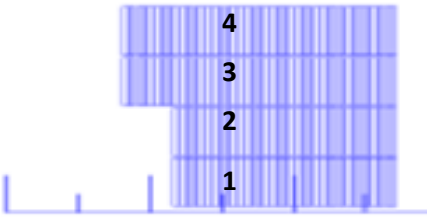

Fig. 4.3.1 – Layers numbering.

Consistent with § 3, the following magnetic design has been done with a conductor section of 21.4 x 1.82 mm degraded at 5% (PIT) or 4% (RRP) with an insulation of 200 µm per conductor face [1.1]. The change in the conductor section before and after cooling has not been considered. This should have little influence on the parametric study. Only the final configuration has been calculated with the cable section at 4 K (dilatation coefficients are indicated on Figure 3.4.1).

2D calculations have been done using Roxie software [4.3].

4.3.1 Parametric study

The influence of different parameters has been studied in order to reach the best compromise between field strength and quality, reasonable forces, sufficient operating margin and easiness of winding.

First parametric studies have been done with a layout comprising two double pancakes and a total of 156 turns. The layout is the result of an iterative process: it has evolved along the project (see § 4.1). The parametric study couldn't be restarted from scratch at each step. Nevertheless, it is reasonable to consider that our general conclusions remain valid regardless of minor configuration changes. This project history explains why we can find different layouts and some slight inconsistencies in the following parametric analysis.

In the following, we focus on: the influence of a shim inside of the layers, the repartition of iron in the magnet cross-section, the repartition of conductors in the layers, the horizontal and vertical position of the layers (including the gaps between them).

Shimming inside of the layers

The stress in the third layer is higher than in the other ones (Figure 4.3.2 and Table 4.3.a). The possibility to decrease this stress with a shim located inside of the third and the fourth layers has been studied. The configuration considered here was simple: "41-41-37-37" layout with no iron in the yoke and pads.

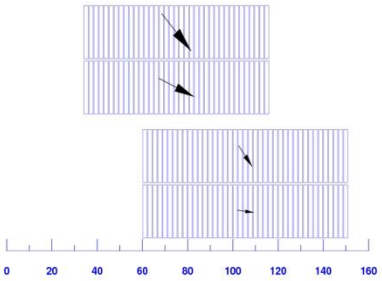

Fig. 4.3.2 – Forces in the layers (values are given in Table 4.3.a), "41-41-37-37" layout.

Table 4.3.a – STRESSES AND FORCES IN THE LAYERS				
Layer	F_x [MN/m]	σ_x [MPa]	F_y [MN/m]	σ_y [MPa]
1	1.43	65	-0.19	-2
2	1.19	54	-1.66	-18
3	3.08	141	-1.47	-18
4	2.60	119	-2.99	-36

Two configurations have been studied and optimized to improve the field quality: "41-41-(19/18)-(19/18)" and "41-41-(11/26)-(11/26)". The first configuration reduces the peak stress in the third layer from 141 MPa to 118 MPa; the second one reduces it to 79 MPa (Figure 4.3.3 and Table 4.3.b).

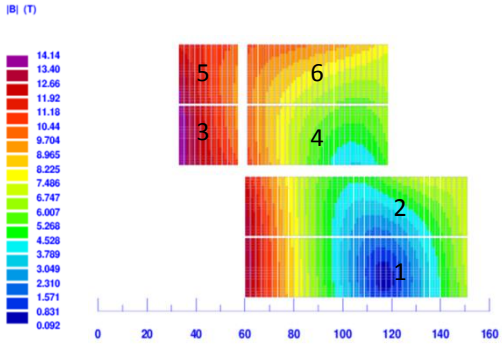

Fig. 4.3.3 – Magnetic field with the "41-41-(11/26)-(11/26)" layout.

Table 4.3.b – FORCES AND STRESSES WITH THE "41-41-(11/26)-(11/26)" LAYOUT				
Block	F_x [MN/m]	σ_x [MPa]	F_y [MN/m]	σ_y [MPa]
1	1.45	66	-0.17	-2
2	1.21	55	-1.62	-18
3	1.73	79	-0.19	-8
4	1.49	68	-0.65	-27
5	1.33	61	-1.41	-24
6	1.09	50	-2.37	-41

The “41-41-(11/26)-(11/26)” layout leads to homogenous repartition of the stresses and forces between the blocks. The field quality optimization imposes a distance of 4 mm between the lower and upper blocks and a midplane shim thickness of 3.6 mm (which is the horizontal gap between blocks 3 and 4 or 5 and 6). This option has *not* been retained because there was no easy technical solution to contain the stresses with such a thin shim.

Iron configuration

Magnetic iron can be added around the coils to contribute to the field. In principle, it could allow to increase the central flux density for a given current while decreasing the peak field on the conductor. Different iron configurations have been compared, with iron in the yoke, in the pads and/or in the top post[1].

The type of iron considered here is Magnetil, as was used in the LHC magnets. It has the following B(H) curve:

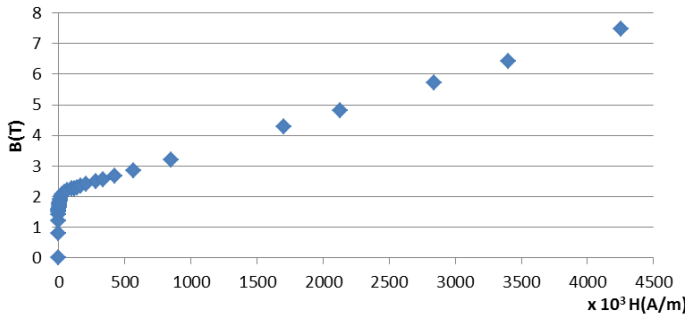

Fig. 4.3.4 – B=f(H) curve for Magnetil iron. Saturation occurs at 2.12 T.

A preliminary study has been done in order to optimize the **iron yoke** thickness. There is a compromise between its weight/dimensions and its contribution to the magnetic field.

This comparative analysis has been led on the “41-41-37-37” layout (Figure 4.3.2). Some space must be reserved around the coils for the elements of the coil pack: the yoke aperture is fixed to 250 mm per side (see Figure 4.3.5). There is *no* magnetic pad or post. The effect of the external radius of the iron yoke R_{yoke} on the central field has been calculated. The current considered here is identical in any case. It has been fixed to 12 kA, which gives a main field B_0 of 13 T without iron yoke. Results are presented in Table 4.3.c.

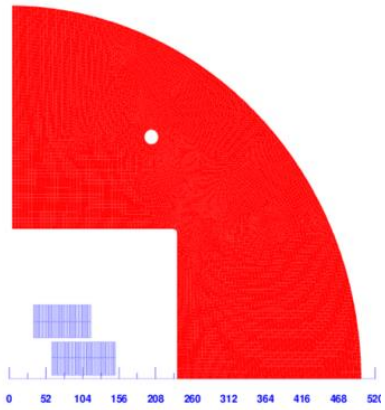

Fig. 4.3.5 – Scheme of the iron yoke.

[1] The mechanical parts of the magnet structure are defined and described extensively in chapter 5.

Table 4.3.c – CONTRIBUTION OF THE IRON YOKE TO THE CENTRAL FIELD (at 12 kA)		
R_{yoke} [mm]	B_0 [T]	Contribution to B_0 [%]
none	13	-
500	14.37	+ 10.5
450	14.19	+ 9.2
400	13.97	+ 7.5
350	13.72	+ 5.5
320	13.54	+ 4.2

The effect of the yoke radius on the central field is important (+4% with R_{yoke} = 320 mm; +10.5% with R_{yoke} = 500 mm). Hence, for a fixed target B_0, the current at short sample limit can be reduced in the coil with a larger yoke. At first glance, the largest reasonable yoke thickness (500 mm) looks preferable.

A second study has been led with **iron pads** in the magnet structure. There are four pads in total in the structure: two vertical ones and two horizontal ones. Using iron there allows increasing again the central field for a fixed current. However, it is less favorable on the mechanical point of view because it increases the number of material types used around the coil and it supposes to use laminations. Four cases have been compared (see Figure 4.3.6): all four pads in iron, all four pads non-magnetic, only vertical pads in iron and only horizontal pads in iron. Results are presented in Table 4.3.d.

Table 4.3.d – CONTRIBUTION OF IRON PADS TO THE CENTRAL FIELD (at 12 kA)		
Configuration	B_0 [T]	Contribution to B_0 [%]
All pads non-magnetic	13	-
All pads in iron	13.91	+ 7.0
Vertical pads in iron	13.66	+ 5.1
Horizontal pads in iron	13.24	+ 1.9

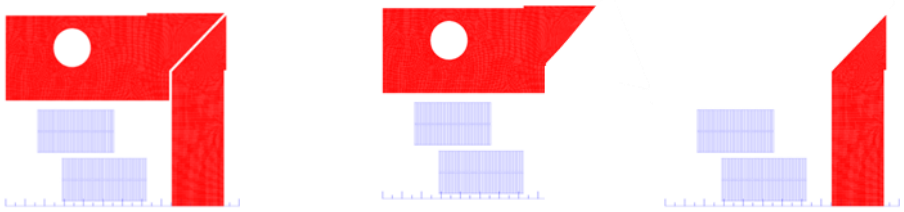

Fig. 4.3.6 – Scheme of the iron location (irons is represented in red): all pads (left), vertical pads only (mid), horizontal pads only (right) .

Having all the pads in iron increases the central field by 7%. The contribution of the horizontal pads is much lower than the one of the vertical pads. It has been decided to keep the horizontal pads non-magnetic, which is better on the mechanical level [4.4]. Finally, it has been decided to work with a 450 mm iron yoke and with vertical pads made of iron. The gain in terms of B_0 with a 500 mm iron yoke is very limited when using iron in the vertical pads [4.5].

Next step is to understand the influence of magnetic posts. Using a magnetic central post is counter-productive, as it tends to reduce the magnetic flux density in the bore tube and to increase it on the coil [4.6]. In the following, only the option of an iron top post is considered. The analysis has been done for different coil layouts. Conclusions show that an iron top pole decreases significantly the peak field on the coil (around 5%) as it concentrates more the flux lines toward the center. This option has been retained [4.7].

The possibility ta have a top pole in FeCo instead of Magnetil has been proposed. The aim was to decrease further the peak field thanks to the higher saturation field of FeCo (2.35 T) [4.8]. Calculations have shown that a FeCo top pole permits to decrease the peak field by 0.7% and the current by 1.3%, which increases the margin. However this very limited benefit must be confronted to the price of FeCo which is three times more expensive than Magnetil iron. Considering this, this option has been discarted.

Conductor repartition

Apart from the layout mentioned earlier ("41-41-37-37"), different configurations with different conductor repartitions have been studied. The first one has 39 turns in each layer ("39-39-39-39"), which facilitates winding and avoids corners in the magnet section. The second configuration has 36 turns in the lower layers and 42 turns in the upper ones ("36-36-42-42"). The third layout has 39 turns in the lower layers and 45 turns in the upper ones ("39-39-45-45"). The overall number of turns is increased here to 168, which makes the field higher.

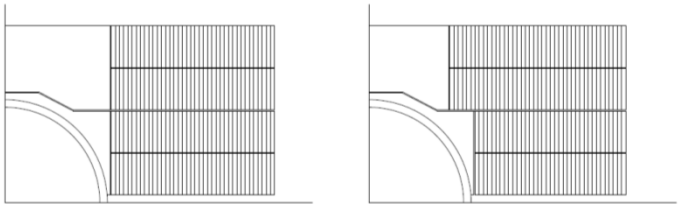

Fig.4.3.7 – Configuration "39-39-39-39" (left) and "36-36-42-42" or "39-39-45-45"(right)

In the three latter cases, the width of all the double-pancakes is identical. This presents a great advantage in terms of conception of the coil pack elements. Moreover, this limits the risk of misbalance during lateral pre-stress.

The four iron configurations described in the previous paragraph have been compared for each layout. In every case, for B_0 fixed to 13 T (at 4.2 K), the use of iron everywhere reduces the current by 20% or more and increases the short sample field by 1 T or more at 1.9 K. The horizontal position of the first block is 56 mm here and its vertical position is 4 mm.

Table 4.3.e presents the results with iron everywhere. Using non-magnetic horizontal pads as proposed earlier would slightly change the values, but it wouldn't affect the conclusions.

In the following, b_i is defined as $b_i = \frac{Bi}{B0} . 10^{-4}$

Table 4.3.e - COMPARISON BETWEEN 2D MAGNET LAYOUTS (WITH IRON)			
Layout	39-39-39-39	36-36-42-42	39-39-45-45
Number of turns	156	156	168
B_0 [T]	**13**	**13**	**13**
I [kA]	9.9	9.9	9.4
B_{peak} [T]	13.6	13.09	13.11
B_{ss} at 4.2 K [T]	15.49	15.99	16.17
B_{ss} at 1.9 K [T]	16.80	17.34	17.51
Load line margin at 13 T, 4.2 K [%]	16.1	18.7	19.6
Load line margin at 13 T, 1.9 K [%]	22.6	25.0	25.8
b_3 at 2/3 of the aperture	199.3	31.5	39.1
b_5 at 2/3 of the aperture	29.4	25.3	24.1
b_7 at 2/3 of the aperture	-2.6	2.3	2.3
$\sum F_x$ per quadrant, at 13 T [MN/m]	7.6	7.9	8.0

The horizontal forces are similar for each layout.

The first layout is geometrically simpler, but it has an important sextupole field (b_3 ~ 200). The third layout improves the margin but utilizes much conductor. The "36-36-42-42" layout is the best in terms of field quality (b_3 = 31.5). With iron everywhere and for a central field of 13 T, it has a peak field of 13.09. This is very efficient. The margin remains very good. **This comparative study is clearly in favor of the "36-36-42-42" layout** [4.9]**, which is retained in the following.**

Vertical position of the layers

First idea could be to position the layers along the midplane in order to get the largest possible contribution to the central field and the best margin. However, this option is not the best in terms of field quality. Additionally, free space between the coils is necessary for insulation and instrumentation (see § 4.6).

The influence of the vertical position of the conductor layers on the magnetic field is analyzed. The vertical distance between first layer and the midplane is the parameter (values of 3 mm, 3.5 mm and 4 mm are considered). Calculations are done on layout "36-36-42-42" with a horizontal position of the first block of 58 mm and with iron in the yoke and in the pads. The distance between the layers in a pole is set to 0.5 mm.

Table 4.3.f – INFLUENCE OF THE VERTICAL POSITION OF THE LAYERS ON THE MAGNETIC FIELD					
Position on the median plane [mm]	I_c at B_0 = 13 T [kA]	b_3	b_5	B_{peak} [T]	Margin on the load line at 4.2 K [%]
3	10.5	67	-19	13.2	17.3
3.5	10.54	57	-20	13.15	17.4
4	10.58	48	-21	13.15	17.4

The magnetic results are similar. Hence, the choice has been driven by the design of the traces and insulation. A value of 3.5 mm has been retained.

Horizontal position of the layers

Based on the experience from LBNL, it has been decided early in the project to align the four layers of a pole in the horizontal direction along their external edge. This is meant to avoid corners in the section that could create mechanical stress zones during operation. It has also been decided to have the same number of turns in the two layers of a single coil (1 and 2 or 3 and 4). This is meant to facilitate the fabrication tooling.

The internal radius of double-pancakes 1-2 (including mechanical support) is imposed by the specification and by the insert (see § 2): FRESCA2 aperture must be 100 mm. Coil design must account for the mechanical parts. For these reasons, the internal position of coil 1-2 has been fixed to 58 mm (6 mm for mechanical support + 2 mm margin). Coils 1-2 having 36 turns, it leads to an external horizontal position of 137.92 mm (*i.e.* 58 + 36 x 2.22 mm). The constraint of having the four layers aligned on their external edge results in an internal radius of 44.68 mm for coil 3-4 (*i.e.* 137.92 – 42 x 2.22 mm).

Influence of the cable thickness

The 2D magnetic layout is now fixed. It has a consequence on the geometry of the posts of the coils (in particular their width is directly correlated to the horizontal position of the layers). If the cable thickness changes for some reason, coils 1-2 and 3-4 won't be aligned anymore. Shims would be added in that case but the horizontal position of layers would remain the same.

In order to evaluate the influence of such change in terms of magnetic field, different cases have been calculated with conductor thicknesses from 1.82 mm to 1.93 mm.

Three cases have been compared as shown in Table 4.3.g and Figure 4.3.8.

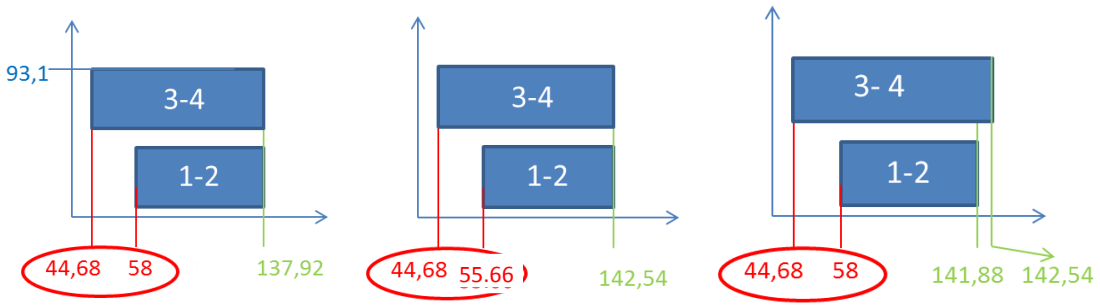

Fig. 4.3.8 – Scheme of the magnet layout in cases 1 (left), 2 (mid) and 3 (right).

The following table sums up the parameters and results of the study. In any case, the magnetic field is acceptable.

Table 4.3.g – INFLUENCE OF THE CABLE THICKNESS

Parameter	Case 1	Case 2	Case 3
Reacted cable width (bare) [mm]	21,3 (20.9 + 2%)	21,3 (20.9+ 2%)	21,3 (20.9+ 2%)
Reacted cable thickness (bare) [mm]	1.82 (no dilatation)	1.93 (1.82 + 4%)	1.93 (1.82 + 4%)
Insulation thickness (per face)	0.2	0.2	0.2
B_0 [T]	13	13	13
I [kA]	10.8	11.0	10.9
J_{eng} [A/mm²]	213	216	215
B_{peak} [T]	13.4	13.4	13.4
Load line margin at 13 T, 4.2 / 1.9 K [%]	17 / 23	17 / 23	18 / 23
Temperature margin at 13 T, 4.2 / 1.9 K [K]	3.0 / 5.3	2.9 / 5.3	3.0 / 5.2
b_3 at 2/3 of the aperture	67	67	72
b_5 at 2/3 of the aperture	28	27	21

4.3.2 Nominal magnetic design

Previous analysis has led to an efficient and optimized magnetic layout, accounting for the external constraints and based on an insulated cable section of 21.8 mm x 2.22 mm.

Following the development presented in § 3.2, the conductor section has been finally set to 20.9 mm x 1.82 mm at room temperature, with a transposition pitch of 120 mm. Insulation thickness around the conductor is in the 0.15 - 0.2 mm range (per side). During reaction, the dilatation of the conductor is estimated to 2% in height and 4% in thickness. The insulation is assumed to show no dilatation. Hence, final conductor section is 21.318 x 1.89 mm² without insulation, *i.e.* 21.618 x 2.19 mm² with 0.15 mm insulation or 21.718 x 2.29 mm² with 0.2 mm insulation (see Figure 3.4.1).

The magnetic layout can be summarized as follow:

- There are four horizontal layers per pole in block configuration. They are nominally aligned on their external edge, but slight misalignment may occur if the actual cable thickness is not exactly 2.22 mm.
- Layers 1 and 2 (from double-pancake coil 1-2) have 36 turns. Layers 3 and 4 (from double-pancake coil 3-4) have 42 turns. The overall number of turns is 156.
- The internal horizontal position of layers 1 and 2 is 58 mm; it is 44.68 mm for layers 3 and 4.
- The midplane insulation thickness is 7 mm, *i.e.* the vertical position of layer 1 in a pole is 3.5 mm. The interlayer insulation thickness is 0.5 mm inside of a double pancake (between layers 1 and 2 or 3 and 4). The inter-coil insulation thickness is 1.5 mm (between layers 2 and 3).
- The yoke, vertical pad and top post are made of iron.
- The iron yoke has an external radius of 450 mm.

The main magnetic parameters are listed in Table 4.3.h. For clarity, some results from the following 3D analysis are integrated in the table.

Parameter name	Symbol	Unit	Value
Table 4.3.h – 2D MAGNETIC LAYOUT: MAIN PARAMETERS*			
Nominal central field	B_0	T	13.0
Clear bore aperture diameter	Φ	mm	100
Number of turns in layer 1-2 / 3-4 (per quadrant)	N_t	/	36 / 42
Nominal current	I_{nom}	kA	10.9
Conductor peak field at I_{nom}	B_{peak}	T	13.4
Short sample current at 4.2 K / 1.9 K	I_{ss}	kA	13.8 / 15.1
Central field at I_{ss} (4.2 K / 1.9 K)	$B_{0,ss}$	T	16.0 / 17.2
Conductor peak field at I_{ss} (4.2 K / 1.9 K)	$B_{peak,ss}$	T	16.5 / 17.8
Position on the load line at 4.2 K / 1.9 K	ΔB	%	79 / 72
Magnetic field multipoles at 2/3 $Φ_b$	b_3	10^{-4}	71
	b_5	10^{-4}	-28
	b_7	10^{-4}	4
Inductance per unit length	L	mH/m	64
Stored magnetic energy per unit length at I_{nom}	$E_{mag,2D}$	MJ/m	3.8
Total stored magnetic energy at I_{nom} (from 3D analysis)	E_{mag}	MJ	4.6
Stray magnetic flux density at I_{nom} (at 1 m from the center)	B_{out}	T	0,1
Lorentz forces per unit length at I_{nom} (per quadrant)	F_X	MN/m	7.61
	F_Y	MN/m	-3.98

** thermal dilatation of the conductor is not considered here*

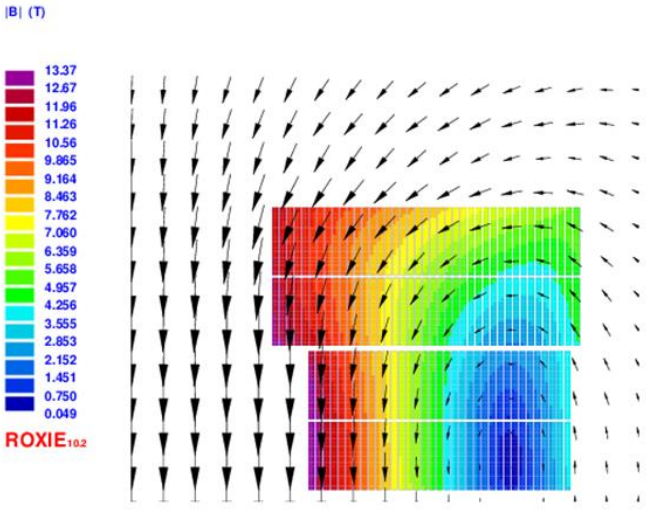

Fig. 4.3.9 – Final layout: 2D magnetic field
(thermal dilatation of the conductor is not considered here).

4.3.3 Model validation with the contracted cable section

Thermal dilatation of the conductor was not considered in the previous analysis. The nominal conductor section at room temperature was used in the model, which was sufficient for the parametric study. In the following, the thermal contraction of the conductor due to the cooling and the displacement due to the magnetization are considered [4.11].

The insulation is assumed to have no thermal contraction during cooling. Cable dilatation from 293 K to 4.2 K is described in ANSYS using orthotropic material properties. The major effect is a small keystone deformation of the blocks and a maximal displacement of -700 µm in the X-direction and -270 µm in the Y-direction.

The effect of magnetization is to push back the blocks outwards of maximum 120 µm in the X-direction.

The magnetic field is computed again on the base of the deformed conductor layout. Very little difference is observed with the results presented before (Table 4.3.h). **This validates the magnetic layout.**

Table 4.3.i presents the magnetic results in the worst configuration, accounting for a conductor displacement of 700 µm in the X-direction and 270 µm in the Y-direction. It is pessimistic because the maximal displacement in X and Y during cool-down doesn't actually occur at the same location. Comparison with Table 4.3.h shows that the geometrical effect of cooling-down and magnetization is negligible and doesn't affect our previous conclusions.

Parameter name	Symbol	Unit	Value
Table 4.3.i – 2D MAGNETIC LAYOUT: MAIN PARAMETERS AT 4.2 K*			
Central field at I_{nom}	B_0	T	13.09
Position on the load line at 4.2 K	$\Delta B_{4.2K}$	%	83
Position on the load line at 1.9 K	$\Delta B_{1.9K}$	%	77
Nominal current	I_{nom}	kA	10.9
Conductor peak field at I_{nom}	B_{peak}	T	13.4
Magnetic multipoles at 2/3 Φ_b	b_3	10^{-4}	73
	b_5	10^{-4}	-27
	b_7	10^{-4}	4
Inductance per unit length	L	mH/m	64
Stored magnetic energy per unit length at I_{nom}	E_{13T}	MJ/m	3.8
Stray magnetic flux density at I_{nom} (at 1 m from the center)	B_{out}	T	0.1
Lorentz forces per unit length at I_{nom} (per quadrant)	F_X	MN/m	7.65
	F_Y	MN/m	-4

** thermal dilatation of the conductor is considered here.*
Pessimistic conductor displacements of 700 µm (in X) and 270 µm (in Y) are considered.

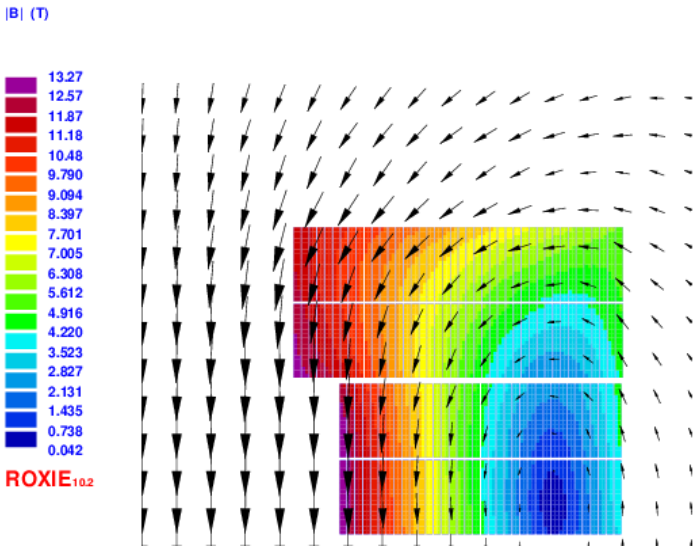

Fig. 4.3.10 – *Final layout after cool-down: 2D magnetic field (thermal dilatation of the conductor is considered here with pessimistic displacements).*

4.4 3D magnetic design

4.4.1 Ends geometry

2D coil layout is now fixed. Next step is to define the 3D parameters of the double-pancakes. As described earlier, FRESCA2 magnet is made of two identical poles, each of them comprising two different double-pancake coils named “coil 1-2” and “coil 3-4” (with respect to the name of the layers, see § 4.2).

The magnet length has been specified to 1500 mm. There is a strong geometrical constraint on the dipole structure which must let a net aperture of R50 mm *all along the coil*. This supposes to have flared ends, such as in the HD2 magnet from LBNL [4.12]. In order to account for the mechanical parts, it has been decided to impose a minimum clear bore of R61 mm to the conductor (*i.e.* 50 mm aperture + 10 mm for mechanics + 1 mm for tolerance management).

The vertical position of the coils is defined by the position of layer 1 (3.5 mm from the midplane). These constraints are represented in Figure 4.4.1. There are additional geometrical constraints on the pole dimensions, due to the reaction furnace.

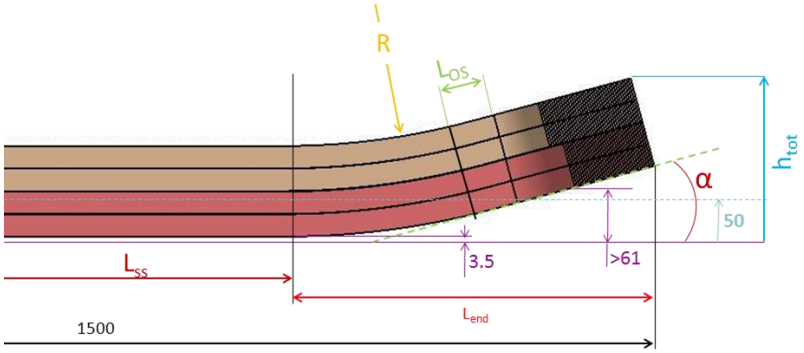

Fig. 4.4.1 – Constraints and parameterization of the double-pancake flared ends.

Schematically, the geometry of a flared coil falls into four parts:

- Straight section (extrusion of the 2D layout) defined by its length L_{ss}
- “Hard-way bend” section (HW) where the cable is bent in its main plane, defined by its radius R
- Inclined straight section (optional) interfacing HW and EW regions, defined by its length L_{OS}
- “Easy-way bend” section (EW) where the conductor is bent around the post before returning.

There are two driving parameters: the ramp angle α and the HW radius R. h_{tot}, L_{OS} and L_{SS} (= 1500 – 2 x L_{end}) can be derived geometrically from them. Constraints are: L_{ss} > 700 mm and h_{tot} < 200 mm (see § 2). Because of the cable stiffness, there is a minimum acceptable value for R. It has been fixed to 500 mm from the experience of LBNL (extrapolated to our cable width [4.12]) and verified with experimental tests (see § 8.1).

Figure 4.4.2 shows the results of the parametric geometrical study, varying R from 500 to 1000 mm (for fixed α) and α from 10 to 25° (for fixed R).

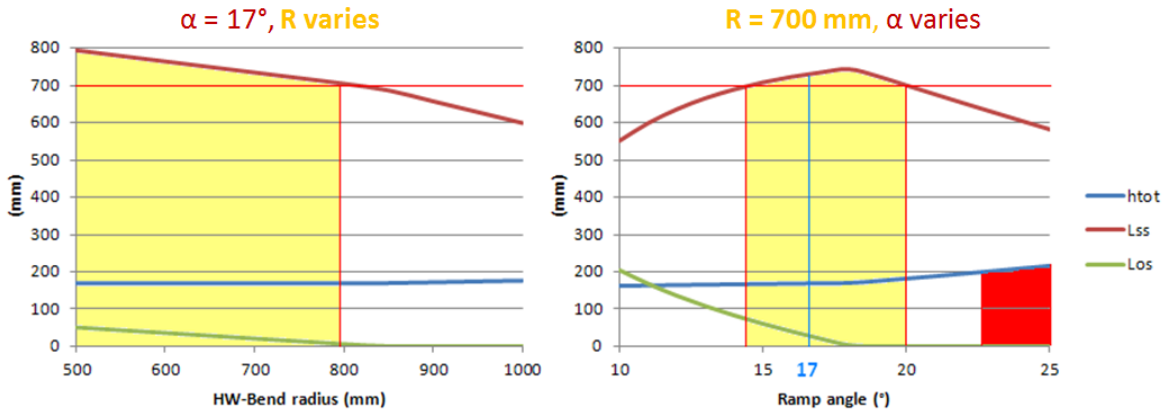

Fig. 4.4.2 – Parametric study of the ends geometry.

The regions in yellow are admissible. In order to have a long enough optional straight section (L_{OS} > 20 mm), the following compromise has been retained: ***α* = 17° and *R* = 700 mm.**

This analysis gives the approximate values of the ends parameter. A detailed engineering study has been led on that base, using a parameterized turn-by-turn CAD model. The final pole geometry is shown in Figure 4.4.3. We can note the slight difference between the two ends due to the intrinsic asymmetry of the coil (the *return end* on the left is symmetric while the *lead end* on the right is not).

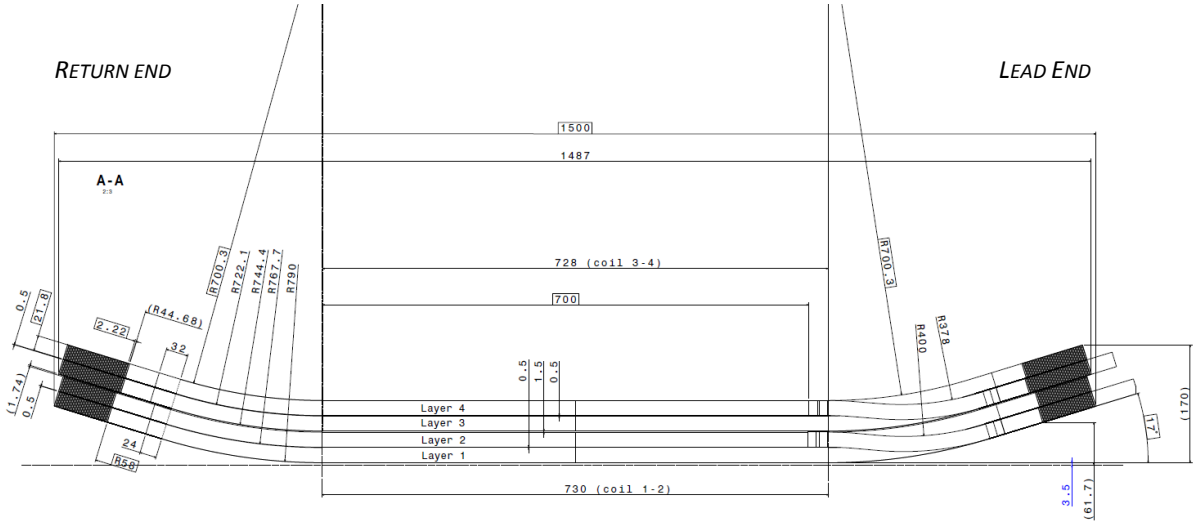

Fig. 4.4.3 – Final magnet geometry (one pole represented)
Main design parameters are framed.

Nota: In addition to this geometrical analysis, the return end geometry has been experimentally tried. Three options were compared: circular, elliptic or clothoidal bend (see § 8.1). As the test showed no major difference between them, the circular end has been retained.

4.4.2 Layer jump

In the case of Nb_3Sn, it is very difficult to solder the two layers of a double-pancake. Hence, it is preferable to respect cable continuity between both layers. Hence, a "layer jump" is necessary to connect the first turns of each layer. In order to avoid reducing the field quality in the "good field zone", it is not permitted to have it in the straight section.

Several geometrical options are possible. The jump can be located in the circular EW zone or in the HW zone. In the latter case, it is possible to take advantage of the ramp angle to go more on less smoothly from one layer to the other. Figure 4.4.4 shows three possible options.

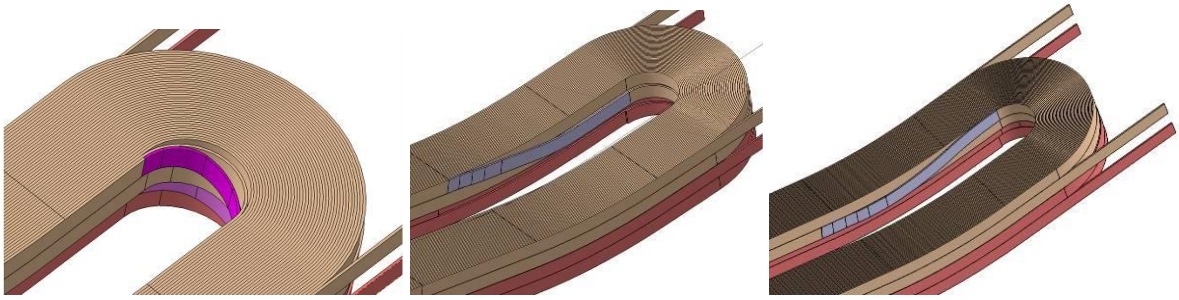

Fig. 4.4.4 – Possible layer jump geometries: "EW" (left), "HW soft" (center), "HW hard" (right)

Pros-and-cons analysis has been performed. It is summarized in Figure 4.4.4. "EW" option is localized and should be the best in terms of field quality, but it has been considered too much risky because of the cable width and stiffness. "HW soft" option has been retained because it has softer bending radii. In order to have a flat layer jump, it would be necessary to remove or to add turns in the 2D section. This would create corners in the magnet layout that are not desirable in terms of mechanics. To avoid that problem, it has been decided to integrate "chicanes" in the layer jump.

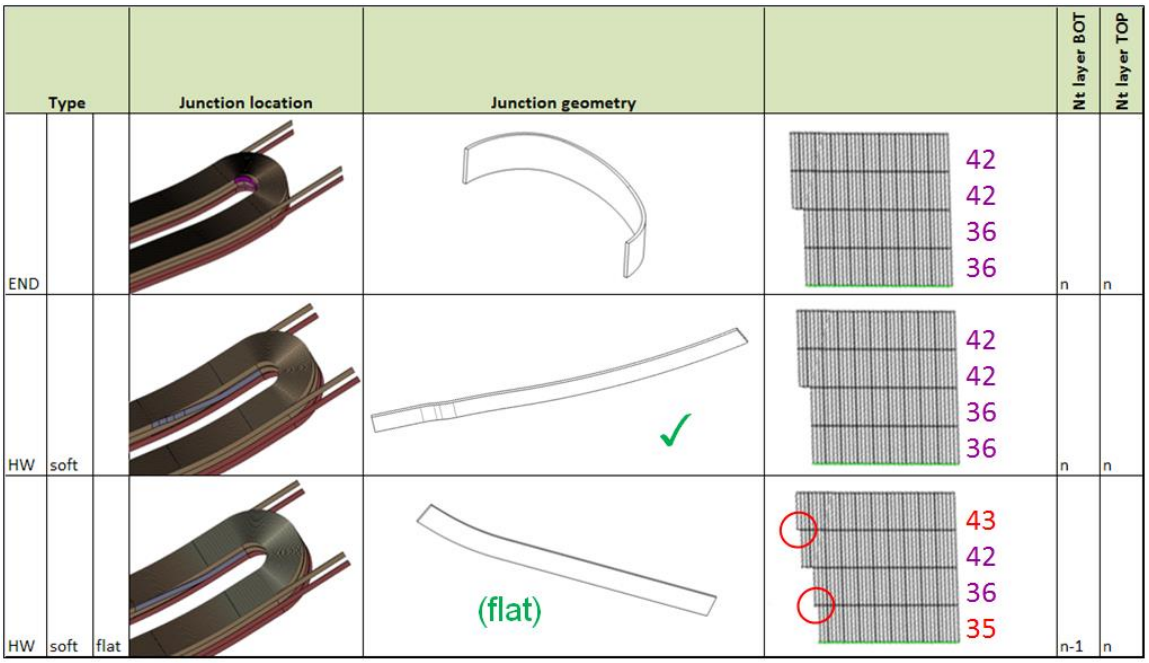

Fig. 4.4.4 – Qualitative comparison between main layer jump options

Figure 4.4.5 illustrates the final layer jump geometry, which consists in two parts: chicane and planar HW connection. Additional shim will be necessary to fill the space around the layer jump.

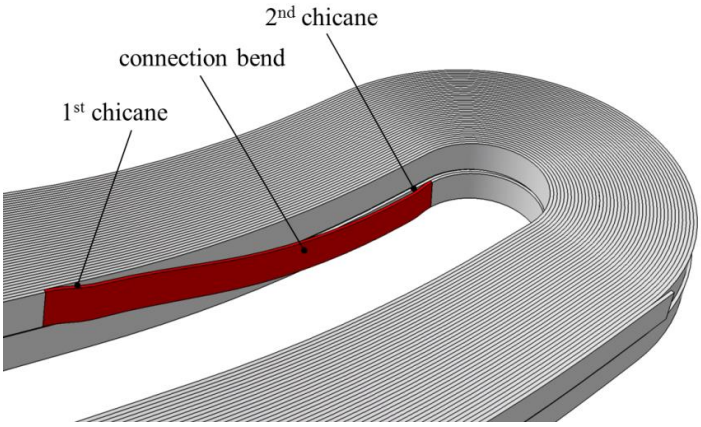

Fig. 4.4.5 – Final layer jump geometry.

Note that because of their different HW radii, the layer jumps of coil 1-2 and coil 3-4 are not exactly similar.

4.4.3 Magnetic field homogeneity

The 3D magnetic field corresponding to the final magnet geometry is computed using TOSCA/OPERA.

The magnetic optimization has been performed in 2D. The goal of the 3D calculations is to confirm the magnetic layout and to evaluate the field map in the straight section. It also gives us the peak field in the ends, which equals 12.3 T. Figure 4.3.6 shows the final magnetic field for a current of 10.9 kA.

As magnetic optimization has been performed in 2D, the goal of 3D calculations is to cross-check them in the straight section and to evaluate the peak field in the ends. A peak value of 13.2 T is obtained. Figure 4.4.6 shows the final magnetic field for a current of 10.9 kA. The peak field in the end is 10% lower than in the straight section.

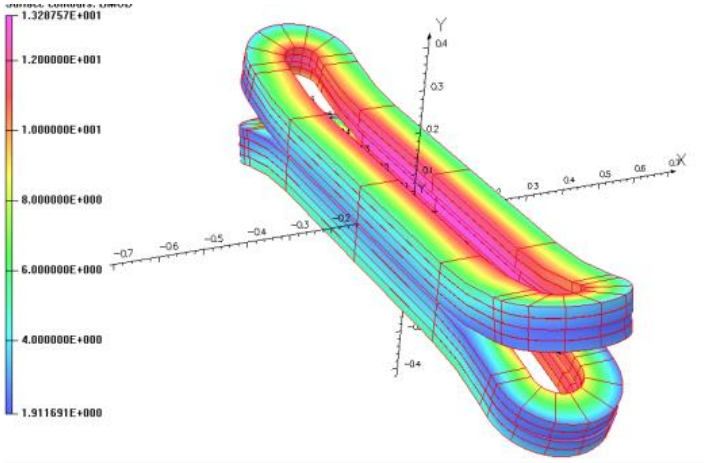

Fig. 4.4.6 – 3D final magnetic field.

The evolution of the magnetic field along the longitudinal axis is plot in Figure 4.4.7. The “1% homogeneity zone” has a length of 540 mm; the “2% homogeneity zone” has a length of 630 mm.

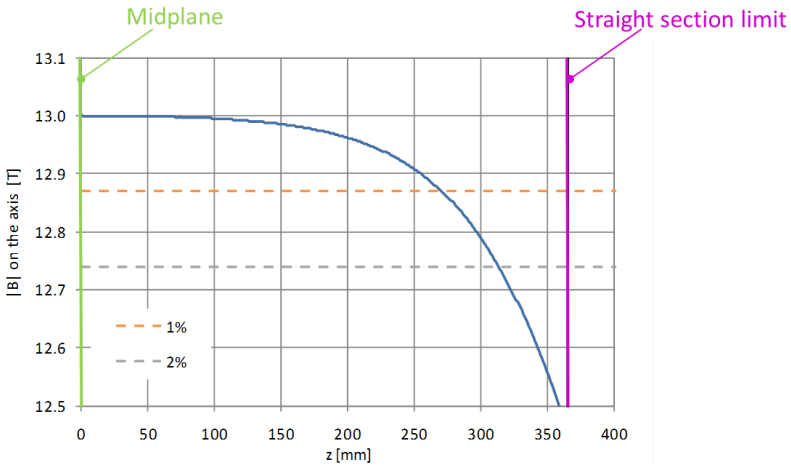

Fig. 4.4.7 –Magnetic field evolution along the longitudinal axis.

4.4.4 Cable length needs

The cable length needs corresponding to the magnetic analysis presented in this chapter are indicated in Table 4.4.a. A dipole roughly corresponds to one kilometer of cable, in four pieces.

Table 4.4.a – CABLE LENGTH NEEDS

Sub-element	Theoretical cable length [m]	+ 5% margin
Double-pancake 1-2	223	234
Double-pancake 3-4	253	266
1 POLE	476	500
FULL DIPOLE	**952**	**1000**

in one piece

4 pieces of cable

4.5 Protection study

First computations have been made using the QTRANSIT Fortran code. The quench thermal transient evolution is simulated in 3D in the magnet on the base of the quench propagation velocities and the resistance growth with time. Even if this very reliable code has been used and cross-checked with experimental results on several magnets, it is generally dedicated to large magnets that are indirectly cooled. Moreover, the usual formulas for propagation velocities strongly depend on the magnetic field (magneto-resistance, current sharing temperature) and they are obviously not uniform along the winding.

For these reasons, we decided to study the protection using the FEM code CAST3M, with procedures modified in order to take into account the decrease of current with time, which is directly related to the joule losses in the winding.

The 2D FEM study gives the evolution of the current decrease versus time for $t > t_{det}$ (detection time). It is represented in Figure 4.5.1.

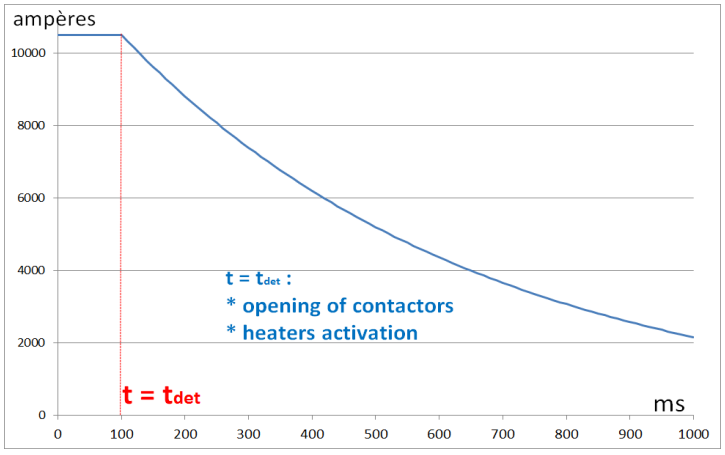

Fig. 4.5.1 – Evolution of the current during a fast discharge.

The computations led in 2D assume the heaters to be located uniformly all along the dipole. The discharge of the current is computed once the heaters are activated. As shown in Figure 4.5.1, it takes a time t_{det} to detect the quench. Heaters are then activated and contactors open, leaving the magnet discharge into the dump resistor. Then, the hot spot can be computed for each possible t_{det} from the hot spot criteria (Equation 1). The integral of J_0^2 only depends on t_{det} as we assume no decrease of the current during the expansion of the quench (this is a conservative assumption).

$$\int_{\theta_0}^{\theta_{max}} \frac{\gamma C(\theta)}{\rho(\theta)} d\theta = \int_0^{\infty} J^2(t)dt = \int_0^{t_{det}} {J_0}^2 dt + \int_{t_{det}}^{\infty} J^2(t)dt \qquad (1)$$

The principle of protection relies on the extraction of energy into a dump resistor *and* on the growth of the internal resistance due to heaters. Figure 5.1.2 illustrates the protection circuit.

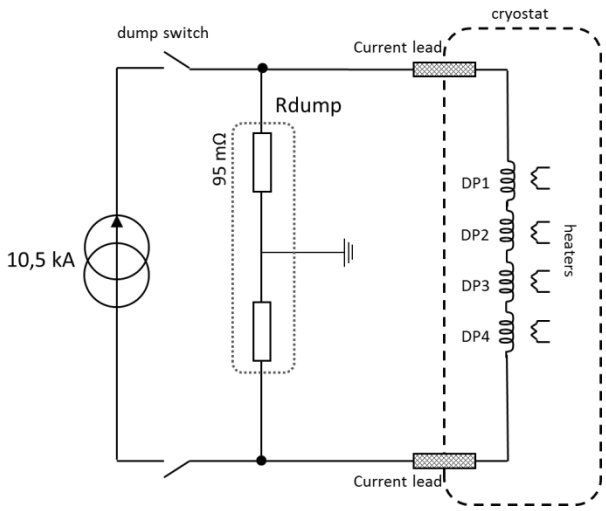

Fig. 4.5.2 – Protection circuit

A grounding circuit is used in order to divide the discharge voltage by two; the voltage at the terminals of the magnet is ± 500 V to ground. The resistance volume is set to 2.63 liters so that the voltage remains maximal as long as possible at the terminals.

Regarding the heaters, a power of 50 W/cm² is technically achievable. The power distribution is assumed uniform. It has been decided to take into account a heater power of 25 W/cm² in the model, considering that the real power distribution will not be uniform. The duration of the power pulse has been set to 50 ms.

The evolution of the quenched volume is shown in Figure 4.5.3. It takes about 450 ms to quench the dipole totally. The delay time is 20 ms between activation of the heaters and quench ignition in the dipole.

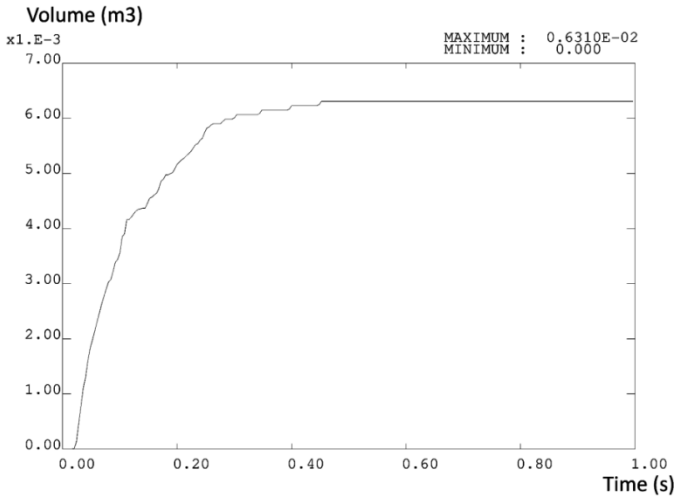

Fig. 4.5.3 – Evolution of the quenched volume.

Figure 4.5.4 gives the current evolution. It has a time constant (defined as *I/e*) of 520 ms.

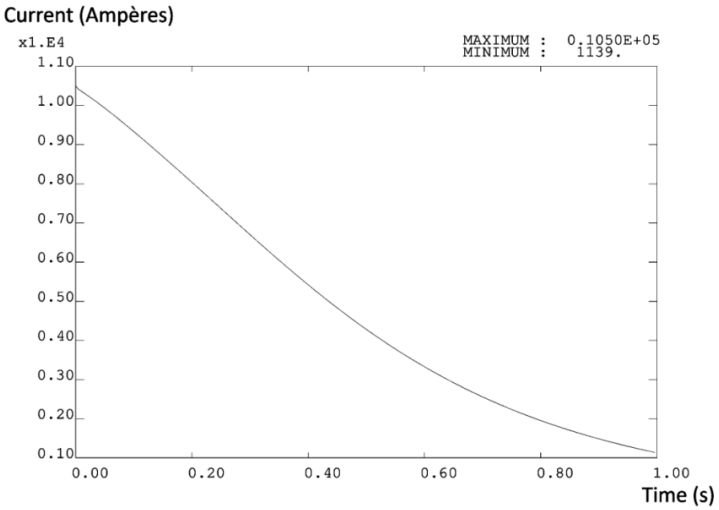

Fig. 4.5.4 – Current evolution.

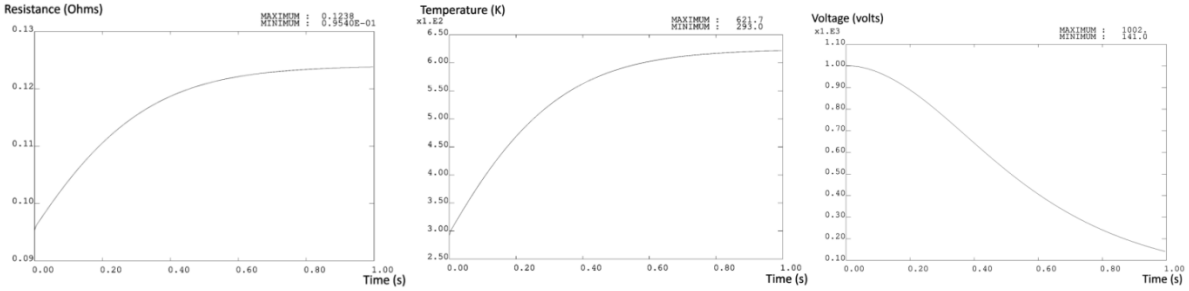

Fig. 4.5.5 – Evolution of dump resistance (left) temperature (mid) and voltage (right).

The value of the dump resistance increases by 30% during discharge. Its temperature increases up to 622 K at the end of the discharge, which is an acceptable value. The voltage at the terminals of the magnet remains maximal at the beginning of the discharge (zero slope) as was used for the volume computation mentioned *supra*.

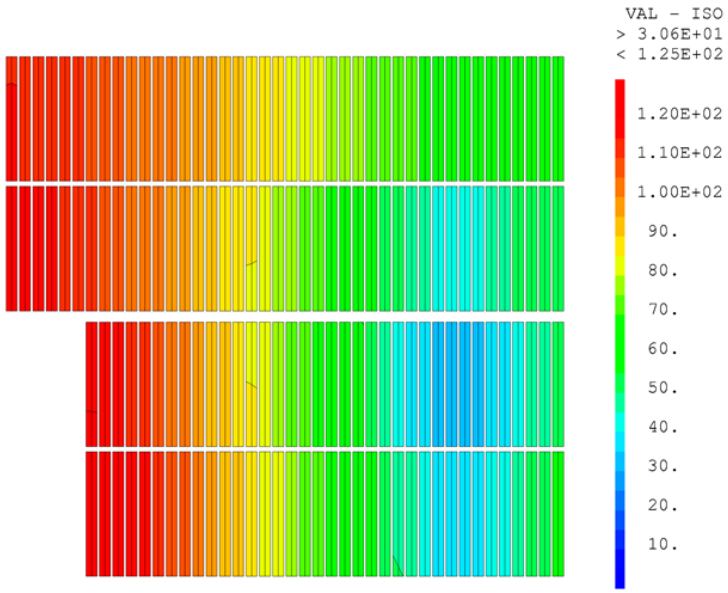

Fig. 4.5.6 – Temperature distribution within the dipole section at the end of the discharge.

Due to the heaters, the temperature is well distributed and the thermal gradients are kept low as shown on Figure 4.5.6.

From the current evolution (right part of equation 1), the adiabatic hot spot temperature is calculated and compared to the maximum temperature computed by the FEM code. The good accordance between both curves (Figure 4.5.7) allows us to compute directly (*i.e.* from the current evolution) the maximal temperature, taking into account the detection time.

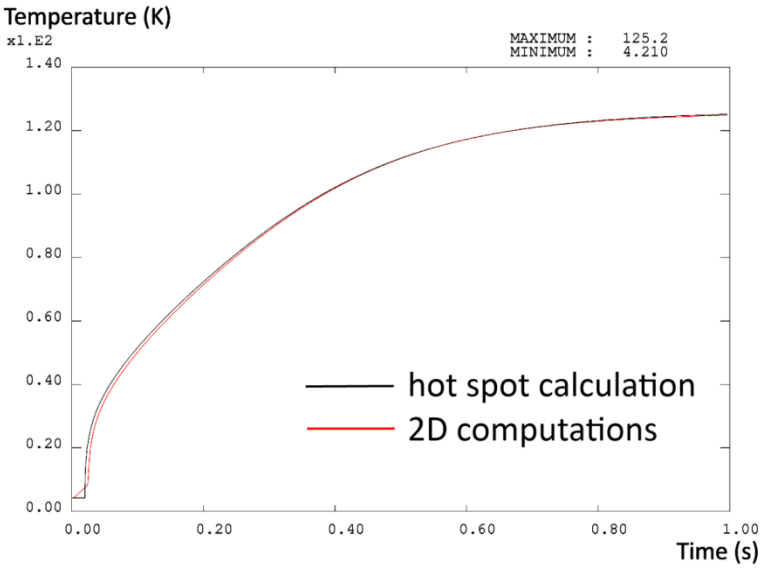

Fig. 4.5.7 – Comparison between hot spot and 2D FEM calculations.

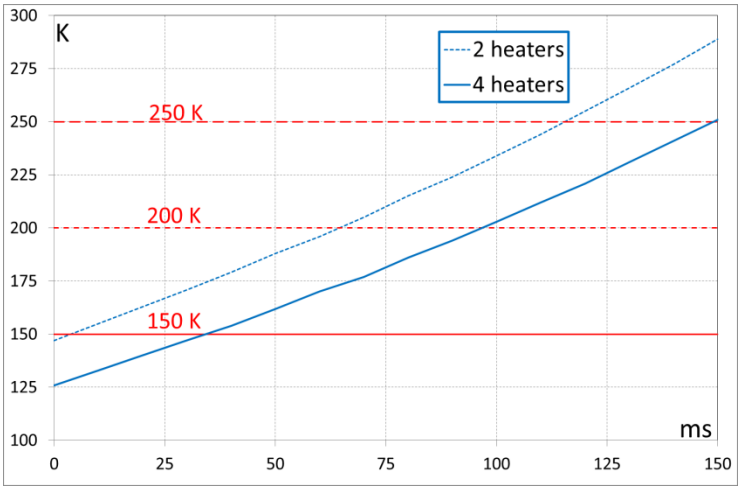

Fig. 4.5.8 – Maximal temperature versus detection time.

Figure 4.5.8 gives the hot spot temperature in the dipole, taking into account the detection time t_{det}. The detection must be lower than 40 ms if we want a maximal temperature below 150 K (with four heaters). Nevertheless, we expect a detection time of 100 ms: in that case, the maximal temperature is 203 K with four heaters. The maximal temperature difference is around 30 K if we use two heaters rather than four.

Using four heaters decreases the maximal temperature in the dipole and helps to distribute more uniformly the temperature (lower gradients).

As developed for the HTS insert [0.1], we studied the effects of a varying protection resistance, switching each time the voltage at its terminals goes below 800 V (Figure 4.5.9).

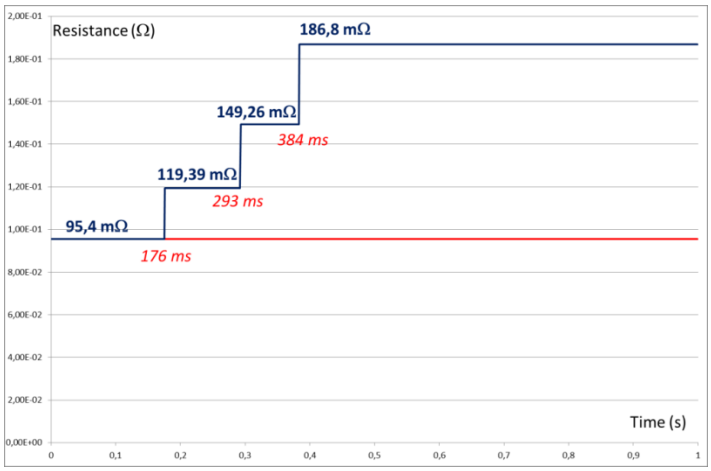

Fig. 4.5.9 – Varying protection resistance.

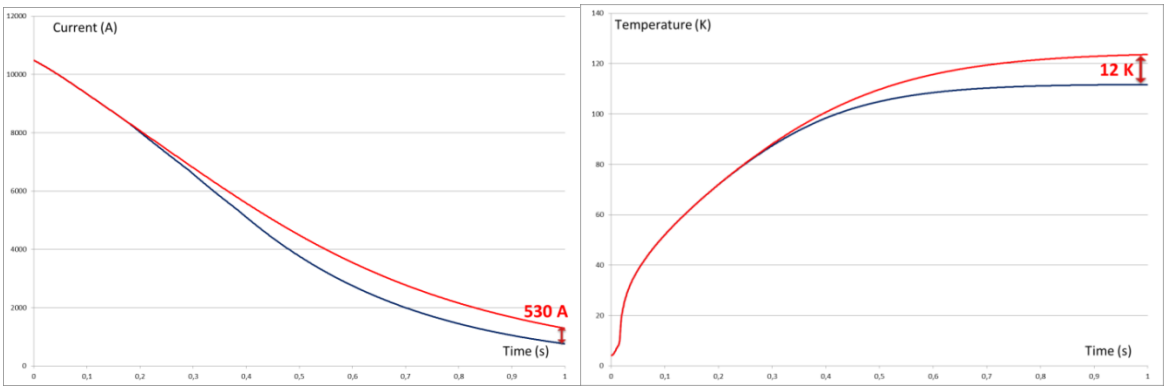

Fig. 4.5.10 – Current decrease and resistor temperature - varying protection resistance

Results are compiled in Figure 4.5.10. The current decrease is faster with the varying resistor: the MIITs[1] are then smaller and the maximal temperature within the conductor is reduced by 12 K. Nevertheless, the gain is low compared to the complexity of the electrical circuit. This is only an option.

[1] The "MIITs" parameters for magnet protection are derived from the energy balance as follow:

$$\int_0^{\infty} I(t)^2 dt = A_{cu} A_{tot} \int_{T_0}^{T_{max}} \frac{\sum_i \gamma_i c_{p,i}(T)}{\rho_{cu}(T)} dT = 10^6 \ \mathrm{MIITs}(T_{max})$$

4.6 Instrumentation

At nominal field, FRESCA2 has a total stored energy of 4.6 MJ (see § 4.3), significantly larger than the ones of the Nb_3Sn dipoles and quadrupoles built in the last decade (for example, the 3.7 m long LARP long quadrupole magnet LQ features 1.4 MJ [4.13]). However, as pointed out in [4.14], the stored energy density in the coil is comparable to the other magnets. The quench protection system for FRESCA2 relies on a dump resistor and quench heaters. The value of the external resistor is 95 mΩ, set so that the voltage at the terminals of the magnet never exceeds 1 kV, ±500 V to ground by means of the grounding circuit. A 2D model implemented in CAST3M [13] has been used to determine the parameters of the quench protection system (see § 4.5), under the assumption that quench heaters are placed on the outer surface of each layer, covering 50% of the total allowable surface and providing 50 W/cm² [4.15]. According to the computations, the detection time (from quench initiation to opening of the switch and activation of the heaters) must be lower than 40 (100) ms for a Tmax below 150 (200) K in the high field region. The quench heaters design, shown in Figure 4.6.1, is based on 25 µm thickness stainless steel strips with a 12 mm width. To cover the coil, whose width is 80 mm, we have two nested families of heaters, going from connection side to non-connection side and back, with a wiggling shape. The length of the heaters is 3.1 m, with a total surface per circuit of 370 cm², and a total resistance of 5.2 Ω. To get the required power, one needs 60 A, resulting in a voltage of 310 V at the end of each circuit.

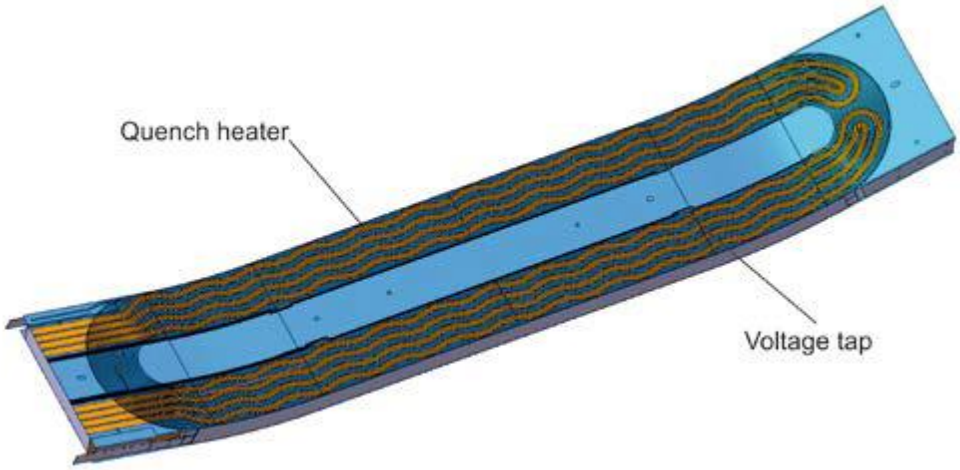

Fig. 4.6.1 – Quench heater trace design.

5. Structural design

5.1 Mechanical design

5.1.1 2D mechanical design

The coil design is based on a block layout (see § 4). It is represented in Figure 5.1.1. Each pole is made of four layers, wound as two double pancakes. The total number of turns per pole is 156, with 36 spires in layers 1 and 2, and 42 in layers 3 and 4 (the layers are numbered from the midplane outwards). Layers 1 and 2 are formed from a continuous length of cable, and so are layers 3 and 4. The two double pancakes of a pole are individually wound, reacted and instrumented. They are impregnated with the respective central posts and horizontal rails. The 100 mm aperture is given by the assembly of the two inner central posts, without any additional component. Each double-layer coil includes 0.5 mm thick fiber-glass insulation between the layers and two 300 µm thick insulated traces for quench protection and instrumentation on the external faces. The contact between coils is provided by the poles and by an inter-coil (or midplane) shim. The inter-coil shims will be made by fiberglass sheets impregnated with epoxy in-between the coils and mold-released, so to ensure uniform coil-to-coil contact, at the same time allowing detachment and replacement of individual coils.

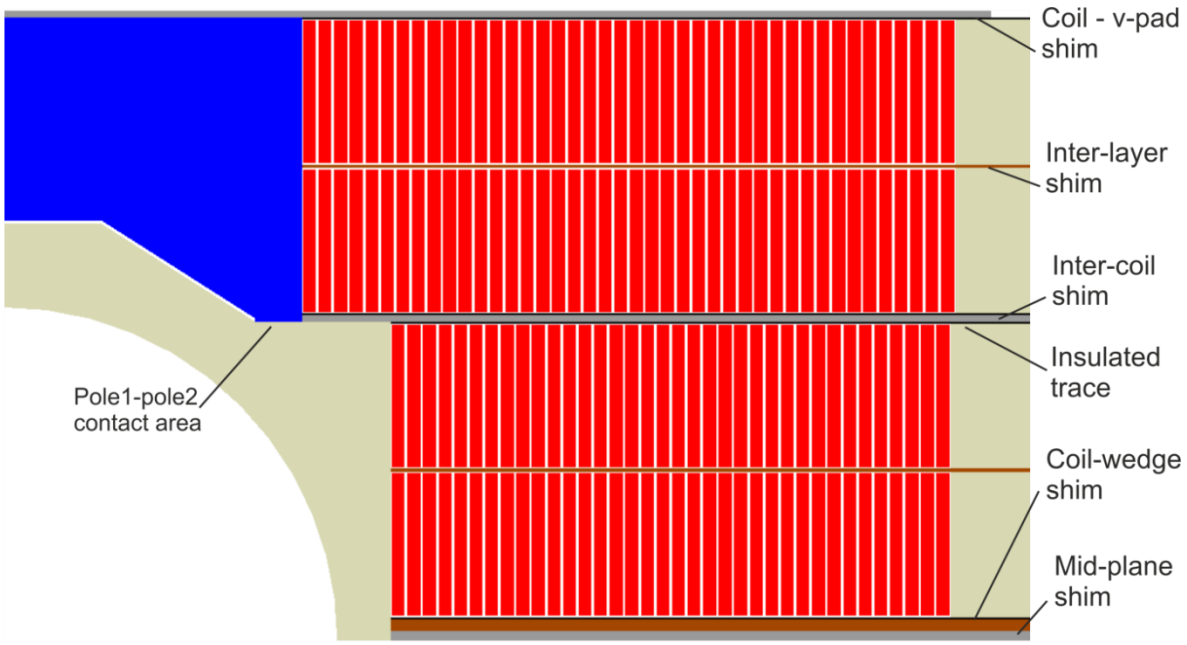

Fig. 5.1.1 – Coil cross-section and insulation scheme.

The choice of this 2D layout for the coil, with no spacers in the cross-section and rectangular-like aligned double pancakes, has been favored mostly because it results in a minimum number of discontinuities of geometry and materials around the Nb_3Sn coil. A secondary effect is the expected ease of manufacturing and shimming [1.6].

As presented above, this layout limits de facto the number of degrees of freedom available for magnetic optimization to four (not considering the iron geometry): the total number of turns, the relative number of spires in coil 1-2 *vs*. coil 3-4, the position of the first cable in layer 1 and the thickness of the mid-plane shim. The objectives are multiple: sufficient margin on the load line, field uniformity in the aperture at high current, limited peak field on the coil. The main mechanical constraint is the thickness of the inner central post.

In the baseline coil layout, the first conductor of layers 1-2 is wound at a distance of 58 mm from the center, whereas the mid-plane shim thickness amounts to 2 × 3.5 = 7 mm (§ 4.3). These values have been chosen giving a heavier relative weight to field strength with respect to field quality. In this case, in fact, the random harmonics and the nonlinear contribution of the iron might shadow the importance of reducing the allowable harmonics. Furthermore, the priority for this model is to reach the nominal flux density, with relaxed field quality requirements.

The coil and magnet parameters are summarized in Table 4.3.h. At the nominal bore field of 13 T, the conductor peak field of 13.4 T is located in the straight section of the pole turn in layer 1, the other layers having a field margin ranging from 1% in layer 2 to 9% in layer 4. In the nominal condition the magnet current will be 79% (72%) of the maximum "short-sample" current I_{ss} at 4.2 (1.9) K. The peak field in the end is 10% lower than in the straight section, and the 1% uniform field region is 540 mm long.

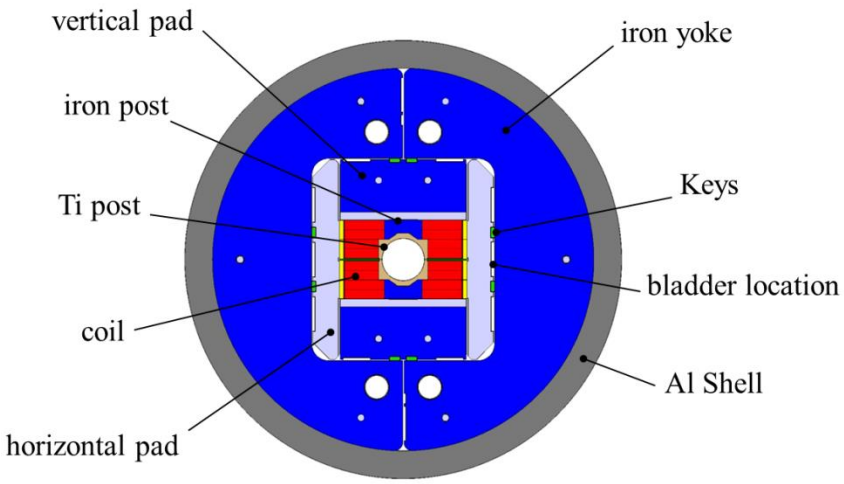

Fig. 5.1.2 – Magnet structure cross-section.

The mechanical structure is based on the so-called bladder and key concept. This approach was developed at LBNL [5.1] and it has been successfully used in several model magnets. With reference to Figure 5.1.2, the coil is surrounded by pads in the horizontal and vertical directions. These pads transfer forces to the outside split iron yoke through keys (mostly in the perpendicular directions). These forces on the iron are finally contained by a 65 mm thick aluminum alloy cylinder. During assembly, bladders are inserted next to the keys and pressurized, in order to create a clearance. This is used to shim the keys before the bladders are removed, so that the final assembly at room temperature involves interferences. The coil is equally compressed on average both on the central post side and on the pad side. During cool-down, the external cylinder tends to shrink more than the other components and provides an additional pre-stress to the coil. During powering, the Lorentz forces tend to separate the coils from the central islands, so that these interfaces are gradually unloaded as the current in the magnet rises.

The design aims at providing adequate pre-stress to the coil throughout the various stages, in particular limiting peak stresses at cryogenic temperatures and maintaining the cable supported along the central posts at the nominal current. The general strategy here is to provide full pre-stress with respect to the Lorentz forces.

The two double layers experience different Lorentz forces (F_x for block 3-4 is about 30% more than for block 1-2). Furthermore, they see a different stiffness in the central region, as in the case of block 1-2 a rather thin titanium alloy island is used, whereas for block 3-4 a solid iron piece is present. Titanium alloy has been chosen because of its high stress carrying capabilities, also in tension, and for its thermal contraction behavior; the iron post comes mostly from magnetic considerations (§ 4.3.1). Two lateral keys per side are used instead of a single one: in this way, the forces are better aligned with the coil, especially around the ends. The horizontal pad is in stainless steel; the vertical pad is made of a stainless plate in contact with the coil and has an iron insert along the straight section. The mid-plane shim is in G11.

The stresses in coil and support structure were computed with a 2D finite element mechanical model (see Figures 5.1.3 and 5.1.4). The contact surfaces of the impregnated coil (*i.e.* coil blocks and pole pieces) are assumed bonded, while all the other surfaces are modeled under the assumption of "sliding with separation allowed" with a friction factor of 0.2.

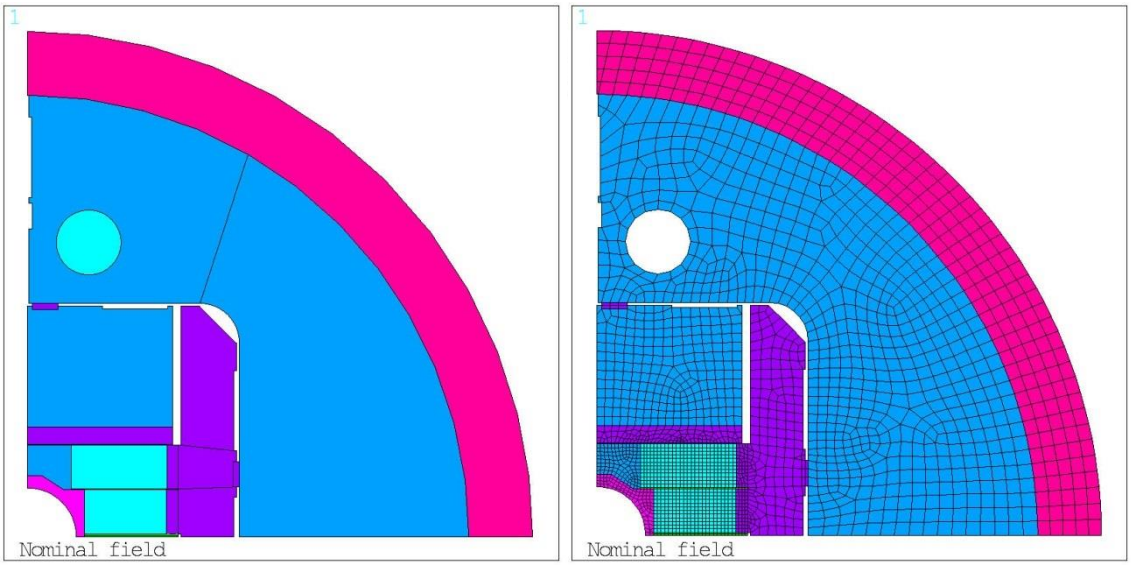

Fig. 5.1.3 – 2D finite element model of the magnet cross-section: areas (left) and elements (right).

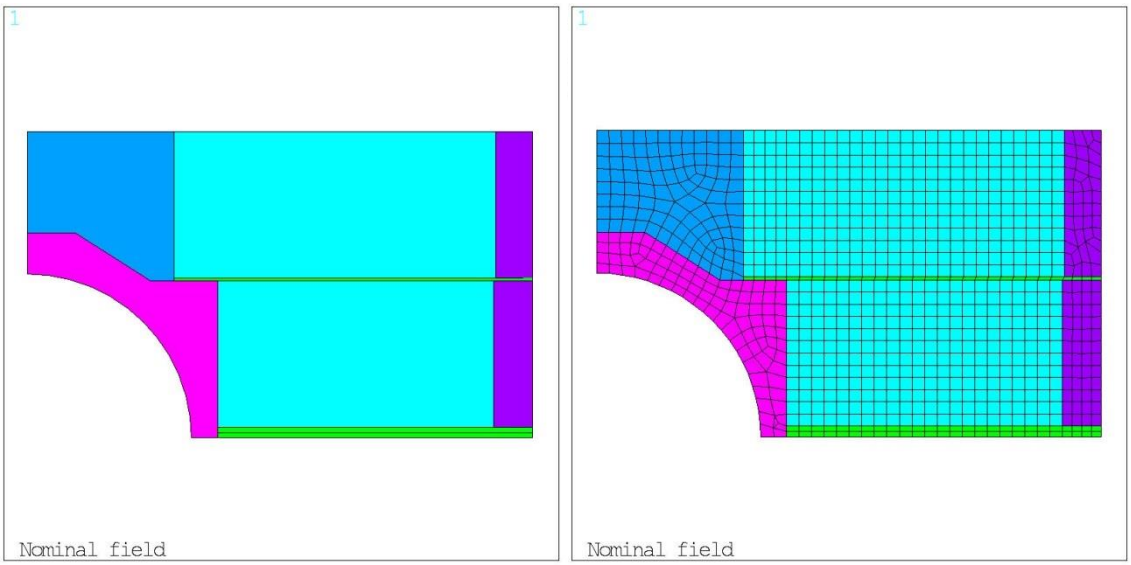

Fig. 5.1.4 – 2D finite element model of the coil cross-section: areas (left) and elements (right).

The following material properties have been considered in the models:

Table 5.1.a – MATERIAL PROPERTIES USED IN THE MODELS

Material	Localization	E_Y at 4.2 K [GPa]	E_Y at 293 K [GPa]	ν	$\int \alpha_{th}\, dt$ 293 – 4.2 K [mm.m^{-1}]
Insulated conductor[1]	Coil	42	30	0.30	3.9
MAGNETIL iron	Yoke / Y-Pad / Top post	224	213	0.28	1.97
304L steel	X-Pad / Y-Pad (3D) / Keys / Rails / End-plate	210	193	0.28	2.84
Titanium Ti-6-Al-4V	Central post	120	110	0.30	1.80
Aluminum 7075 T651	Shell	79	70	0.34	4.20
G10 (through thickness)	Insulation	30	30	0.30	7.06

[1] *measurements on-going (§ 3.4)*

The electromagnetic forces, listed in Table 5.1.b, tend to separate the turns from the pole pieces, compressing the coil blocks towards the side rails. The shell pre-load is therefore selected so that the contact region between the pole turns and the pole pieces are (in average) in compression when electromagnetic forces, generated by a field of 13 T, are applied. The nominal horizontal interference for a proper lateral pre-load around the coil at 13 T is 600 µm. Simulations show that such an interference can be locked in using reasonable pressures in the bladders (in the order of 350 bar). The average pressures between coil and central pole are shown in Figure 5.1.5 for four steps: room temperature after bladder inflation, room temperature after key insertion and bladder deflation, cryogenic temperature, and for a central flux density of 13 T. The pressure at 293 K and 4.2 K on the coil-to-central-post side it increases from the mid-plane outwards (*i.e.*, from layer 1 to layer 4). This effect is in part unavoidable, due to the presence of the bore, and in part wanted, to better match the distribution of the Lorentz forces. At full field, the mid-position of each layer exhibits still significant contact pressure, and tension is observed only on the top corner region of layer 4.

Table 5.1.b – ELECTROMAGNETIC FORCES (at I_{nom})

Coil 1-2	F_X	per quadrant	MN/m	+3.4
	F_Y	per quadrant	MN/m	-0.5
	F_Z	per octant	kN	+200
Coil 3-4	F_X	per quadrant	MN/m	+4.3
	F_Y	per quadrant	MN/m	-3.6
	F_Z	per octant	kN	+520

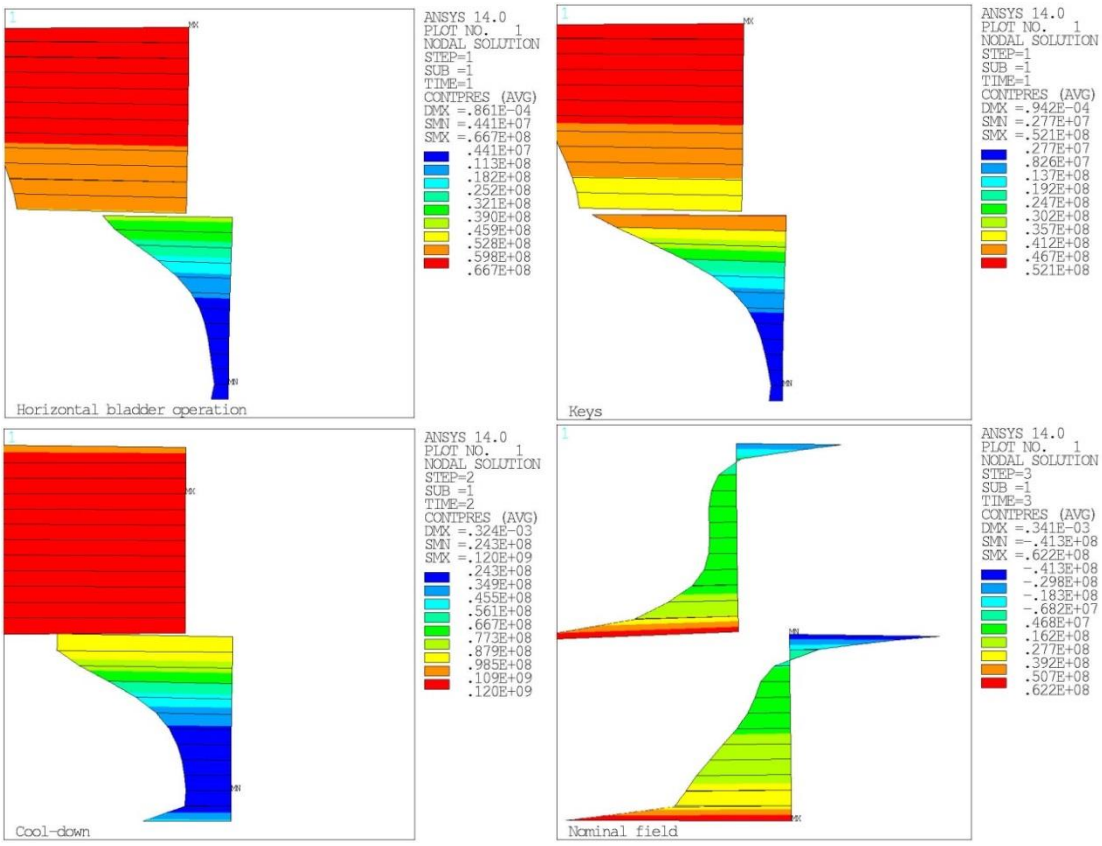

Fig. 5.1.5 – Computed contact pressure coil-pole (positive-pressure, negative-tension) during bladder inflation (top left), after key insertion and bladder deflation (top right), after cool-down (bottom left), and at 13 T (bottom right).

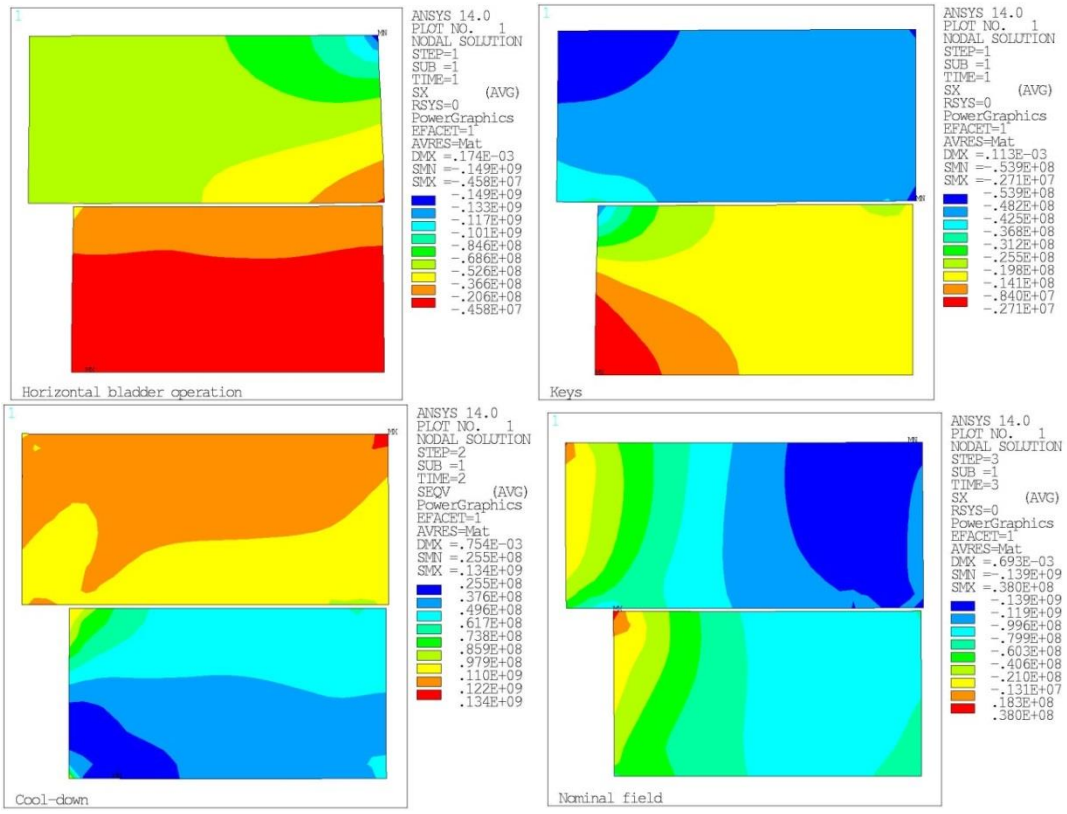

Fig. 5.1.6 – Computed coil horizontal stress during bladder inflation (top left), after key insertion and bladder deflation (top right), after cool-down (bottom left), and at 13 T (bottom right).

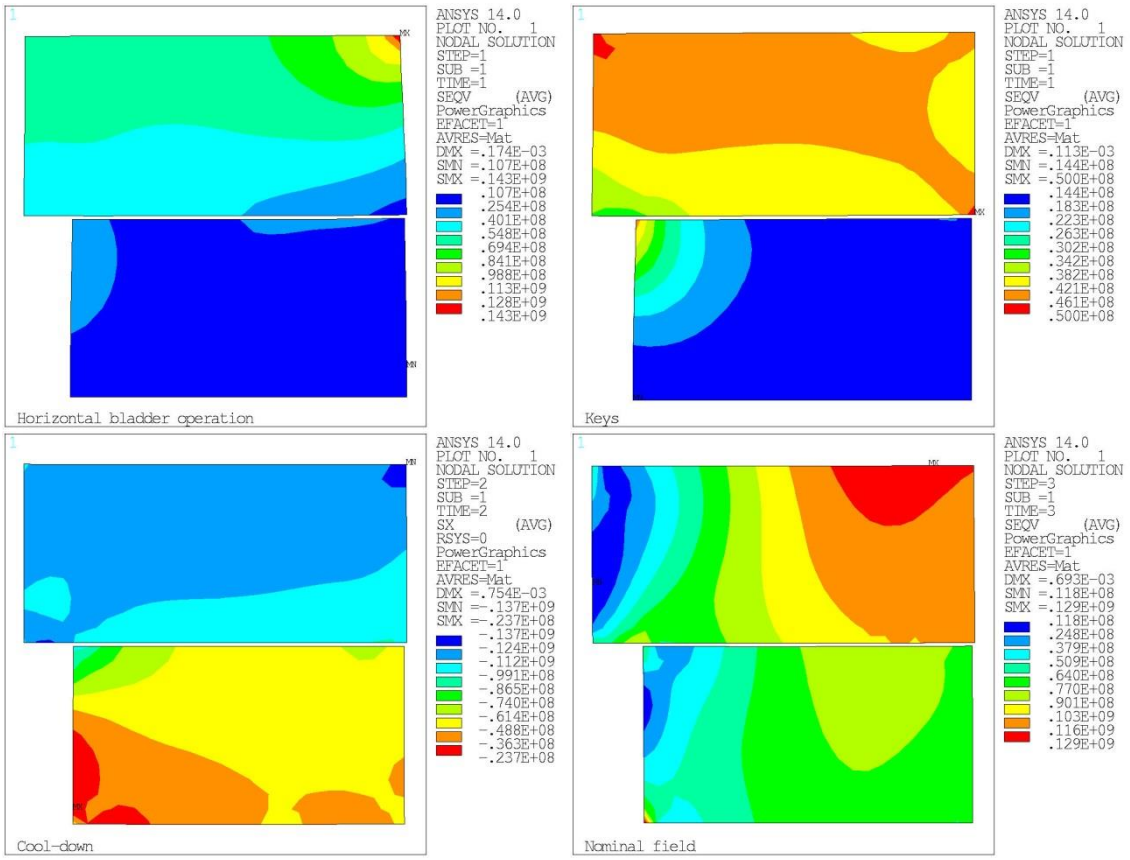

Fig. 5.1.7 – Computed coil Von Mises stress during bladder inflation (top left), after key insertion and bladder deflation (top right), after cool-down (bottom left), and at 13 T (bottom right).

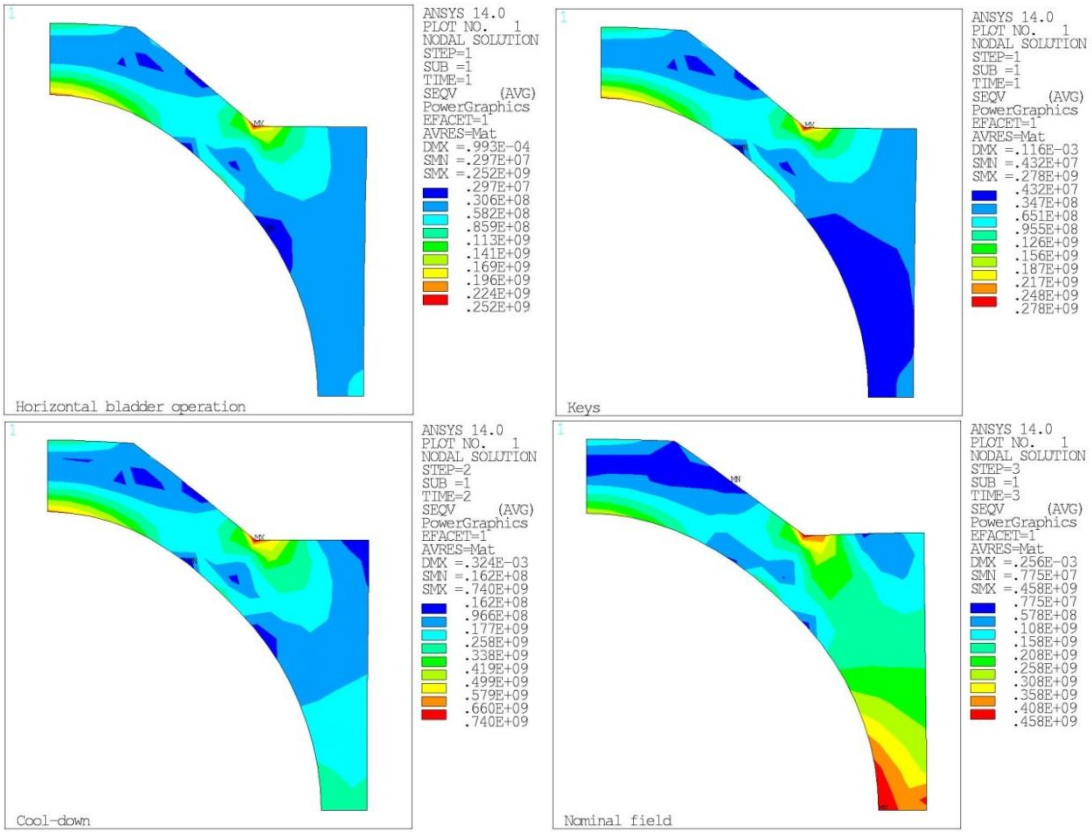

Fig. 5.1.8 – Computed pole 1 Von Mises stress during bladder inflation (top left), after key insertion and bladder deflation (top right), after cool-down (bottom left), and at 13 T (bottom right).

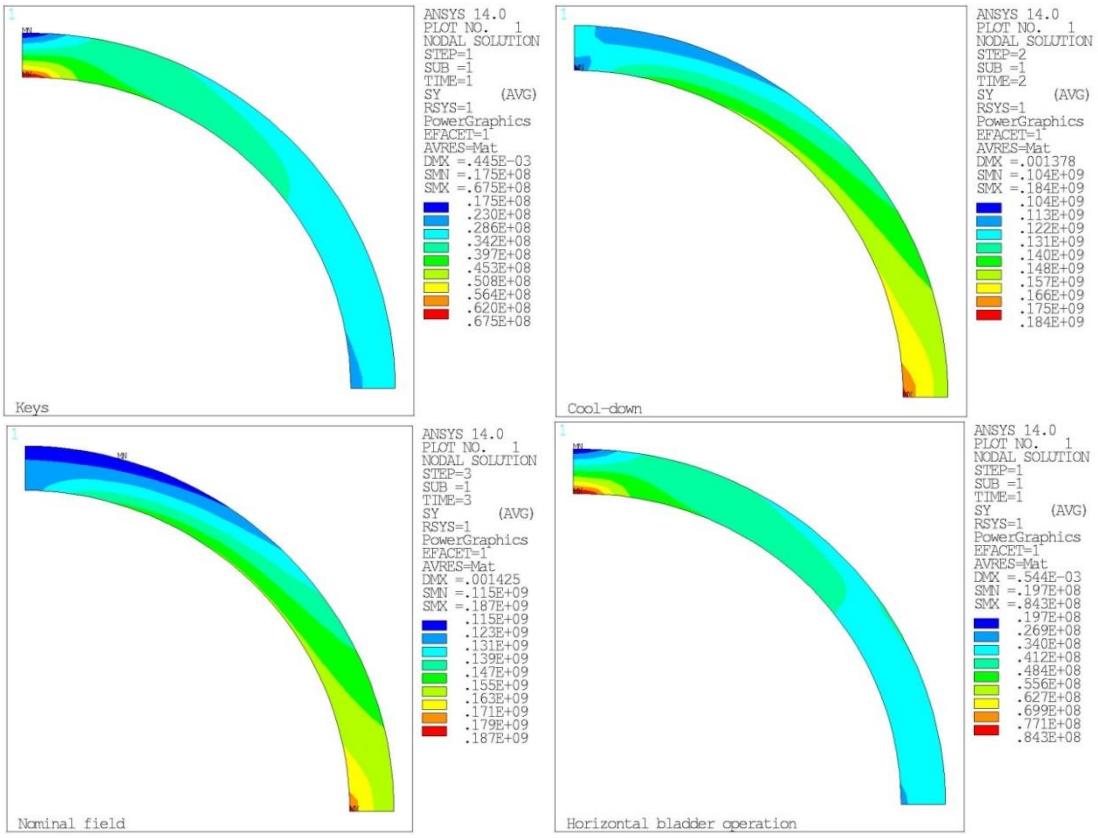

Fig. 5.1.9 – Computed shell azimuthal stress during bladder inflation (top left), after key insertion and bladder deflation (top right), after cool-down (bottom left), and at 13 T (bottom right).

The expected horizontal and Von Mises stresses developed in the coil during the four steps are shown in Figures 5.1.6-7. After cool-down, the maximum horizontal (Von Mises) stress in the coil is 134 (137) MPa. At 13 T a peak of 139 (129) MPa is observed, but the high stress and high field region do not overlap.

The model indicates also that in the nominal pre-load conditions, both the titanium alloy pole and the aluminum shell experience stresses within the plasticity limits (see Figures 5.1.8 and 5.1.9).

5.1.2 3D mechanical design

Magnet support structure design

FRESCA2 mechanical support structure is represented on Figure 5.1.10. It is consistent with the conclusions of the 3D magnetic design (§ 3) end the 2D mechanical design (§ 5.1.1). The coils are represented in red; the aluminum parts are represented in dark grey; the iron parts are represented in blue; the stainless steel parts are represented in light grey. The longitudinal support system consists in four Ø60 mm aluminum rods and two nitronic-50 steel end-plates delivering pre-load to the coils.

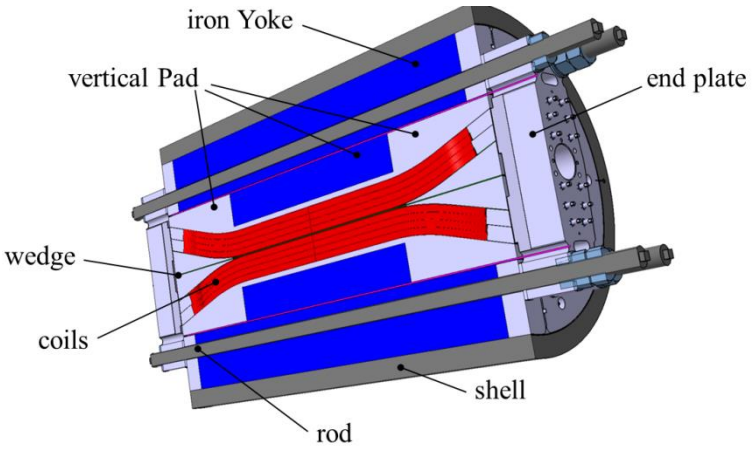

Fig. 5.1.10 – FRESCA2 mechanical support structure (longitudinal cut)

Figure 5.1.11 gives a focus on the coils, the clear bore and the iron parts.

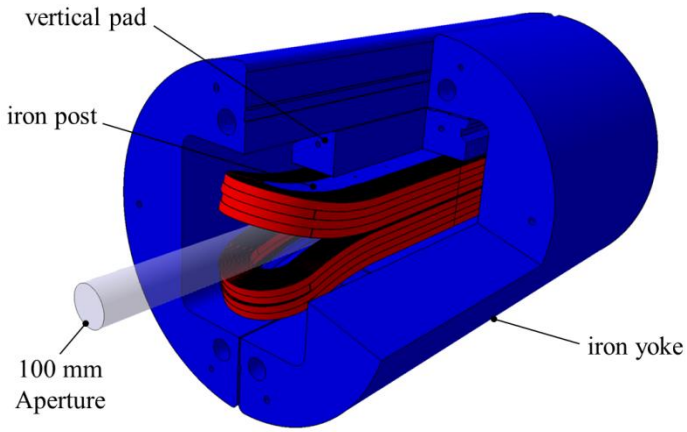

Fig. 5.1.11 – FRESCA2 mechanical support structure: coils and iron parts (cutaway view)

3D model: structure geometry

FRESCA2 3D FEM model is built in ANSYS. For symmetry reasons, only one octant is represented: half of the total length and quarter of the cross-section. The parts of the 3D model are shown in Figure 5.1.12. The coils model is represented on Figure 5.1.13. Friction coefficient of 0.2 is considered everywhere needed.

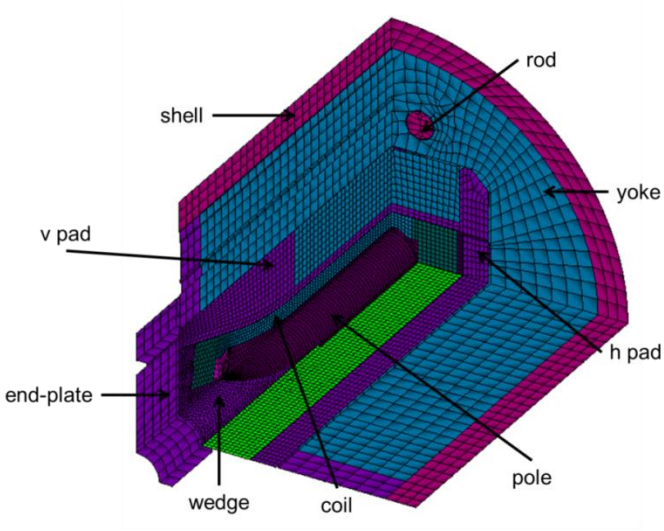

Fig. 5.1.12 – FRESCA2 3D model

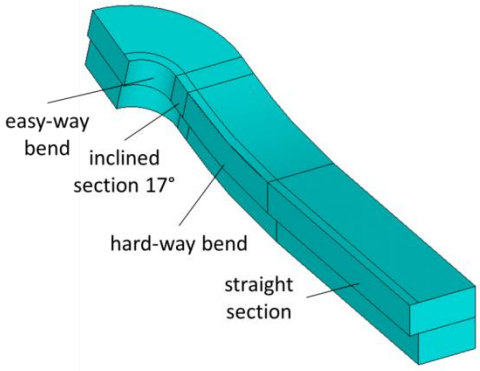

Fig. 5.1.13 – FRESCA2 3D coil model

The 3D model of the longitudinal compression system is shown in Figure 5.1.14. The sub-elements of the magnet are bonded together. A longitudinal pre-tension of 150 MPa is applied to the rods at room temperature using a hydraulic jack with a maximum capacity of 200 tons. The stresses in the aluminum rods and in the end-plates are within the yield stress limits.

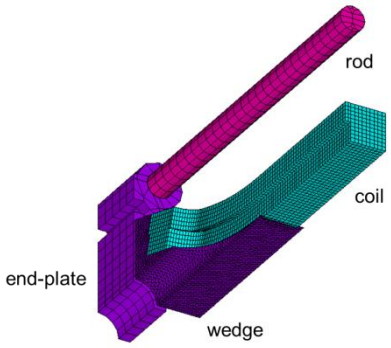

Fig. 5.1.14 – FRESCA2 3D longitudinal compression system

Cases of study

In the following, the 3D mechanical analysis will focus on three questions:

- **1) Impregnation**: is it better to impregnate the wedge with coil 1-2?
- **2) Lateral contact**: is it beneficial to force contact between the horizontal pad and the wedge (Figure 5.1.15 a)?
- **3) Longitudinal pre-load**: should the end-plate press on the coil pack and the wedge, or on the coil pack (via end-shoe), the wedge and the yoke (Figure 5.1.15 b)?

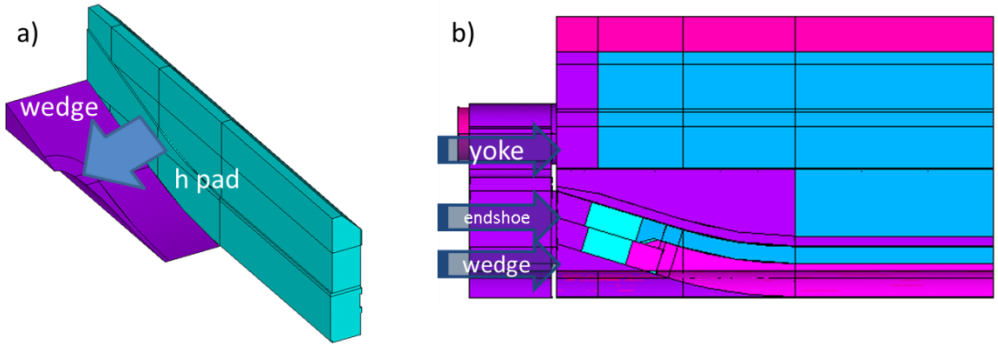

Fig. 5.1.15 – a) Lateral support: contact between the horizontal pad and the wedge
b) Longitudinal loading options

Case of study #1: impregnation of the wedge

The distribution of the Von Mises stresses in the coil is computed and compared at 13 T with/without wedge impregnation and with/without lateral contact between wedge and pads. The results are shown in Figures 5.1.16.

- The peak stress is higher when the wedge is impregnated with coils 1-2.
- When the wedge is *not* impregnated, the peak stress is higher *without* lateral contact.
- When the wedge *is* impregnated, the peak stress is higher *with* lateral contact.

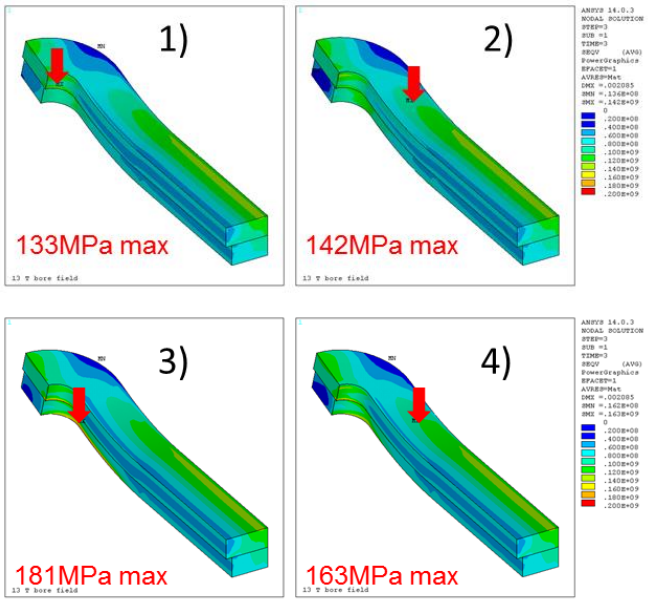

Fig. 5.1.16 – Von Mises stresses on the coils at 13 T (peak values are indicated).
Non-impregnated wedge: 1) with 2) without lateral wedge/pad contact.
Impregnated wedge: 3) with 4) without lateral wedge/pad contact.

The evolution of the coil peak stress along magnet lifecycle is shown in Figure 5.1.17 in the four cases. The best option in terms of peak stress corresponds to the **non-impregnated** wedge **with lateral contact** on the pads (case 1).

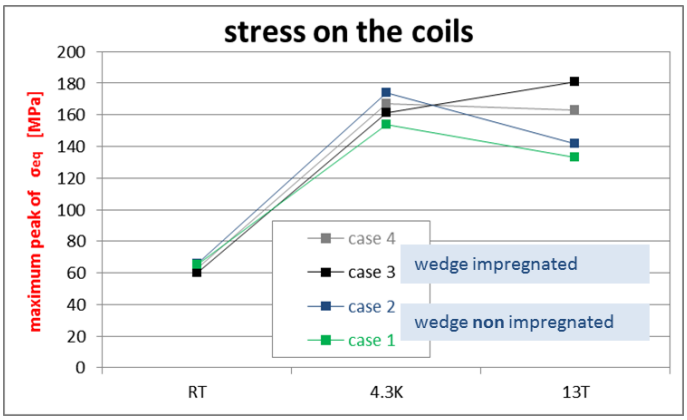

Fig. 5.1.17 – Evolution of the coil peak stress along magnet lifecycle

Case of study #2: lateral contact between wedge and pad

Figure 5.1.18 show the contact element located between the winding post and the coil in the hard-way-bend area of the coil (see Figure 5.1.13), in both wedge impregnation configurations. In any case, post and coils are impregnated together. The areas in color indicate *compression*, whereas the grey areas indicate *tension* (< 30 MPa).

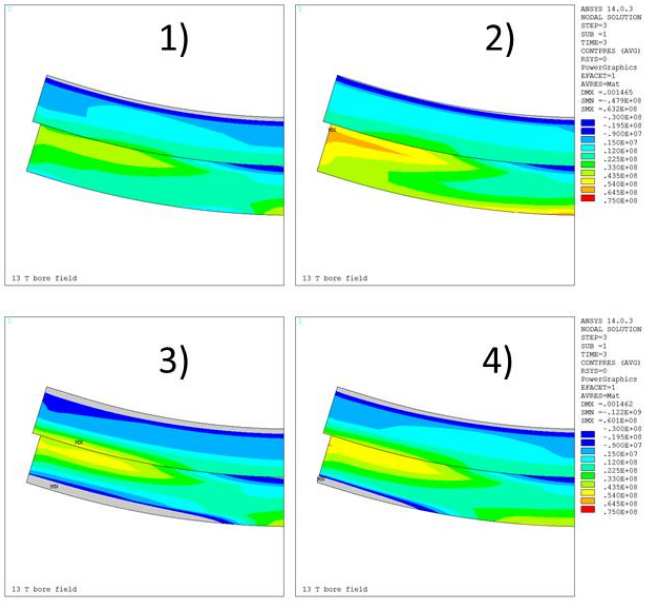

Fig. 5.1.18 – Compression stresses on the coil/post contact at 13 T (hard-way bend area).
Non-impregnated wedge: 1) with 2) without lateral wedge/pad contact.
Impregnated wedge: 3) with 4) without lateral wedge/pad contact.

The tension area is larger when the wedge is impregnated. Hence, the **non-impregnated** case is a better option in order to avoid the risk of delamination and cracking of the epoxy resin. The influence of the lateral contact remains little. Figure 5.1.19 compares the peak *tension* stresses at 13 T in the four cases. This is consistent with the conclusions of the case of study #1.

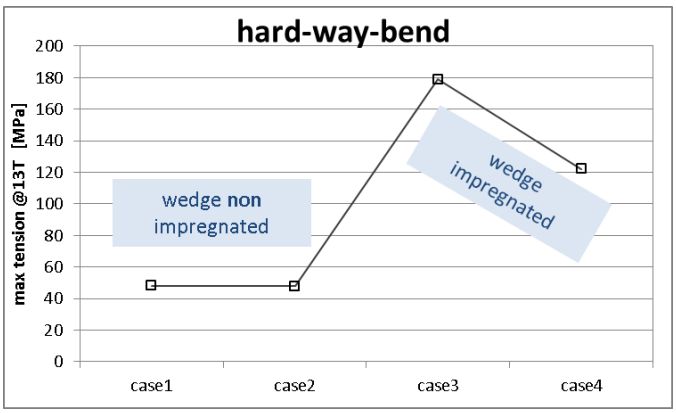

Fig. 5.1.19 – Peak tension stress at 13 T

Case of study #3: longitudinal loading

Assuming a non-impregnated wedge, two configurations are compared for longitudinal loading (see Figure 5.1.15 b):

- Pushing with the end-plate on the end-shoe + wedge
- Pushing with the end-plate on the end-shoe + wedge + yoke

The results in terms of contact pressure in the coil ends are given in Figure 5.1.20 at room temperature (just after longitudinal loading) and after cool-down together with the corresponding longitudinal forces.

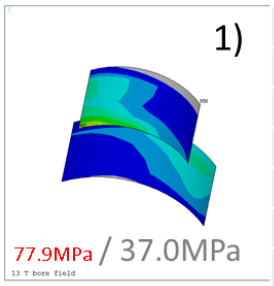

	forces [kN]	
	293K	4.3K
endshoe1	-106	-176
endshoe2	-326	-529
wedge	-5	-41
total	*-437*	*-746*
rod	437	740

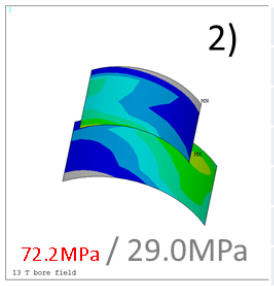

	forces [kN]	
	293K	4.3K
endshoe1	-109	-196
endshoe2	-320	-516
wedge	-7	-27
total	*-436*	*-739*
rod	437	740

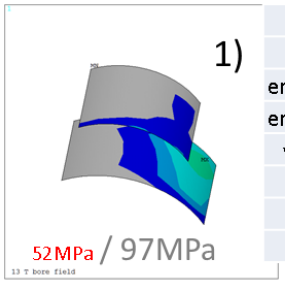

	forces [kN]	
	293K	4.3K
endshoe1	-31	0
endshoe2	-52	0
wedge	-16	0
yoke	-328	-882
total	*-427*	*-882*
rod	427	880

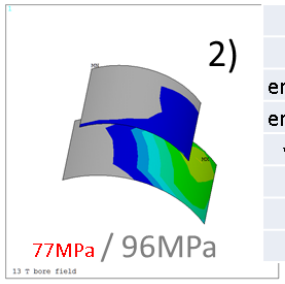

	forces [kN]	
	293K	4.3K
endshoe1	-40	0
endshoe2	-52	0
wedge	-10	0
yoke	-323	-878
total	*-425*	*-878*
rod	426	878

Fig. 5.1.20 – Compression stresses on the coil/post contact (ends), with non-impregnated wedge. Pre-load on the end-shoe + wedge (top) or on the end-shoe + wedge + yoke (bottom) 1) with 2) without lateral wedge/pad contact.

When pushing only on the end-shoe + wedge, most of the force goes to the end-shoe. The tension is slightly lower without lateral wedge/pad contact. When pushing *also* on the yoke, most of the force goes to the yoke at 293 K, even if a low-pressure contact is maintained between the end-plate and the end-shoe + wedge. This contact is lost at 4.2 K. Hence, it seems better to push on the end-shoe + wedge only. The influence of the lateral contact is negligible in that case.

5.2 Thermal study

5.2.1 Numerical modeling

The goal of this study is to calculate the maximum temperature difference in the magnet structure during steady and transient state conditions and to predict the thermal behavior due to a quench of the magnet. The thermal modeling was performed at 1.9 K (superfluid helium condition) and 4.2 K (saturated helium). To simulate the thermal-flow behaviors in superfluid helium a simplified 2D two-fluid model was extended to the 3D geometry of the magnet and developed in ANSYS CFX software. This model is derived from the original two-fluid model and consists of a conventional continuity equation, a modified momentum equation for the total fluid and an energy equation including the Gorter-Mellink internal convection term modeling the turbulence regime. More details can be found in [5.2].

The result of temperature distribution in He II and in the solid elements at the bath temperature of 1.9 K is shown in Figure 5.2.1 a. The details of temperature field in the central part in presented in figure 5.2.1 b. With a power of 0.2 W, due to AC losses distributed in the conductors [5.3], the warmest part of the magnet is at the central part of the coil with the maximum value of the temperature localized in the layer 4 (represented by a dot in the picture). The corresponding temperature increase is T-T_b = 193 mK which is much lower than the temperature margin (5.8 K).

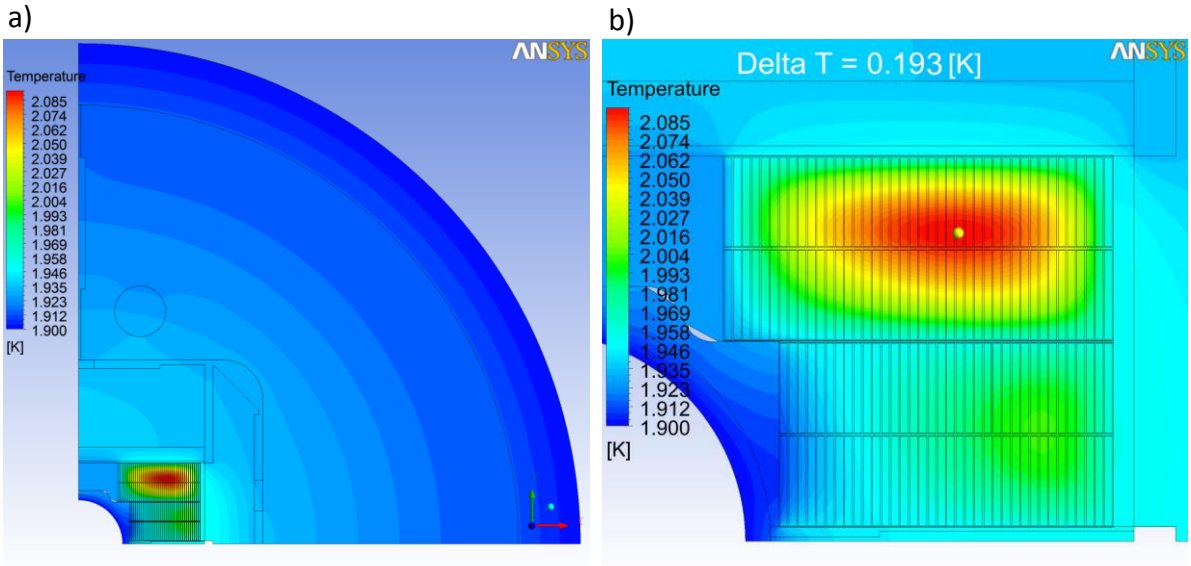

Fig. 5.2.1 – a) Temperature field for the bath temperature of 1.9 K
b) Details of the temperature distribution in the coils at 1.9 K.

The results presented in Figure 5.2.1 have been compared with a so-called ”full conduction” model of FRESCA2 magnet described in [5.4], with no helium between laminations. This is a conservative case. Results are presented in Figure 5.2.2 for the AC losses power distribution. Adding He II to the structure of the magnet makes the temperature rise only 17% lower because there is no helium in the coil since the magnet is fully impregnated with epoxy. Different calculations have been performed with the “full conduction model” and the results are summarized in Table 5.2.a. According to our calculations, the magnet will be kept safe even for a heat load of 10 W dissipated in the whole coil (5.292 W per meter of conductor). This value of the heat load will generate a temperature rise of 4.0 K at a bath temperature of 1.9 K and temperature rise of 2.1 K at bath temperature of 4.2 K.

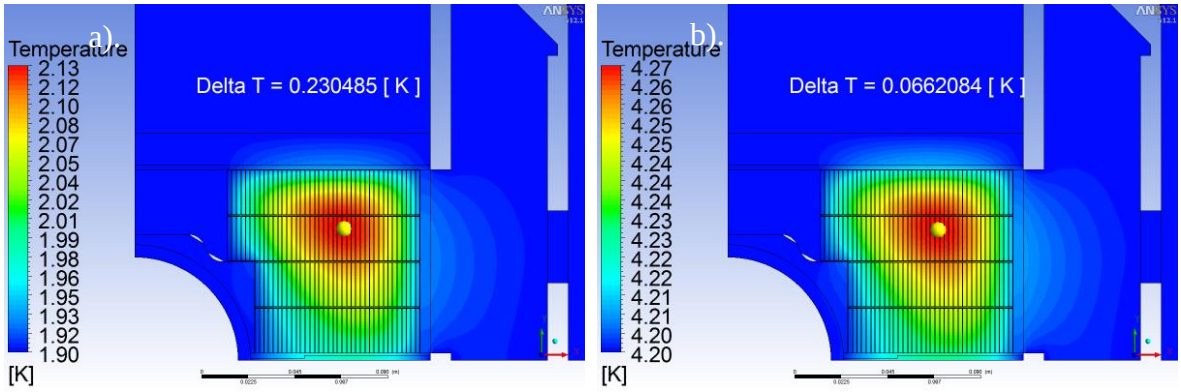

Fig. 5.2.2 – Temperature field with the localization of maximum temperature given by the conductive model for the AC losses power distribution at 1.9 K a) and b) 4.2 K

In the following table, the heat load is presented in W, W/m of conductor length and W/m^3 of conductor volume.

Table 5.2.a – VALUES OF MAXIMUM TEMPERATURE RISE AT 1.9 AND 4.2 K FOR ALL VARIANTS OF SIMULATIONS

		Unit	Maximum tempearture rise				Margin of temperature (K) (at B = 13.5 T and I = 10.5 kA)
			AC losses model	Homogenous model			
Heat load	Total	W	0.50	1	5	10	
	By length of conductor	W/m	0.11	0.53	2.64	5.29	
	By volume of conductor	W/m^3	4.34	21.78	108.88	217.75	
Bath temperature	@ 1.9	K	0.23	1.05	2.91	3.95	**5.84**
	@ 4.2	K	0.07	0.35	1.34	2.20	**3.54**

It is important to understand the thermal behavior of the magnet during cool-down. The temperature differences created within the magnet structure can cause internal thermal stress and in extreme cases, for high values, cracks and eventually magnet failure. The knowledge about the evolution of temperature within the magnet can be useful for optimizing the cool-down process, reducing the working hours and in consequence reducing the amount of coolant.

In [1.1], it has been proposed that the cool-down process could be done following two successive cooling steps. The first cooling step is *indirect*: the magnet is cooled from 300 K to 20 K via eight external cooling tubes placed on the aluminum shell. When the temperature of the magnet reaches 20 K, the cool-down continues by *direct* cooling: helium is supplied around the internal and external magnet structures.

In the models, four possible durations of indirect cool-down are compared: 1.5, 2, 3 and 4 days. All scenarios with particular steps are summarized in table 5.2.b.

Table 5.2.b – COOL-DOWN SCENARIO FOR INDIRECT COOLING					
Step		Time			
		I	II	III	IV
1	Cooling step from 300 K to 80 K	0.5 day	1 day	2 days	3 days
2	Electrical integrity test at 80 K	6 hours	6 hours	6 hours	6 hours
3	Cooling step from 80 K to 20 K	12 hours	12 hours	12 hours	12 hours
4	Electrical integrity test at 20 K	6 hours	6 hours	6 hours	6 hours
Total		**1.5 days**	**2 days**	**3 days**	**4 days**

The evolution of the cooling temperature (called "cooling function") is linear along cool-down and constant during electrical integrity test, with respect to the time. For all scenarios, the maximum of temperature difference appears in the first step from 300 K to 80 K (Figure 5.2.3). A maximum difference of 60 K is obtained for the faster scenario (1.5 days), to be compared to 10 K for 4 days of indirect cooling. From the experience gained during the design of the LHC main magnet at CERN, the maximum acceptable temperature difference during cool-down is estimated around 30 K. To satisfy that condition, **FRESCA2 must be cooled-down in more than 2 days**.

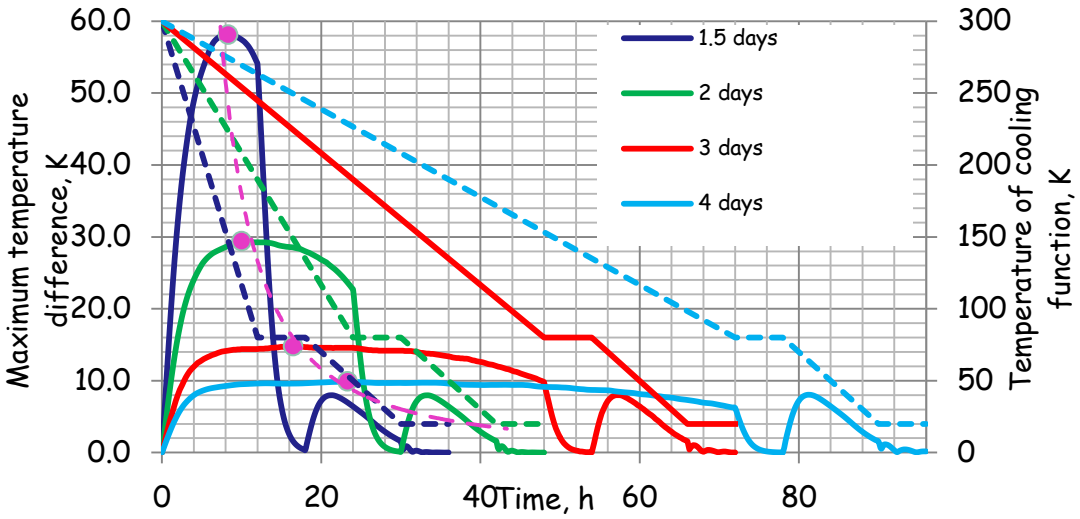

Fig. 5.2.3 – Evolution of the maximum temperature difference (solid lines) as a function of the cooling function, for four cool-down scenarios.

After indirect cool-down to 20 K via external tubes, direct cooling method from 20 K to 4.2 K is applied: the helium is transferred from the bottom to the top of the magnet. Data for the indirect cooling are taken as initial conditions.

In comparison to the indirect cool-down method, direct cooling generates very small temperature differences in the magnet structure. The maximum difference (0.47 K) is reached after half an hour. The evolution of the maximum temperature difference created in the magnet during direct cooling is presented in Figure 5.2.4.

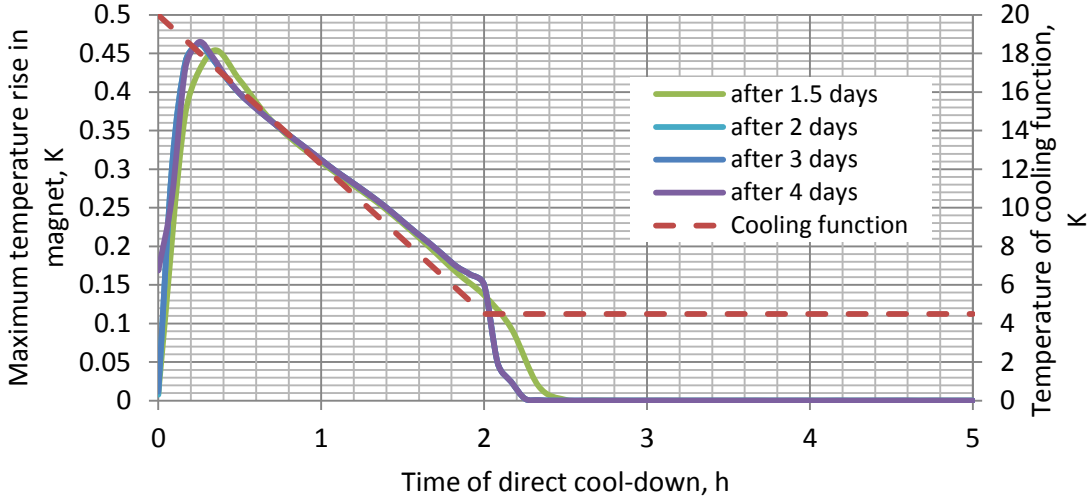

Fig. 5.2.4 – Evolution of the maximum temperature difference in the magnet, and cooling function as a function of time.

FRESCA2 magnet will be operated at CERN in vertical position. In order to design the cryogenic infrastructure for cryostat operation, it is necessary to know the required power for the cryogenic system. According to the numerical calculations, if the magnet is cooled-down using the indirect method within 1.5 days, the maximum power of the cryogenic system shall be higher than 17 kW; for a shorter time, the required power is lower and for 2 days, it is estimated to be 9 kW, for 3 days – 5 kW and for 4 days 3.5 kW. The calculations of the heat which has to be removed from magnet structure during cooling process are shown in Figure 5.2.5.

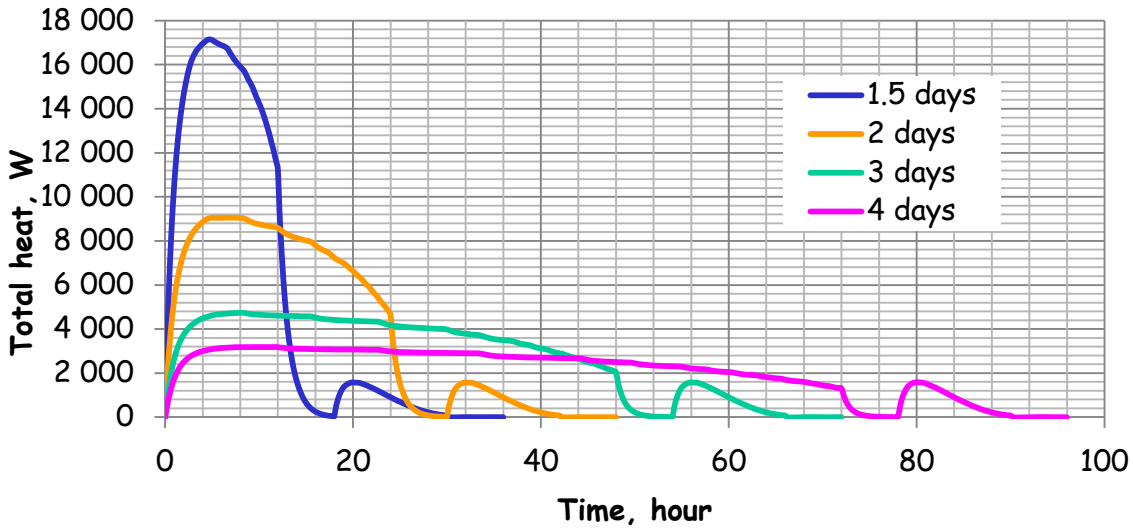

Fig. 5.2.5 – Evolution of the total heat removal during magnet cool-down.

5.2.2 Material for the electrical insulation

Cyanate ester epoxy mix and tri-functional epoxy (TGPAP-DETDA) with S-glass fiber are possible candidates for the electrical insulation. They have been thermally tested in this project. Since FRESCA2 is expected to be operated in pressurized superfluid helium at 1.9 K and atmospheric pressure, the thermal conductivity and the Kapitza resistance are the most important parameters for the thermal design of this type of magnet. To obtain the thermal conductivity and Kapitza resistance, the "drum" technique is used [5.5]. The results of the thermal conductivity as a function of the temperature are shown in Figure 5.2.6. The thermal conductivity of both materials is given by the following linear expressions:

$$k = [(34.2\pm5.5) \times T-(16.4\pm8.2)].\ 10^{-3}\ Wm^{-1}K^{-1}, \quad (1)$$

for the TGPAP-DETDA sample and

$$k = [(26.8\pm4.8) \times T-(9.6\pm5.2)].10^{-3}\ Wm^{-1}K^{-1} \quad (2)$$

for cyanate ester epoxy mix sample.

The thermal conductivity of the tested materials is compared in Figure 5.2.6 with other insulations such as epoxy, epoxy resin fiberglass tape and Kapton. The TGPAP-DETDA epoxy insulation has the largest thermal conductivity, six times larger than the one of Kapton.

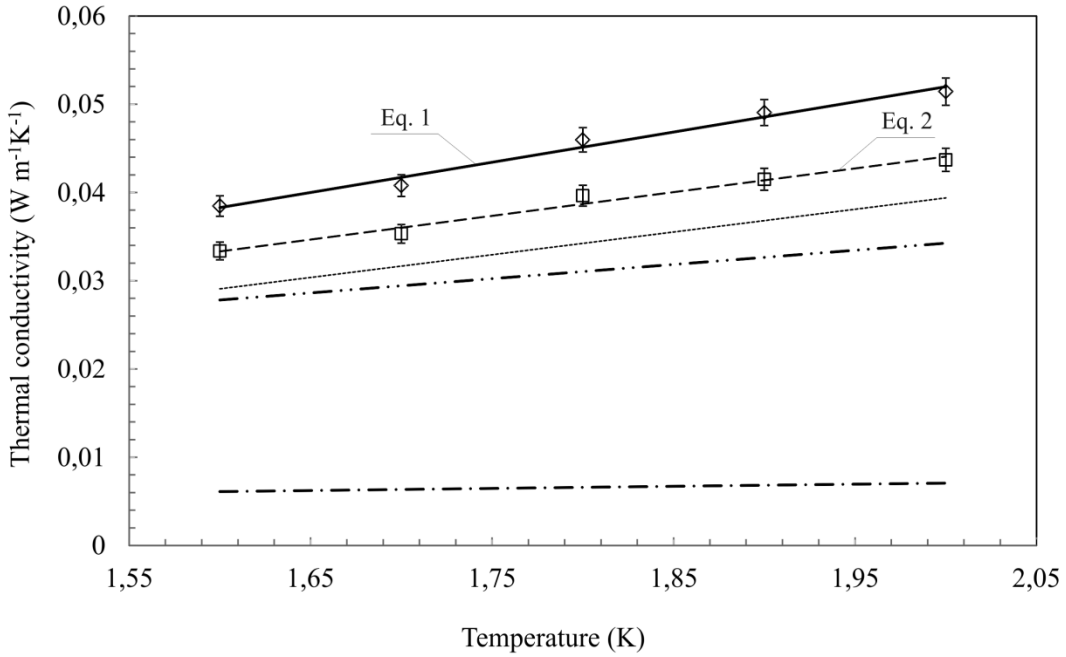

Fig. 5.2.6 – Evolution of the thermal conductivity with temperature: TGPAP-DETDA ◇, cyanate ester mix □ [5.6], Kapton [5.7] –·–·–, epoxy resin fiberglass tape [5.8] ··· and epoxy [5.9] –··–··–

Figure 5.2.7 presents the data obtained during measurements and the best fit for the Kapitza resistance. The data can be expressed by the following expressions for the TGPAP-DETDA epoxy:

$$R_k = (3057\pm593).10^{-6}\times T^{(-1.79\pm0.34)}\ m^2KW^{-1}, \quad (3)$$

and for the cyanate ester epoxy mix:

$$R_k = (4114\pm971).10^{-6}\times T^{(-1.73\pm0.41)}\ m^2KW^{-1}. \quad (4)$$

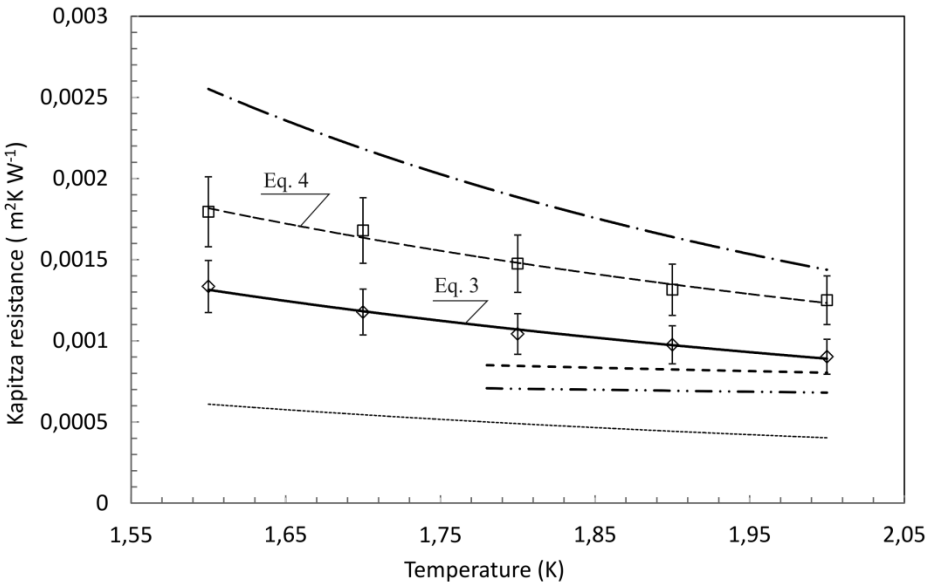

Fig. 5.2.7 – Evolution of the Kapitza resistance with temperature: TGPAP-DETDA ◇, cyanate ester mix □ [5.6], Kapton [5.7] –·–·–, epoxy resin fiberglass tape [5.8] ---, Stycast coating on polished surface [5.10] –··–··–, Stycast coating on oxidized surface [5.11] - - -

In this plot, the experimental results of Kapitza resistance are compared with different materials such as: Kapton, epoxy resin fiberglass tape and Stycast coated on polished and oxidized surfaces. The obtained results are in the same order of magnitude than the insulations found in the literature. Our result is almost two times larger than the one obtained for epoxy resin fiberglass tape even though the external surfaces of the insulations are totally covered by the resin. We can assume that the Kapitza resistance is directly related to the epoxy resin only.

5.3 Interface with the insert

An HTS insert is built in the framework of EuCard HFM task 7.4 [5.12]. It aims at producing an additional field of around 6 T inside of the FRESCA2 dipole that will provide a background field of 13 T.

Some geometrical constrains have to be respected during FRESCA2 design:

- The insert cannot transfer any load on the FRESCA2 magnet. Its external radius has been fixed to 99 mm to avoid any interference with the dipole structure. FRESCA2 structure must let a clear bore of 100 mm for the insert, at any operation step.
- The insert must be fully dismountable from the Nb_3Sn magnet, without disassembly.

On the magnetic point of view, all magnetic calculations have been done in 2D and 3D with the two magnets. The magnetic flux due to the insert in FRESCA2 is opposite to its own flux: the insert contributes to reduce the peak field of FRESCA2.

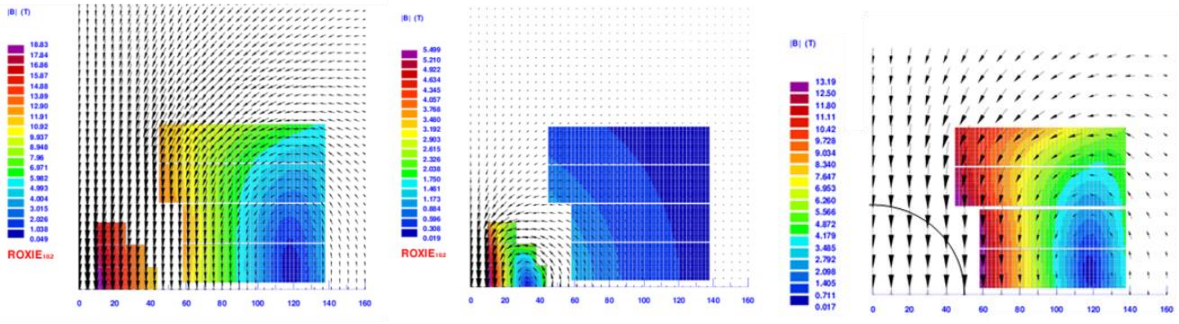

Fig. 5.3.1 – Field map in the dipole and the insert in three cases: both magnets are energized (left), only the insert is energized (mid), only the dipole is energized (right)

On the mechanical level, the insert must be self-supported at 19 T:

- all calculations for the insert have been done with this assumption;
- the influence of the forces created by the insert on FRESCA2 has been evaluated in 2D:

Table 5.3.a – MECHANICAL INFLUENCE OF THE INSERT ON FRESCA2

Forces on FRESCA2 per quadrant	Alone (under 13 T)	With the insert (under 19T)
$F_{X_{(FRESCA2)}}$ [MN/m]	7.6	7.3
$F_{Y_{(FRESCA2)}}$ [MN/m]	-4.0	-4.3

A significant augmentation on F_Y is observed. However, this force value is lower than the one occurring at 1.8 K, 15 T.

- The case when the insert is not centered has been evaluated with a decentering of the insert in the X or Y direction, up to 1 mm. This upper bound is pessimistic: the maximal displacement allowed for the insert in the bore tube is 0.5 mm. The largest additional forces occur with a misalignment in the Y direction. The resultant forces whit a shift of 1 mm are: F_Y = 7.1 kN on

FRESCA2 and F_Y = -2.6 kN on the insert (the force resultant on the whole {insert + dipole} system is not equal to zero because the forces have been calculated on the conductor only and not on the magnetic iron parts). These values are very weak compared to the forces on the magnets.

The protection of FRESCA2 alone is detailed in the previous § 4.5. The common protection of the assembled magnets powered together has been studied in different cases:

- Quench of the insert inside of FRESCA2: the fast discharge of FRESCA2 is preconized together with the discharge of the insert. The simulation with only the discharge of the insert shows that there is peak reverse voltage across the power supply of about -35 V and a peak of the current in FRESCA2 of 380 A above the nominal value of 10,900 A, which can provoke a quench.
- FRESCA2 quench with insert inside: the best solution seems to discharge the insert and FRESCA2 immediately when a quench inside FRESCA2 is detected. In the other case, without discharging the insert, some extra current of 480 A is induced in it, which induces a quench in the insert and so a discharge. A reverse voltage in the power supply reaches about -140V, which can damage it [5.13,5.14].

A Kapton layer will be put on the tube to protect the magnets one from the other in case of arc.

The test procedure, which is under preparation, will follow the following points:

- The two magnets must be tested separately before being assembled.
- The two magnets will operate at the same temperature and will cool down at the same time, by the same way. The thermal inertia of FRESCA2 will be used to cool down the insert.
- The minimal temperature during the tests should not be under T_λ. In the other case, it will be difficult to detect a quench in the insert.

5.4 Design summary

The conceptual design described above leads to the magnet parameters listed in Table 5.4.a.

Table 5.4.a – EuCARD-HFM DIPOLE PARAMETERS

Parameter name		Symbol	Unit	Value	Source	Remarks
2D DIPOLE FEATURES						
Number of layers		N_L	/	4	MPWG #7	Per pole
Nominal insulated cable width		$w_{clb,ins}$	mm	21.8	MDWG #24	Reacted
Nominal insulated cable thickness		$t_{cbl,ins}$	mm	2.22	MDWG #24	Reacted
Turns number	Layer 1	N_1	/	36	MPWG #12	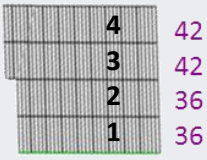
	Layer 2	N_2	/	36	MPWG #12	
	Layer 3	N_3	/	42	MPWG #12	
	Layer 4	N_4	/	42	MPWG #12	
Overall turns number		N_{tot}	/	156	Calculated	$= N_1+N_2+N_3+N_4$
Inner coil radius	Layer 1	r_1	mm	58	MPWG #13.2	
Last turn horizontal position		x_i	mm	137.92	Calculated	$= r_1 + N_1.t_{cbl,ins}$; i = {1..4}
Midplane insulation thickness		t_{mid}	mm	7	MPWG #14.2/Devaux	*i.e.* 3.5 mm per side
Interlayer insulation		t_{1-2}, t_{3-4}	mm	0.5	MPWG #14.2	Layers 1-2 and 3-4
Inter-coil insulation		t_{2-3}	mm	1.5	MDWG #10.3	Layers 2-3
3D DIPOLE FEATURES						
Magnet length		L	mm	1500	EuCARD	Coil end-to-end
Ramp angle		α	°	17	MPWG #14.2	
Hard-way bend radius		R_{HW}	mm	700.3	MPWG #14.2/MDWG #24	Layer 4, minimal value
Inclined straight section length		$L_{OS,1-2}$	mm	24	MPWG #14.2	
		$L_{OS,3-4}$	mm	32	MDWG #2.2	
Straight section length		$L_{SS,1-2}$	mm	730	Calculated	Straight section + jump
		$L_{SS,3-4}$	mm	728	MDWG #2.2	Straight section + jump
Baseline magnet width		w	mm	276	Calculated	
Baseline magnet height		h	mm	170	Calculated	
Magnet stay-clear half-height		h_1	mm	61.7	Calculated	
Layer jump type		/	/	HW 2 chicanes	MDWG #10.2	
Total cable length		L_{SC}	m	952	Calculated	For the full dipole
Magnet volume		V_{SC}	m^3	0,046	Calculated	For the full dipole
MAIN STRUCTURE FEATURES						
Central post aperture radius		r_{bore}	mm	50	MPWG #13	
Iron yoke radius		r_{yoke}	mm	450	MDWG #2.3	
Aluminum shell thickness		t_{shell}	mm	65	MDWG #2.3	
Rod diameter		ϕ_{rod}	mm	60	MDWG #14	

Figure 5.4.1 gives an overview of the final dipole configuration. There is one color per piece of cable.

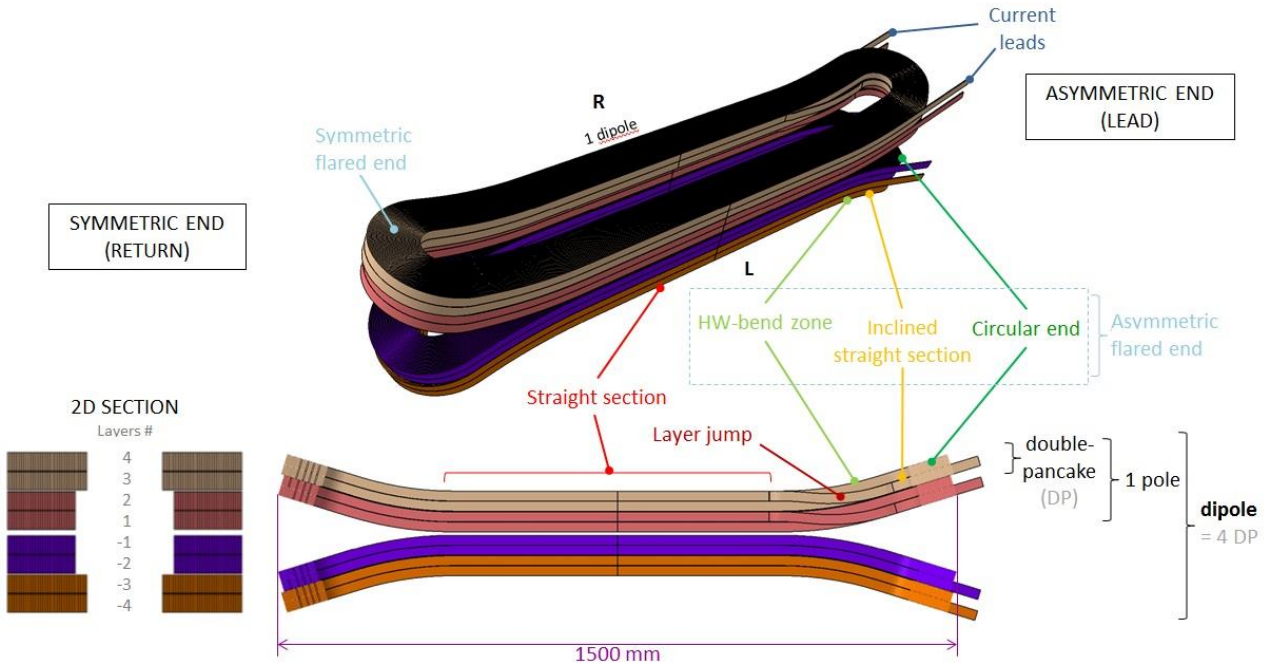

Fig. 5.4.1 – FRESCA2 dipole: final configuration.

Figure 5.4.2 gives close-up on the magnet structure 2D section, showing the position of insulation layers and instrumentation traces around the coil. Coils 1-2 and 3-4 will be impregnated separately, as illustrated by the red rectangles.

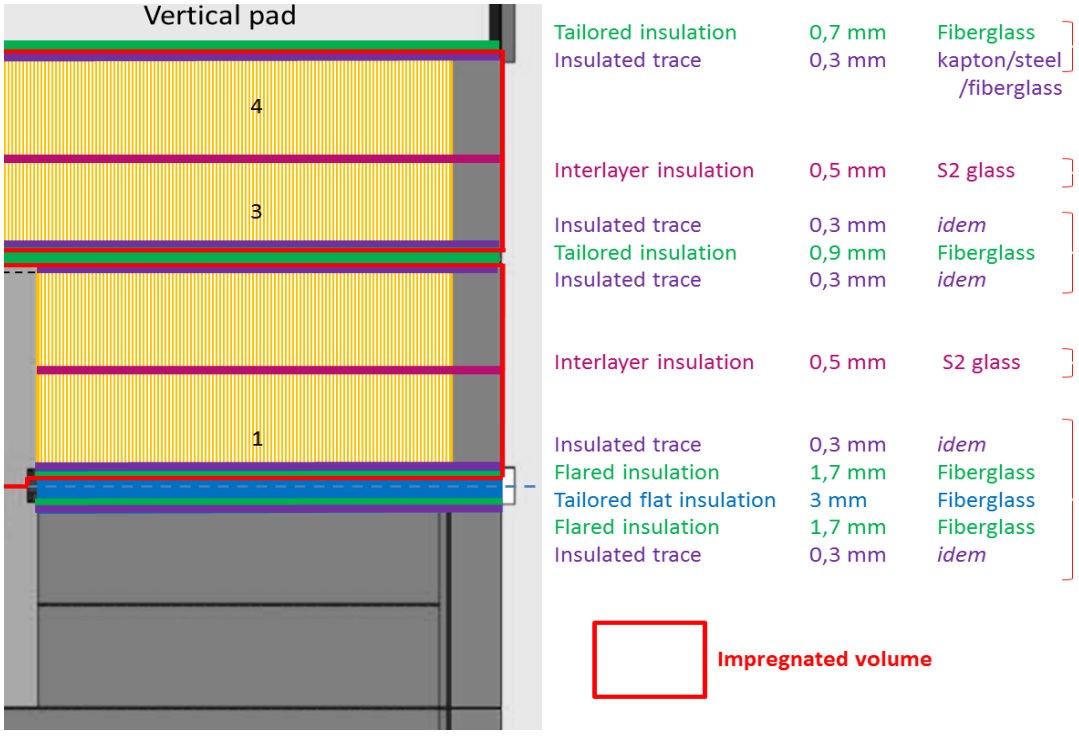

Fig. 5.4.2 – FRESCA2 dipole: final 2D insulation configuration.

6. Manufacturing and assembly steps

As mentioned before, Nb_3Sn technology is very sensitive to details because of the conductor fragility. Apart from the conceptual design, great care must be taken to achieve the detailed engineering design and to define the manufacturing procedure and the related tooling.

The mains steps of the coils manufacturing and assembly steps are:

- Conductor insulation (§ 3.3)
- Conductor preparation (§ 6.1)
- Coil winding (§ 6.1)
- Coil reaction (§ 6.2)
    - Preparation for the heat treatment
    - Assembly of the reaction mould around the wounded coil
    - Transport to the reaction site (CERN)
    - Heat treatment
- Coil impregnation (§ 6.3)
    - Nb_3Sn/Nb-Ti splice soldering
    - Instrumentation, ground insulation and quench heaters integration
    - Impregnation
- Coil assembly (§ 6.4)
- Magnet assembly (§ 6.4)

6.1 Coil winding

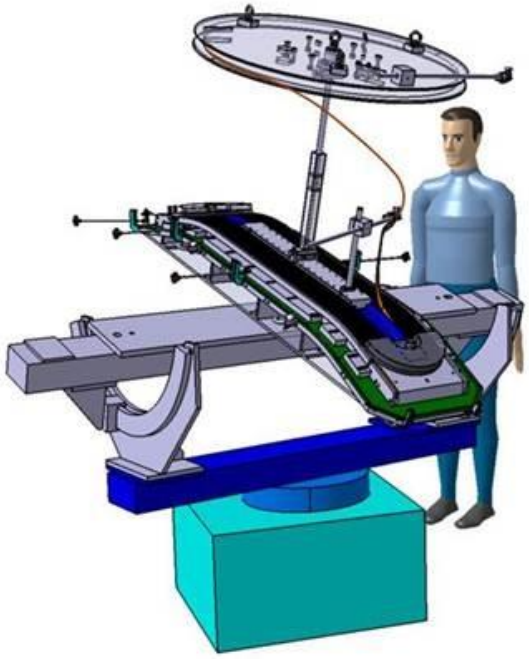

Fig. 6.1.1 – Winding machine.

Each coil is formed of two layers of conductor wounded from one unit length in race-track geometry with flared ends (see chapter 5).

All the surface of the components of the coil in direct contact with the conductor (central post, layer jump shim, rails and shores-shoes receive and additional insulation layer of alumina via plasma deposition.

Following the winding tests results (§ 7.7), the coil winding is performed with flared ends upside-down.

6.1.1 Winding preparation

The winding is done using a winding machine, which allows tilting the winding table to follow the geometry of the coil, and a tensioner to maintain the conductor under a tension of 30 daN.

During the preparation steps, the insulated conductor unit length is split on two different mandrels, one for each coil layer.

The winding table is fixed on the winding machine and is equipped with mica protection layer of 0.2 mm (in green in Figure 6.1.2).

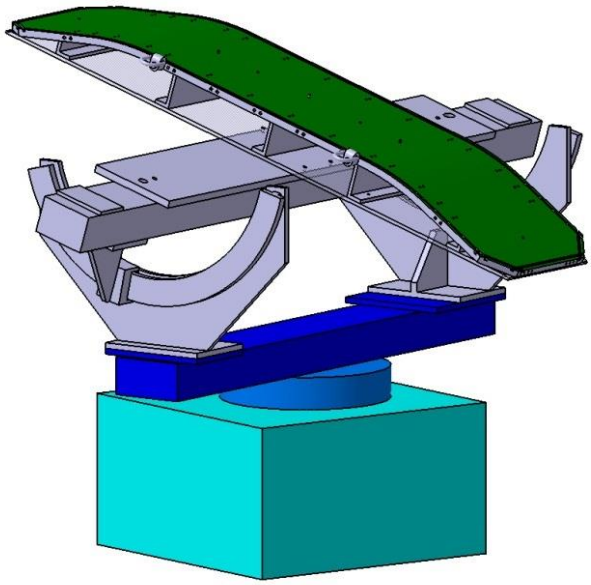

Fig. 6.1.2 –Winding table for coil 3-4, installed on the winding machine.

The central post is then fixed on the winding table. An additional mica sheet of 0.3 mm is installed around the central post to reserve during the winding the space required for the instrumentation layer.

The central post is then equipped with the spool support, which will received the stock spool with the second layer (layer 3 for the coils type 3-4 or layer 1 for the coils type 1-2) (Figure 6.1.3). The spool with the first layer to be wounded (layer 4 for the coils type 3-4 or layer 2 for the coils type 1-2) is installed on the tensioner.

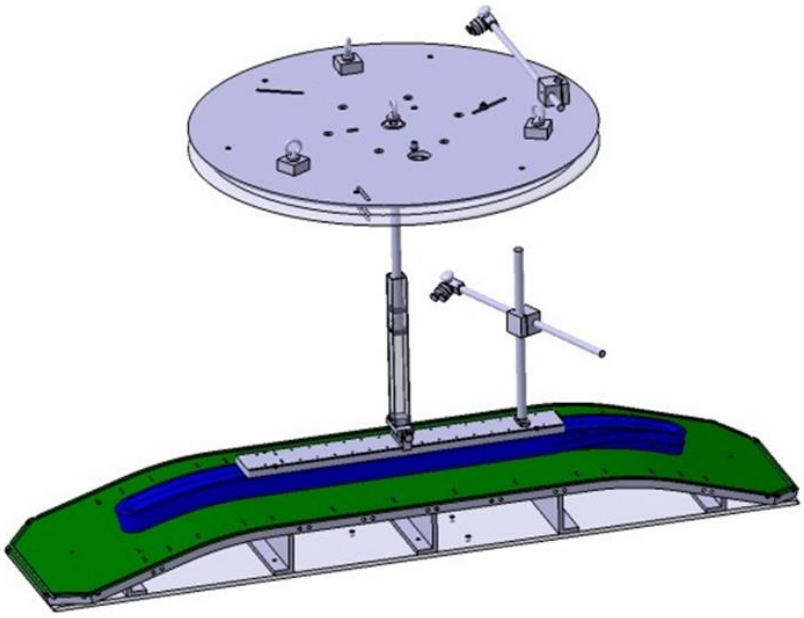

Fig. 6.1.3 – Winding table with the central post (in blue and the stock spool for the second layer (in grey).

6.1.2 Winding steps

The winding starts by forming the layer jump (*cf*. § 4.4.2) and by positioning it in a groove machined in the central post (Figure 6.1.4). In the layer jump region, the insulation of the cable is reinforced with a glass fiber tape of 0.2 mm thickness, wrapped without recovery. The layer jump is protected with the layer jump shim.

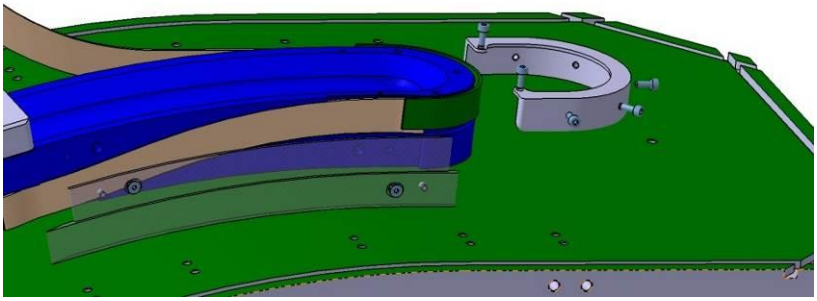

Fig. 6.1.4 – Layer jump.

During winding, conductor turns will be guided and maintained in the right position by lateral compression system using pressure wedges and rods.

The voltage taps are inserted below the insulation braid along the cable (Figure 6.1.5*Fig. 6.1.*), according to the instrumentation design (*cf*. § 4.6).

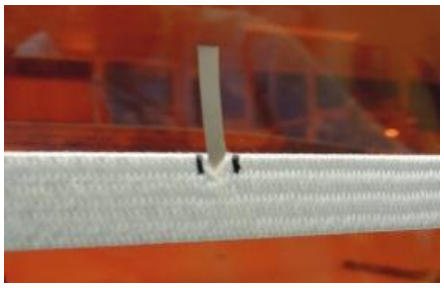

Fig. 6.1.5 – Voltage tap inserted below the insulation braid.

At the end of the layer 4 (respectively layer 2) winding, the bottom layer is maintained through rails and pressure wedges (Figure 6.1.6). The positions of the rails are imposed by the dimension of the reaction cavity defined for the coil.

The cable is then fixed and cut.

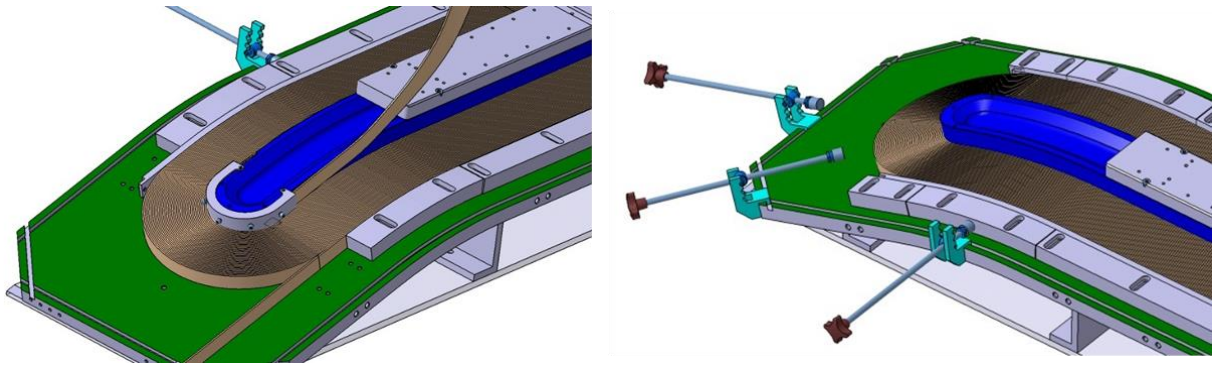

Fig. 6.1.6 – Lower layer 4 winding is completed.

The interlayer insulating sheet (*cf*. Figure 5.4.2) is placed over the lower layer and the upper layer is wound over the insulating sheet in the same way as for the first layer.

At the end of the layer 3 (respectively layer 1) winding, the layer is maintained through rails and pressure wedges. After the check of the coil heads dimensions, the end-shoe end spacers are adapted if necessary and pushed in place (Figure 6.1.7).

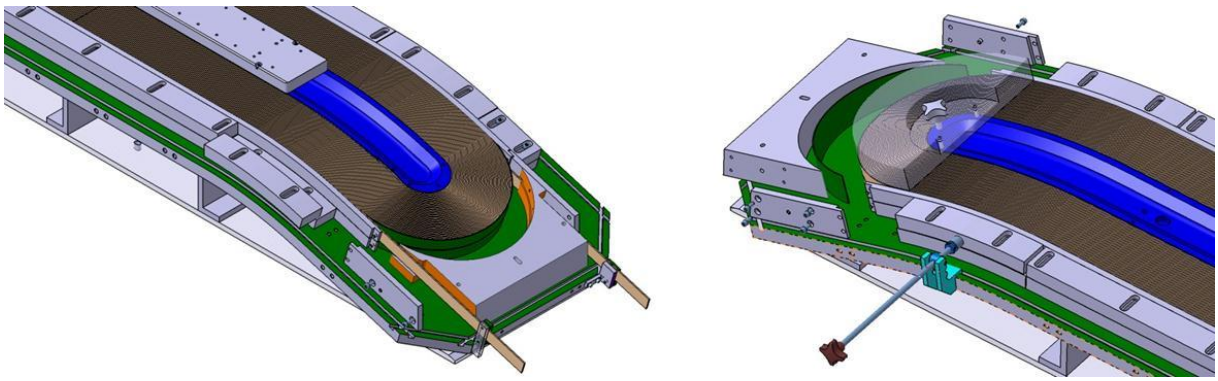

Fig. 6.1.7 – Positioning of the end-shoes.

The rails are then fixed to the end-shoes in order to close the coil (Figure 6.1.8).

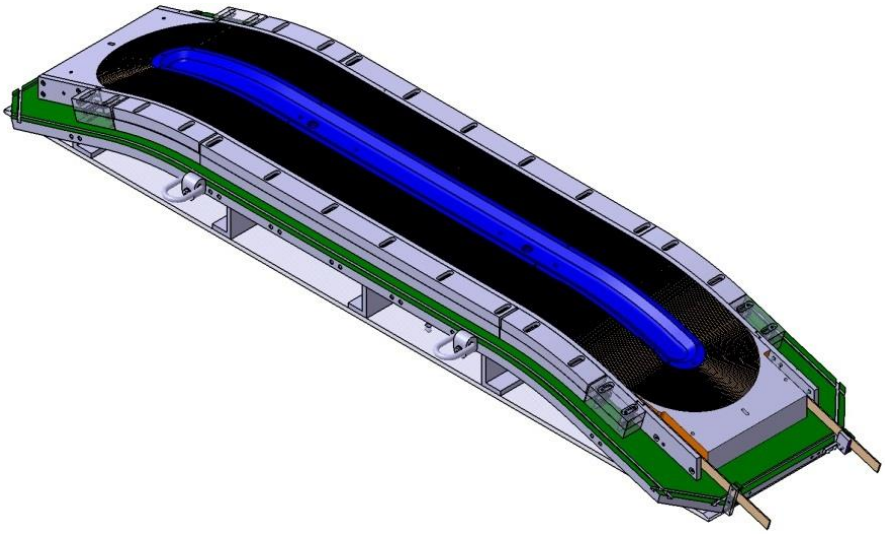

Fig. 6.1.1 – Coil winding completed.

6.2 Coil reaction

6.2.1 Closing the reaction tooling

To limit at the maximum the manipulation of the coil during the manufacturing process, the reaction tooling has been design in such a way that the winding table is a part of the reaction tooling (see Figure 6.2.1).

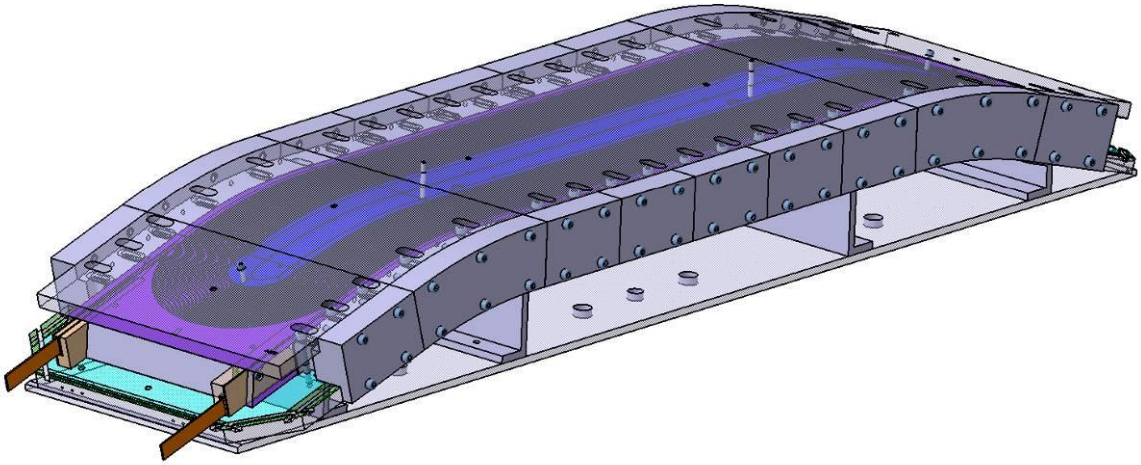

Fig. 6.2.1 – Coil inside of the reaction mold.

The reaction mold is closed by adding top plates and lateral compression wedges around the coil. The segmentation of those components allows to replace the compression wedges without modifying the lateral dimension and pressure on the coil.

The reaction cavity dimensions have been defined by adding 4% with respect on bare cable thickness (respectively 2% with respect on bare cable width) to the nominal dimensions of the winding pack (see chapter 3).

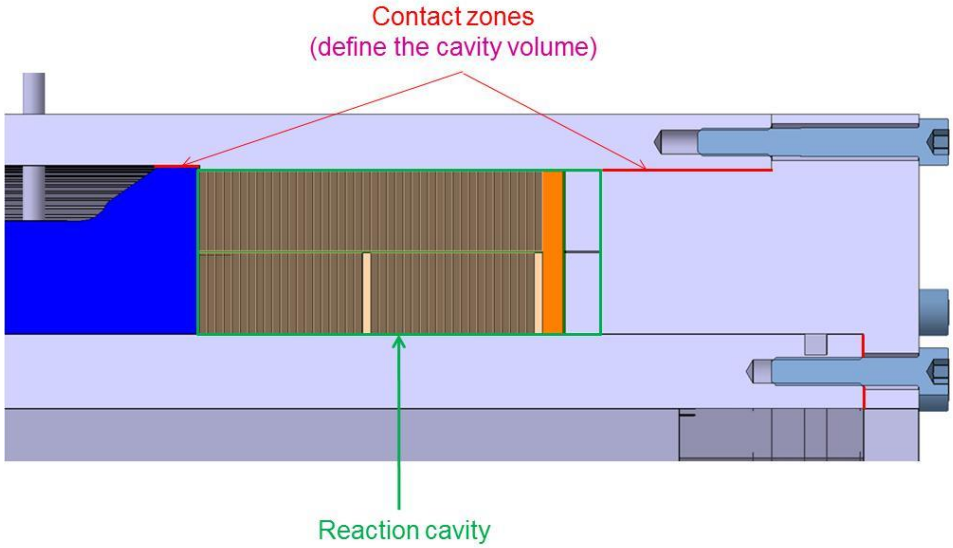

Fig. 6.2.2 – Section of the reaction tooling illustrating the reaction cavity.

An extra length of Nb_3Sn conductor is left at each end of the coil to allow TIG welding of the strand ends in order to avoid tin leakage during the heat treatment. Furthermore in the splice zones, the conductor will be protected using temporary support pieces.

When the reaction mold is closed, the coil is safe and can be transported to the reaction site.

6.3.2 Reaction cycle

The coil (inside of its reaction mold) will be inserted into the reaction furnace. It will undergo the required heat treatment cycle under argon flow. The heat treatment cycle has been defined in order to optimize the conductor properties: ramp until 620°C at 50°C/h - step at 620 °C for 120 h - ramp until 650 °C at 50°C/h - step at 650 °C for 90 h – natural cooling down.

6.3 Coil impregnation

6.3.1 Testing

The impregnation mold undergoes a sealing test. The exit hole is closed and residual air is pumped by the entry hole. Vacuum leaks in the mold are then tracked.

Then a second quick test is done by injecting air in the entry hole and by checking if it exits by the exit hole. This is meant to confirm that the resin can circulate correctly from the entry to the exit without being blocked by something in the mold.

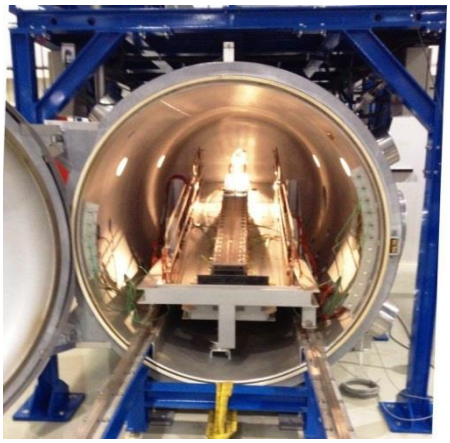

Fig. 6.3.1 – Vacuum chamber used for impregnation.

6.3.2 Setup

The coil is inserted inside of a dedicated impregnation mold represented on Figure 6.3.2. This assembly is inserted in the vacuum chamber with a tilt of minimum 15° and with the exit hole at the top.

The vacuum chamber is heated at 40°C in 48h in a vacuum of 10^{-1} mbar in order to dry it and to remove the air from the coil perfectly.

All the steps of the impregnation process must be done at 40°C.

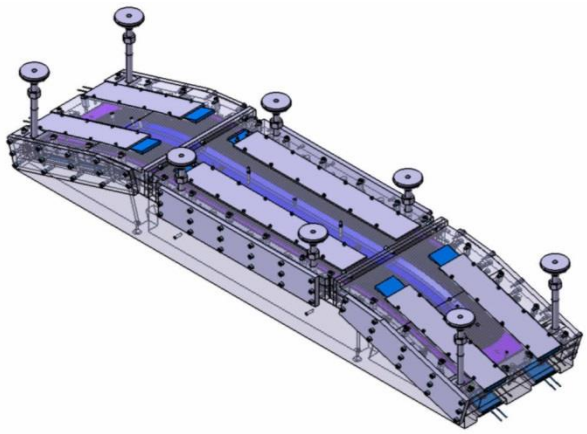

Fig. 6.3.2 – Impregnation mold of coil 3-4 (CAD view).

6.3.3 Preparation of the resin

We will use the two following components: Araldite MY750 resin and Hardener Jeffamine D400.

They must be heated at 40°C for a minimum of one hour before being mixed, in order to increase their fluidity and to get rid of humidity.

The volume needed for the impregnation and mix (in weight proportion) is as follow:

Resin Araldite MY750	100
Hardener Jeffamine D400	57

When these components are mixed, the impregnation must be done within 3 hours before the gelation of the mixture.

The mixture is mixed and degassed in a recipient above the vacuum chamber in a highest vacuum than the vacuum in the impregnation chambers to avoid any new degassing in the mold during impregnation.

The mixing and degassing times are estimated around 30 to 45 minutes.

6.3.4 Impregnation

When the mix is correctly degassed, we can inject it into the mold. We open the connection between the recipient which contains the mix and the impregnation mold.

The mix goes into the mold by gravity and capillarity. Time estimated for the resin to cross the mold is between 1 and 1.5 hours.

When the resin is visible at the exit end of the mold, the arrival of the resin can be stopped. The vacuum chamber can stay 30 to 45 minutes in vacuum in order to be sure the resin has gone in every tight zone.

6.3.5 Curing cycle

The vacuum is then broken, the entry of the mold is closed and the curing cycle is done by increasing the temperature from 40° to 80°C. The curing cycle at 80°C lasts 10 hours.

Afterwards, the coil can be unmolded.

6.4 Magnet assembly

The FRESCA2 coils will be heat treated and impregnated in building 927 (Figure 6.4.1). The capacity of the crane in 927 is 7.5 tons. The estimated weight of FRESCA2 magnet is about 9 ton. Therefore, an assembly area had been dedicated in building 180 which has a crane capacity of 40-60 ton (Figure 6.4.2).

Fig. 6.4.1 – Cern Prévessin-site building 927.

Fig. 6.4.2 – Cern Meyrin-site building 180.

6.4.1 Coil-pack assembly

Coil-pack assembly sequence

The first step of the coil assembly sequence is to put the coil layer 3-4 on top of coil layer 1-2 and this is shown in Figure 6.4.3. Special tooling for handling the coils has been designed. The facing surfaces of the coils will be mold-released. The gap in-between coils will be filled with 0.9 mm fiber-glass cloth which will be impregnated using the coils as cavity. This technique will guarantee perfect contact in-between the two coils and also allow separating the coils in case of failure of one of them. Figure 6.4.4 shows an assembled coil.

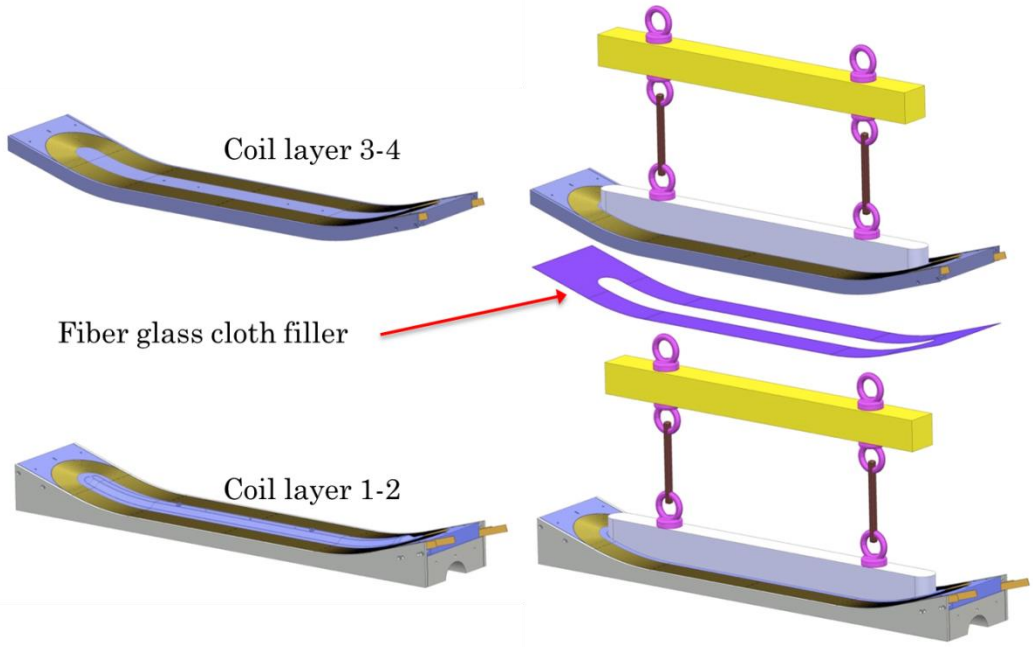

Fig. 6.4.3 – Coil assembly sequence: coil 3-4 on coil 1-2.

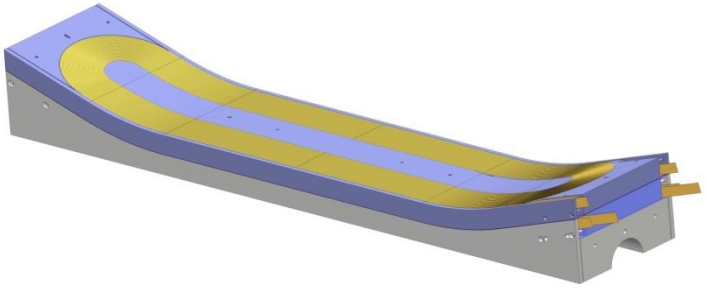

Fig. 6.4.4 – Assembled coil.

The second step of the coil assembly sequence is to put the coils on the vertical pads. Special tooling for rotating each coil has been also designed. As shown in Figure 6.4.5, one coil is lifted and rotated in order to put it on top of the vertical pads. Then the other coil is lifted and put it on the first coil with a fiber-glass cloth in between them. Then the second vertical pad is put on top of the other components.

At this point we have the coils and vertical pads together as shown on top of Figure 6.4.6. The third step is to put into contact the horizontal pads on each side, and bolt everything together in order to have the *coil-pack* assembled. Special tools for lifting and rotating the coil-pack have been designed as shown Figure 6.4.7.

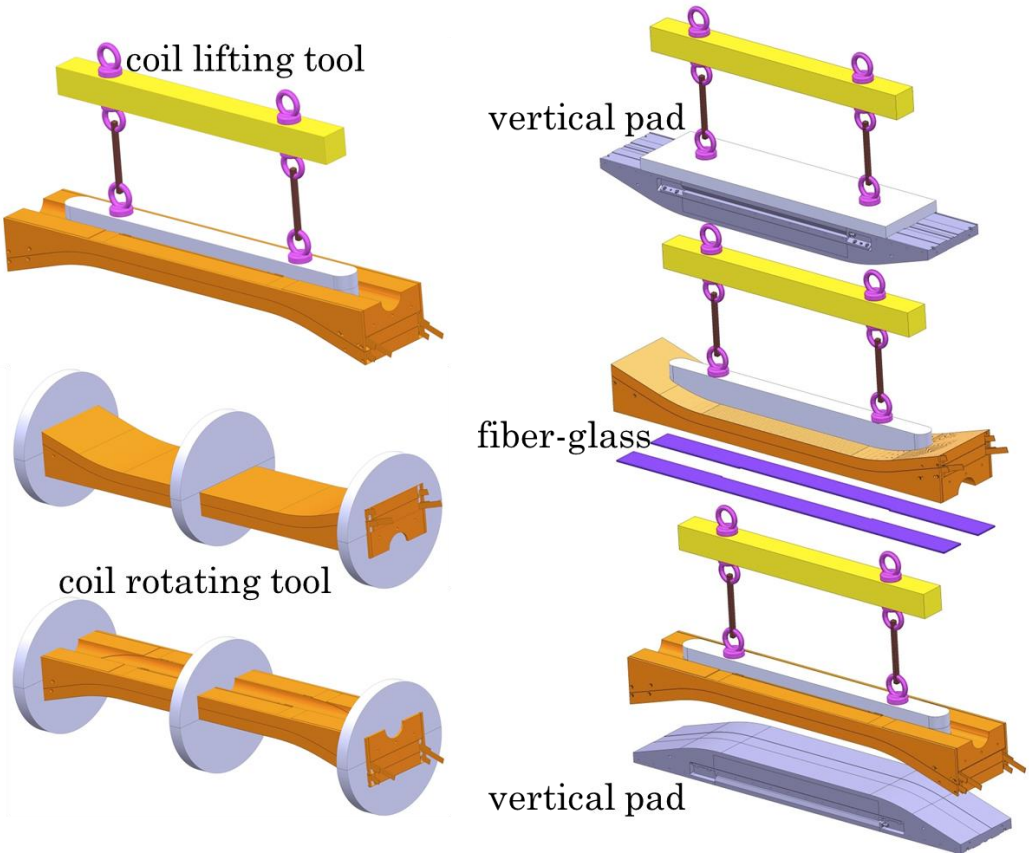

Fig. 6.4.5 – Coil assembly sequence: coils on vertical pads.

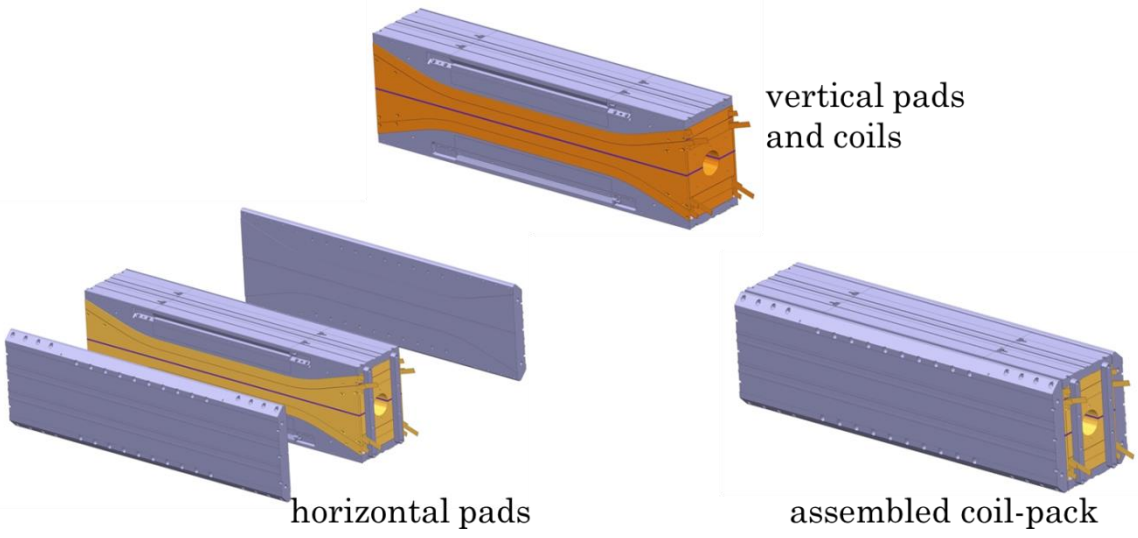

Fig. 6.4.6 – Coil-pack assembly.

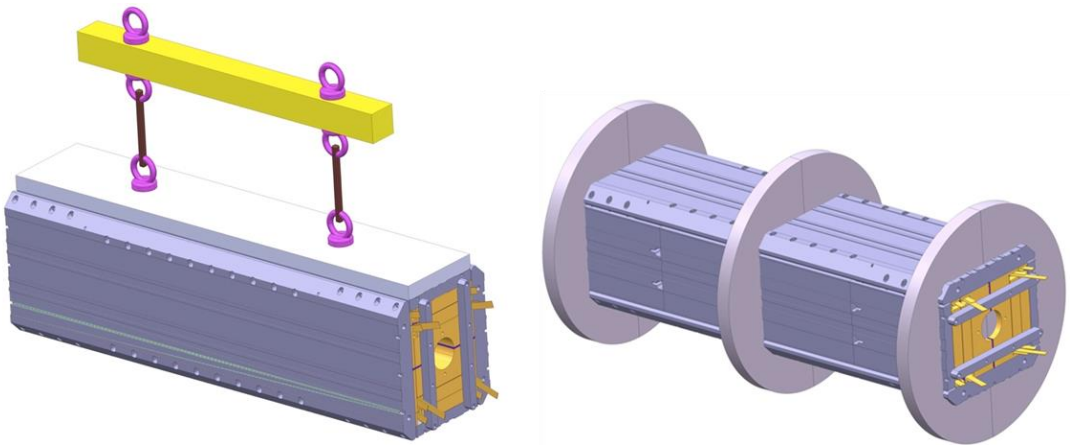

Fig. 6.4.7 – Coil-pack lifting and rotating tools.

First coil-pack assembly with dummy-coils

The first mechanical coil-pack assembly has been performed using Aluminum blocks replacing the superconducting coils (Figure 6.4.8). This will qualify the magnet structure, the assembly and loading procedure, and validate the FEM model. Each of the aluminum *dummy coils* has been instrumented with seven strain gauge stations measuring along azimuthal and longitudinal direction (Figure 6.4.9).

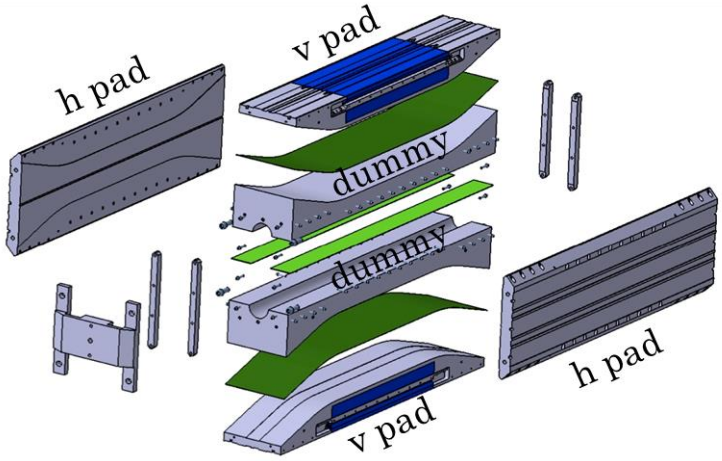

Fig. 6.4.8 – Dummy coil-pack assembly.

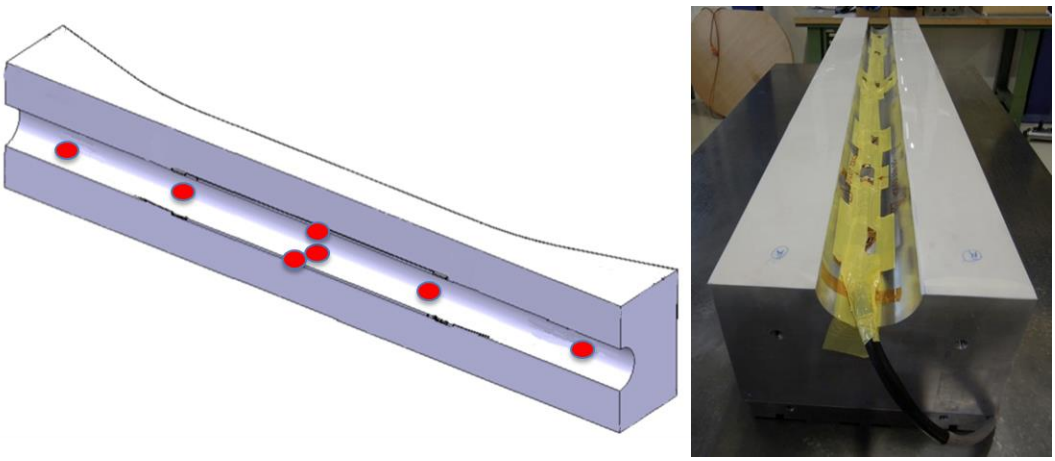

Fig. 6.4.9 – Localization of the strain gauge stations on a dummy coil.

Therefore for this case the components of the coil-pack are the two dummy-coils, two vertical and two horizontal pads (Figure 6.4.10). The contact surfaces between dummy-coils and the pads have been checked using pressure-sensitive paper. In Figure 6.4.11 is shown that there is a good contact and the pressure is very well distributed on both sides. The first coil-pack assembly with dummy-coils is shown in Figure 6.4.12. The coil-pack weight is about 2 tons.

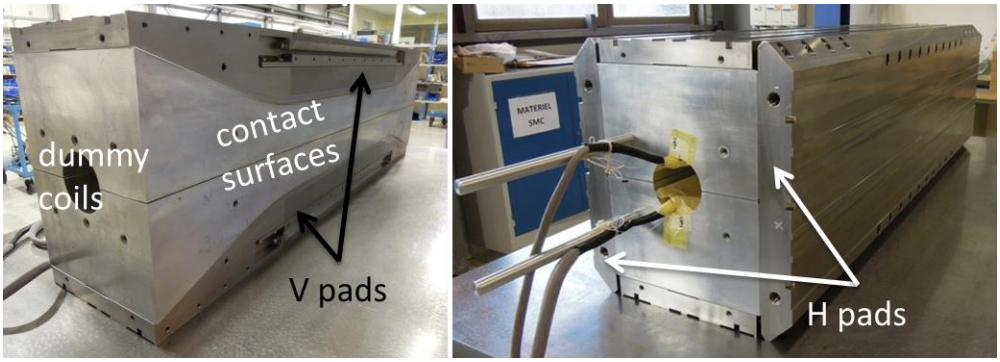

Fig. 6.4.10 – Coil-pack with dummy-coils.

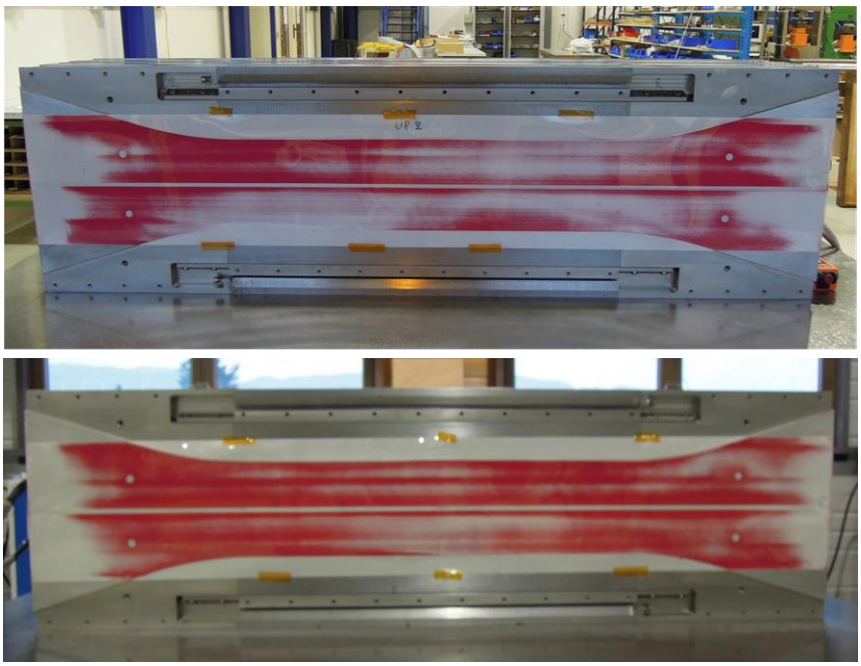

Fig. 6.4.11 – Pressure-sensitive paper on contact surfaces of dummies and h-pads.

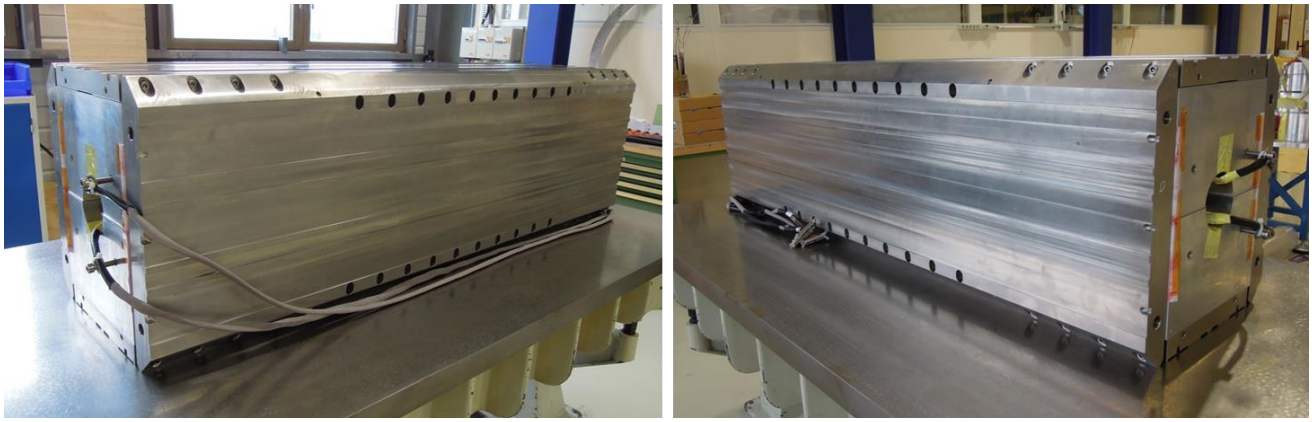

Fig. 6.4.12 – Coil-pack assembled with dummy-coils.

6.4.2 Structure assembly

Sliding the shell

As a first step of the magnet structure assembly, the halves yokes are put together and aligned without any gap in between them (Figure 6.4.13). The weight of each halve yoke is about 2,400 kg. Figure 6.4.14 shows the aluminum shell sliding around the halves yokes, with a detailed view of some rollers used to guide the shell with the yoke and to facilitate the insertion. The weight of the shell is about 860 kg.

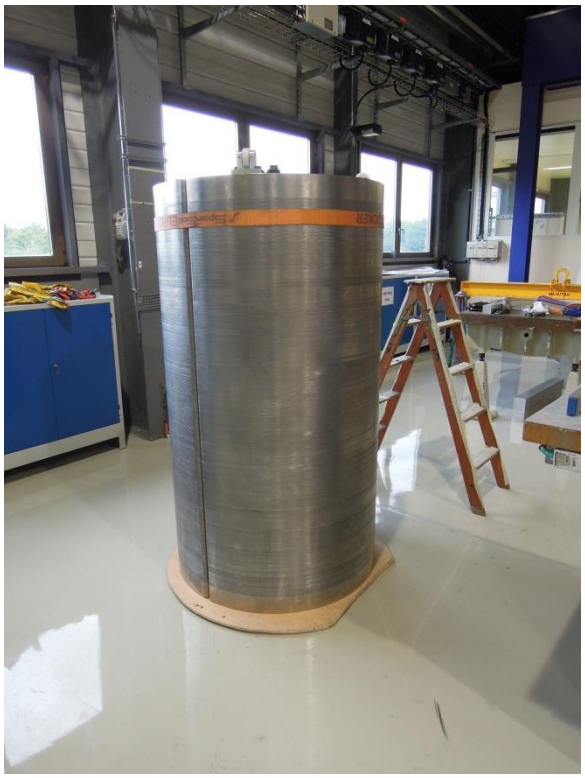

Fig. 6.4.13 – Structure assembly: the halve yokes into contact.

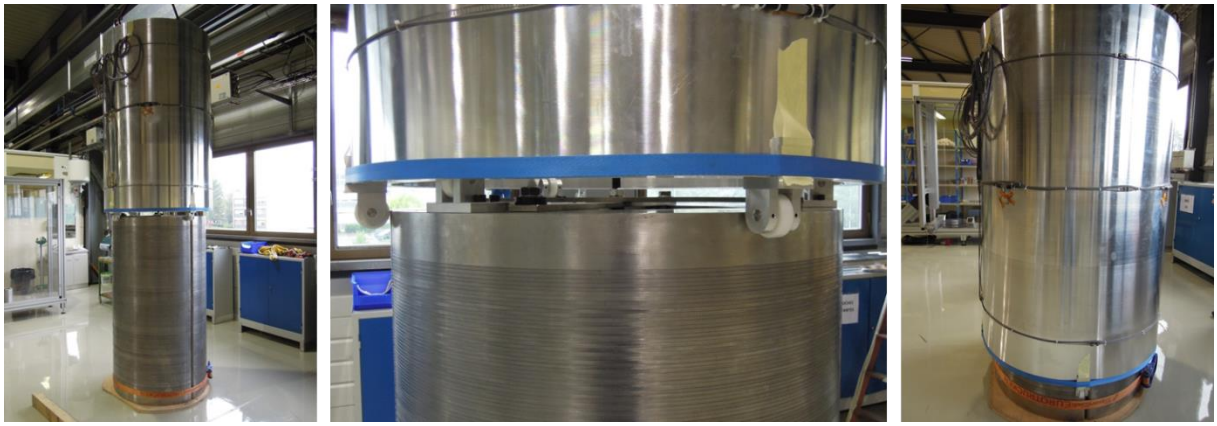

Fig. 6.4.14 – Structure assembly: sliding the shell around the yokes.

Yoke-gap keys insertion

A system of standard hydraulic jacks was used to push the halves yokes towards the shell inner radius in order to allow the insertion of the temporary keys and bladders insertion (Figure 6.4.15). This system is put in between the halve yokes to spread the yokes apart creating a clearance in between in order to insert temporary keys in (Figure 6.4.16). These temporary keys ensure the gap to the bladders insertion. So, bladders are inserted in between the half-yokes. Then, with these bladders, a clearance is generated to insert the yoke-gap keys, thus ensuring tight contact between yoke and shell.

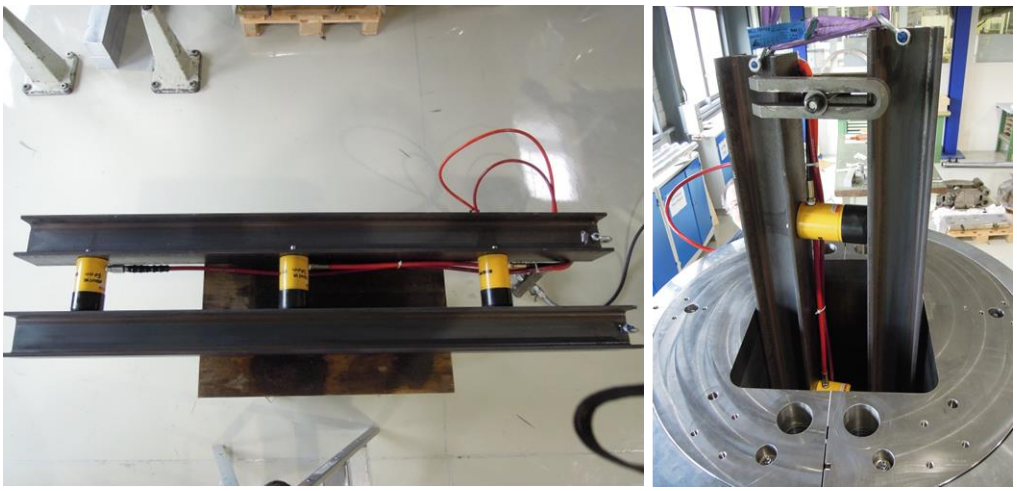

Fig. 6.4.15 – Structure assembly: pushing the yokes towards the shell.

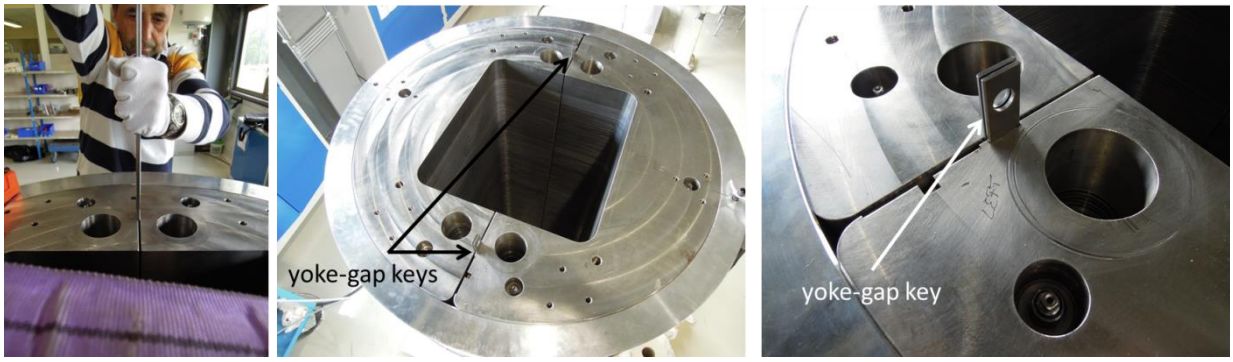

Fig. 6.4.16 – Structure assembly: insertion and location of yoke-gap keys.

Coil-pack insertion

A CERN standard rotating device is used to rotate the magnet structure from vertical to horizontal position (Figure 6.4.17). A support structure was used to clamp the magnet structure to the rotating device (Figure 6.4.18).

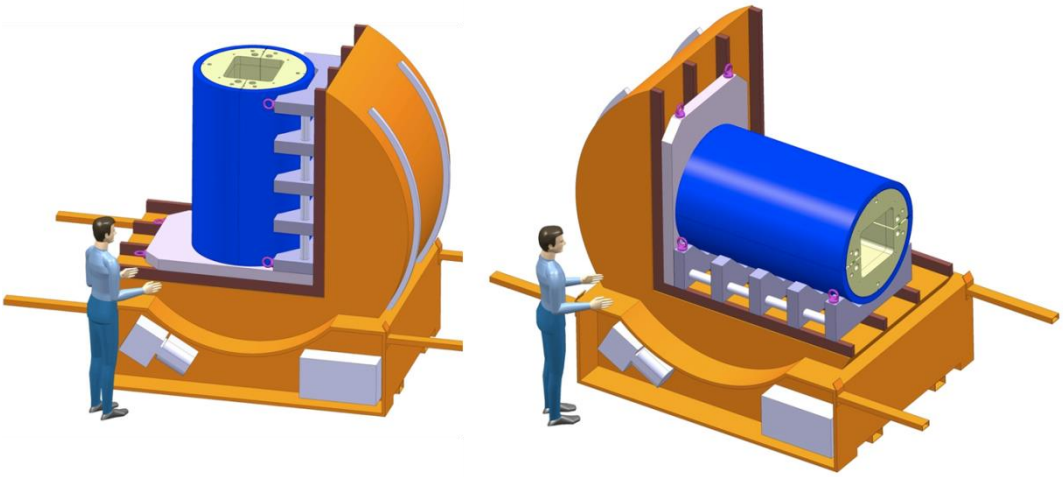

Fig. 6.4.17 – Rotating device.

Fig. 6.4.18 – Structure on the rotating device.

The next step was to transport yoke and shell to the assembly-table (Figure 6.4.19). Bearing rollers were used to slide the coil-pack into the yoke. Then the coil-pack was transported to the assembly table in order to be pushed into the yoke aperture (Figure 6.4.20).

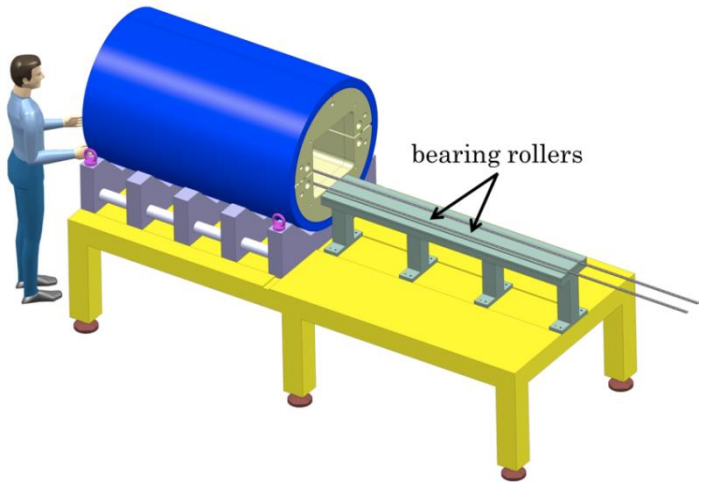

Fig. 6.4.19 – Assembly table.

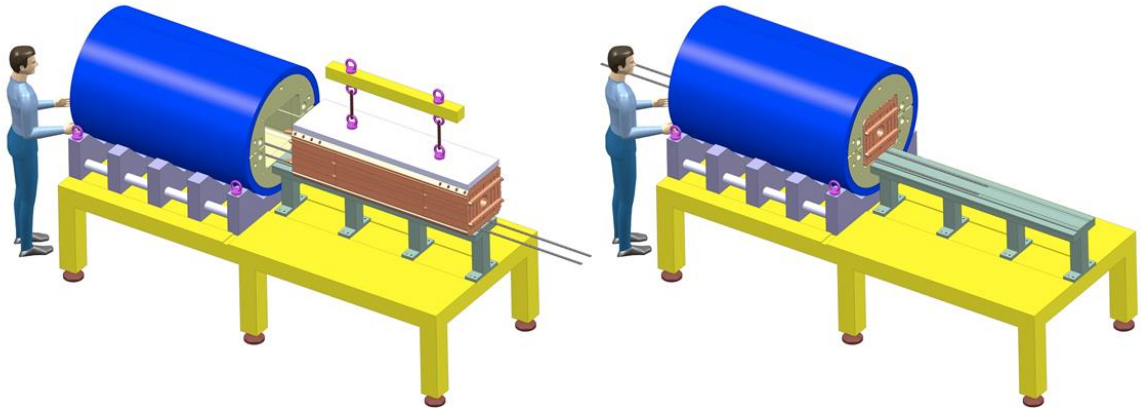

Fig. 6.4.20 – Insertion of the coil-pack into the yoke.

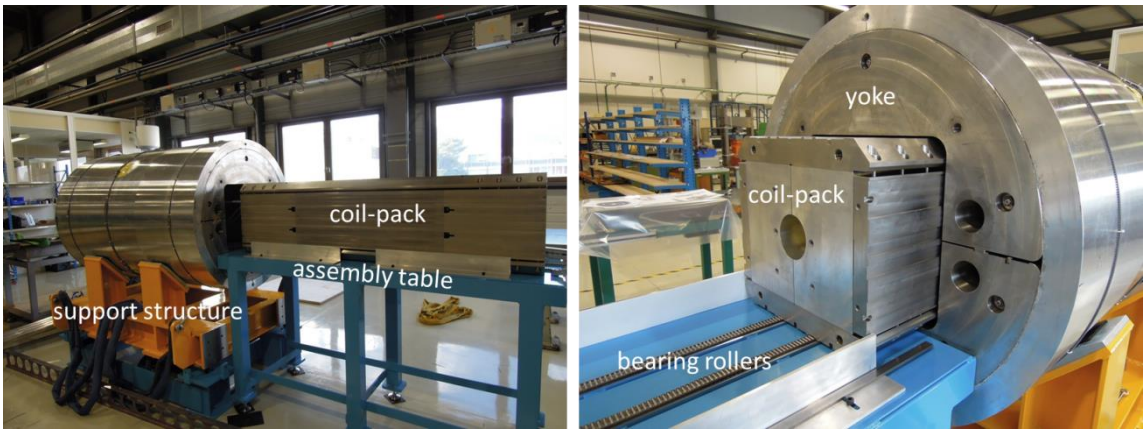

Fig. 6.4.21 – Assembly table, insertion of the coil-pack.

Insertion of the interference keys

After the insertion of the coil-pack in the yoke (Figure 6.4.21*Fig. 6.4.*), a loading operation was performed using bladders placed in between pads and yoke. By pushing the yoke against the shell and compressing the coil-pack, the bladder pressurization allows removing the yoke-gap keys and inserting the interference-keys. This represents an intermediate loading operation aimed at pre-loading the coil-pack.

Fig. 6.4.22 – Coil-pack inserted into the yoke.

Three vertical bladders were used to lift the coil-pack and remove the rollers. Temporary keys were inserted to center the coil-pack into the yoke aperture (Figure 6.4.23).

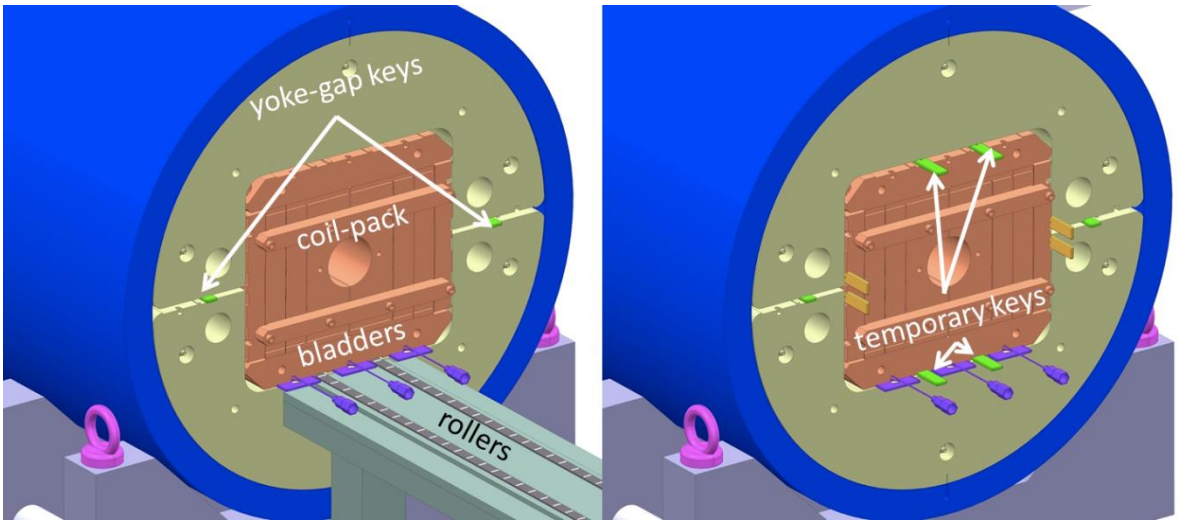

Fig. 6.4.23 – Lifting the coil-pack, removing the rollers.

The rest of the horizontal bladders are then inserted, and all of them are pumped in order to insert the horizontal keys to obtain a tight assembly of the coil-pack (Figure 6.4.24). The vertical bladders are inserted, and then pumped in order to insert the vertical keys (Figure 6.4.25). The vertical shimming is gradually increased and finally the horizontal shimming to reach the defined pretension of the shell. A final configuration after loading operation is shown in Figure 6.4.26.

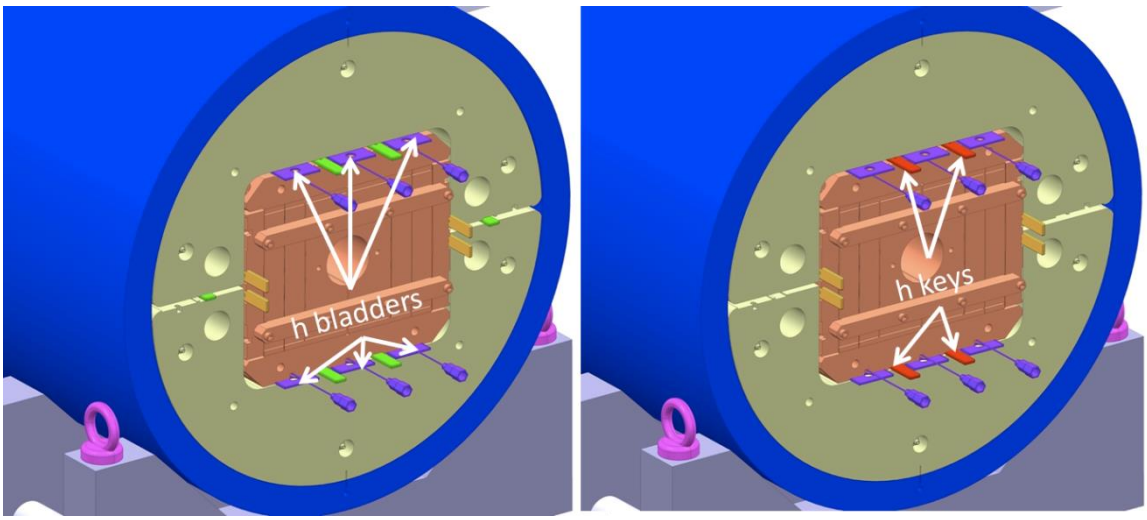

Fig. 6.4.24 – Pumping the horizontal bladders, insertion of the horizontal keys.

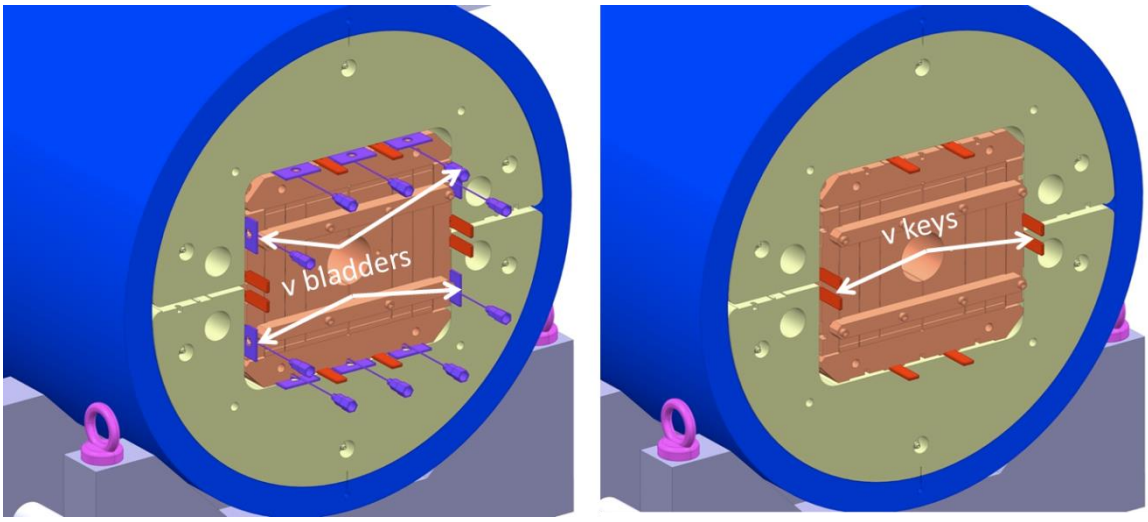

Fig. 6.4.25 – Pumping the vertical bladders, insertion of the vertical keys.

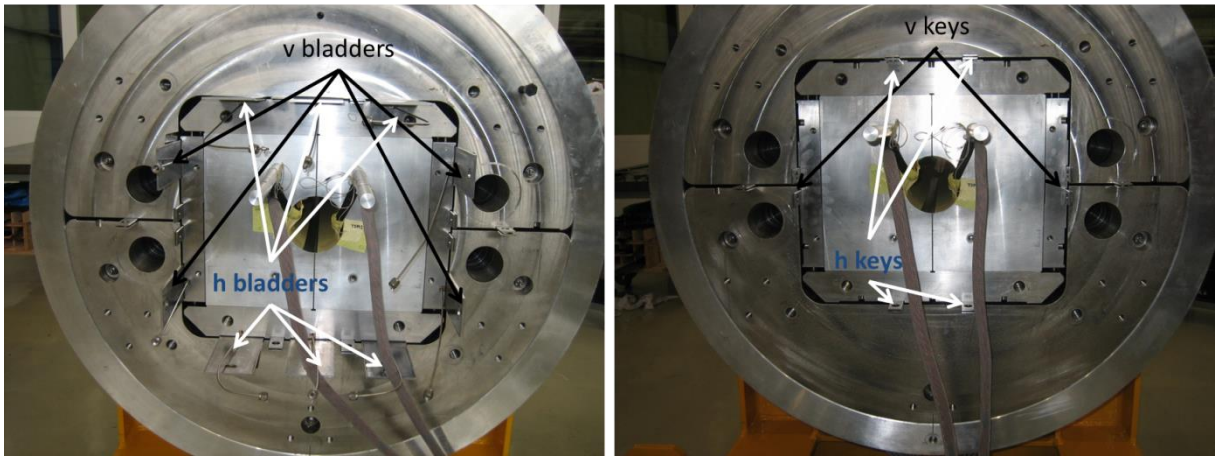

Fig. 6.4.26 – Bladders location and final key configuration.

Longitudinal compression system

As a next step, the longitudinal compression system is assembled and pre-loaded with a hydraulic tensioning fixture. The longitudinal compression system is composed of two end-plates on each side of the magnet structure, which compress directly four aluminum rods (Figure 6.4.27). The rods were instrumented with strain gauge stations measuring along the longitudinal direction (at this point, a bladder operation to change coil-pack pre-tension still remains possible after assembly of the end-plates). Figure 6.4.28 shows the rods inserted in the yoke, and end-plate. A 200 tons hydraulic piston shown in Figure 6.4.29 was used to pre-tension the rods to the targeted stress value at room temperature. Figure 6.4.30 shows the transportation frame for the magnet structure.

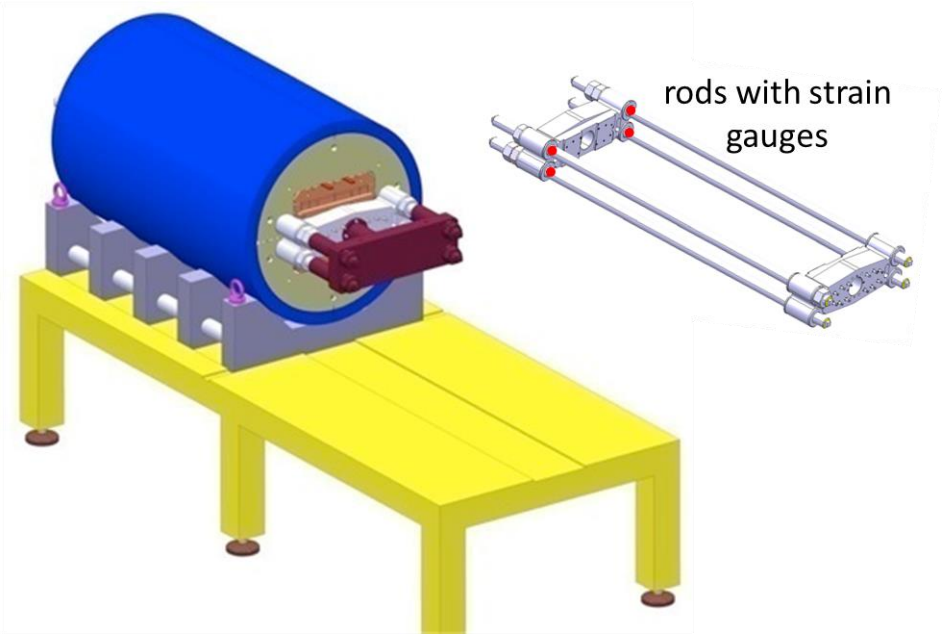

Fig. 6.4.27 – Assembly with the longitudinal compression system.

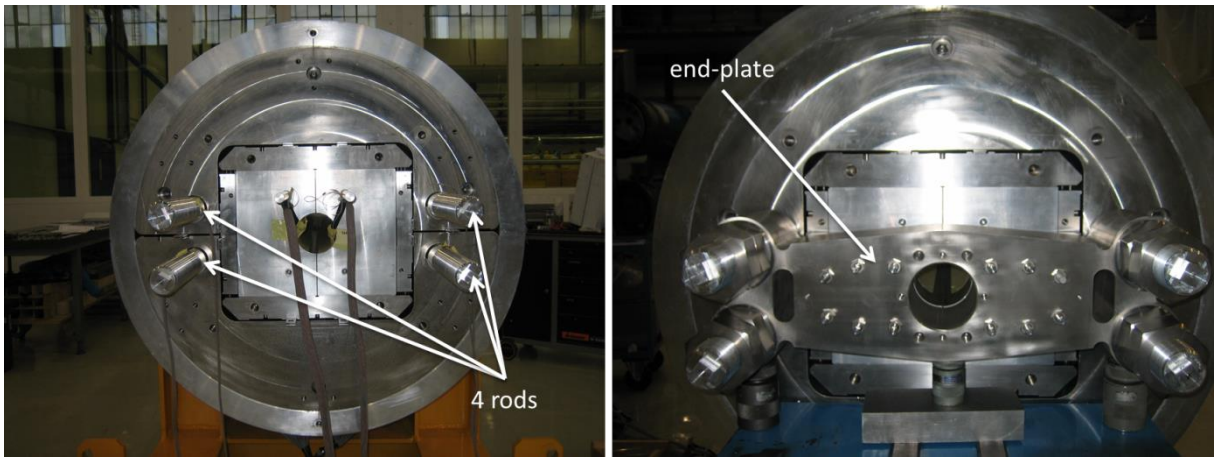

Fig. 6.4.28 – Longitudinal compression system; rods and end-plate.

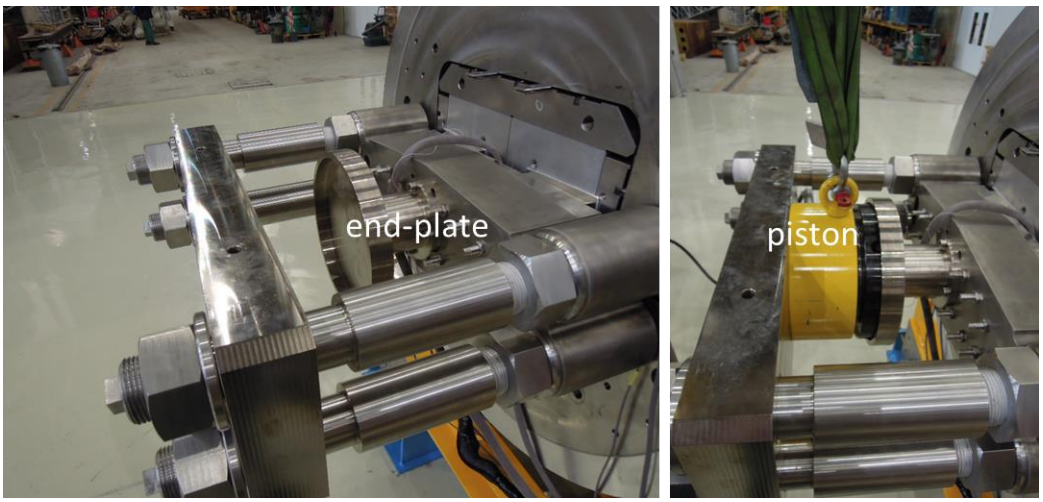

Fig. 6.4.29 – Hydraulic feature to pre-tensioning the rods.

Fig. 6.4.30 – Magnet structure ready to be transported.

7. Test program

Before designing winding and reaction tools, some preliminary tests have been carried out in order to check winding geometry and procedure and compare possible options. During winding, the conductor needs to be kept under tension to prevent it from twisting on its winding spool and to maintain it in place against winding mandrel; on the other hand too much tension could destabilize the cable causing strands popping out of the cable. First bending tests aimed at determining the correct tension to apply on the cable during the different phases of the coil winding: straight section, easy way bending zone, hard way bending zone, interlayer jump region. Those tests are described in the next paragraphs.

Once the coils wound, reacted, impregnated and instrumented, they will be assembled inside the mechanical structure described in chapter 5. The bladders and keys system will provide part of the pre-stress on the coils at room temperature, and the surrounding aluminum shell will provide the rest at cold. Before the magnet assembling, the structure has been tested using aluminum dummy coils in order to validate the pre-stress application procedure and the structure behavior between room temperature and 77K. The structure test is described in paragraph 8.9.

7.1 Bending test

Some bending tests have been carried out in order to evaluate cable behavior when it is forced to bend in the so called easy way (around a circular end piece). First bending tests, around a circular planar mandrel, aimed at determining the correct tension to apply on the cable during the bending of the ends. Then a second tests campaign has been carried to evaluate the impact on cable mechanical behavior of the so called hard way bending (in the plane of the big face of the cable) necessary for coils with flared end. A special tool has been designed and realized in order to be able to wind a short coil with one plane end and one flared end. It is represented on Figure 7.1.1. Different parameters (angles and lengths) of the coil geometry have been tested and compared. Those parameters are represented on Figure 7.1.2.

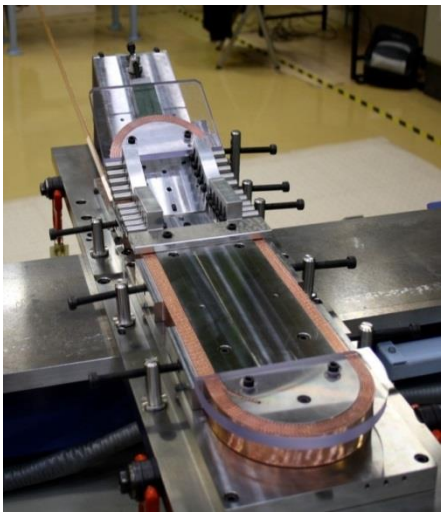

Fig. 7.1.1 – Bending test tooling.

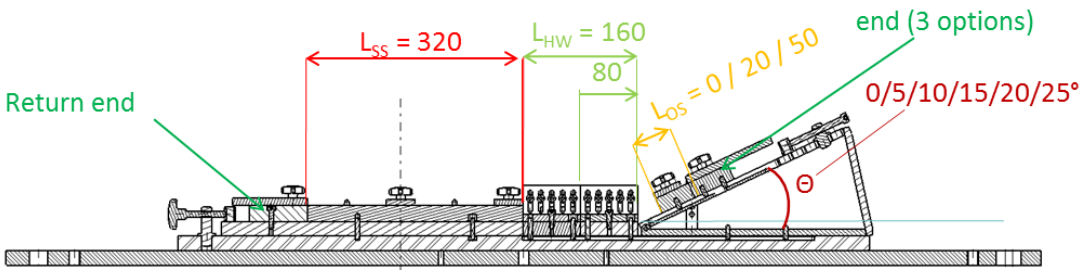

Fig. 7.1.2 – Bending test parameters.

The test was also used to compare three geometrical options for the coil end geometry. They are represented on Figure 7.1.3. The goal was to try to minimize discontinuities in the bending energy along the cable path.

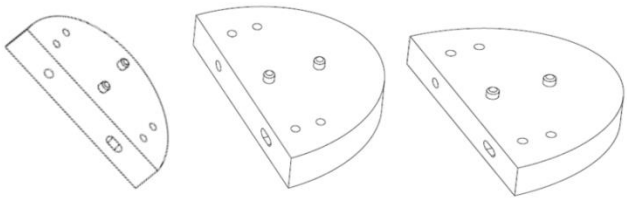

Fig. 7.1.3 – Options for the end geometry: circle (left), ellipse (mid), clothoid (right).

The main conclusion of the test has been to confirm the flared end option was technically possible with our cable geometry, without excessive cable deformation, provided the hard-way bend radius is large enough (see Figure 7.1.4). Consistent with the experience from LBNL, a minimum value of 700 mm has been fixed.

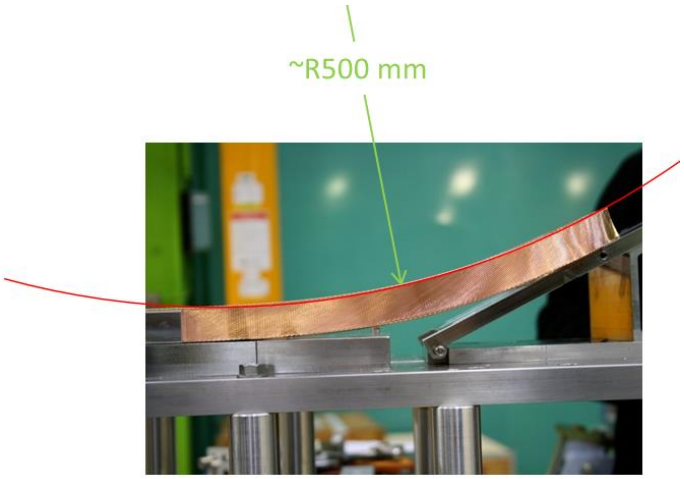

Fig. 7.1.4 – Close-up on the hard-way bend zone.

7.2 Winding orientation test

Winding tests to optimize ends geometry have been realized with the flared end turned up (Figure 7.2.1) but this is not the easiest way to wind.

Fig. 7.2.1 – Winding tests with flared end turned up.

The bending tool has been then modified in order to allow winding with the flared end upside down (Figure 7.2.2).

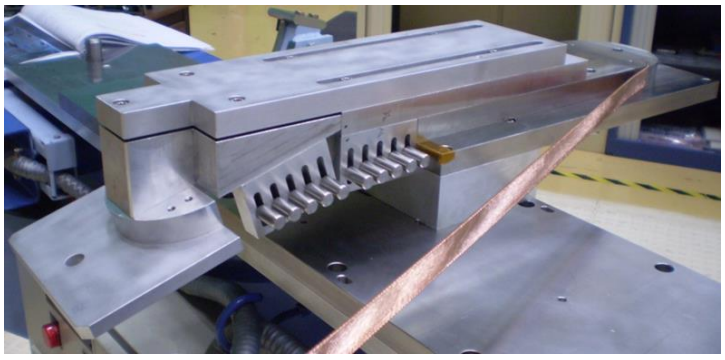

Fig. 7.2.2 – Upside-down winding tests tools.

Three turns have been wound successfully, in an easier way than with the ends turned in the other side (Figure 7.2.3).

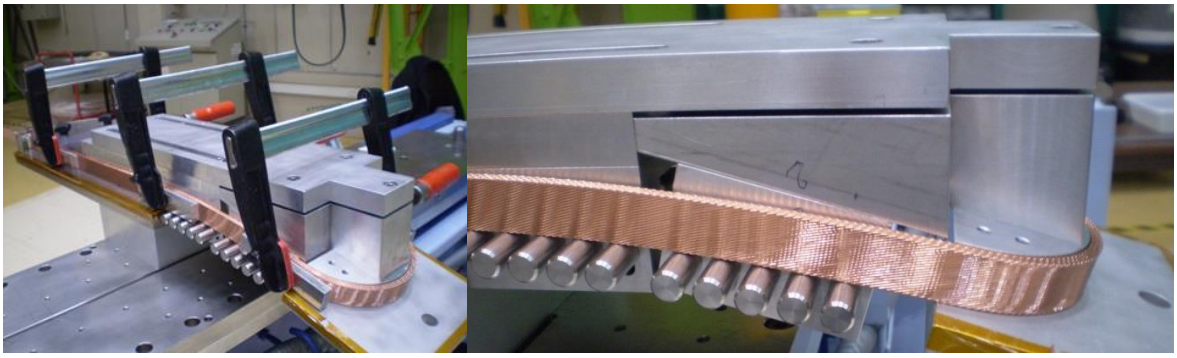

Fig. 7.2.3 – Upside-down winding.

With flared end upside down we do not need supports on conductor upper face in the hard way bend zone and this can contribute to limit cable insulation damaging during winding. The configuration upside down has been validated for FRESCA2 coils winding.

Once coil ends geometry has been defined and the winding process validated, the winding test with one flared end has been repeated while winding in the opposite direction in order to identify any difference in cable behavior depending on bending direction. The test confirmed that if for keystoned cables it is possible to identify a preferential bending direction, for rectangular cables winding direction is not an issue.

7.3 Layer jump test

The definition of the layer jump geometry is described in § 4.4.2.

A layer jump test has been done with two candidate geometries (one or two chicanes) in order to check in operational conditions if this design was acceptable. Bare copper cable was used, with the right section.

As shown on Figure 7.3.1, both geometries have given satisfying results. The ‘double chicane’ solution has been retained because it implies a thicker shim which is easier to put in place. Moreover, it provides better protection to the cable.

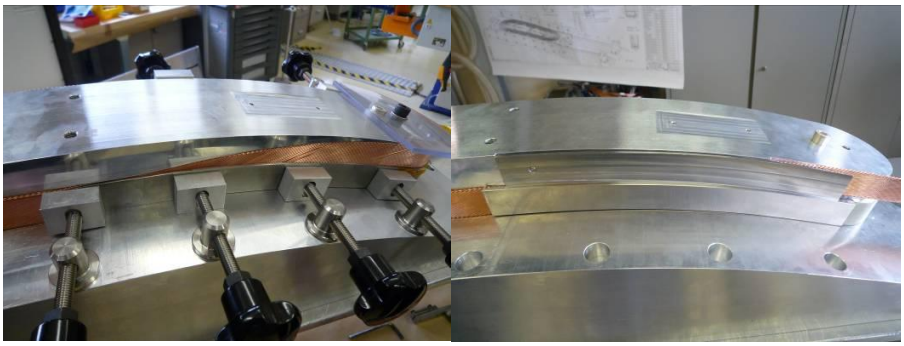

Fig. 7.3.1 – Layer jump test with one chicane (left) or two chicanes (right).

7.4 Dishing test

When the 20-mm wide FRESCA2 cable is submitted to bending, a deformation of its largest face can be observed (Figure 7.4.1).

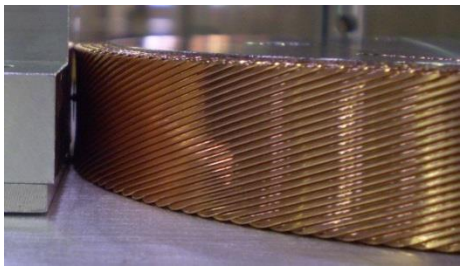

Fig. 7.4.1 – Close-up on the cable end.

The deformation is function of the bending radius: the smallest the radius, the biggest the deformation. Dishing phenomenon is intrinsic to Rutherford type cables and is more relevant in large cables like FRESCA2 cable. Two tests campaigns have been performed at Saclay in order to quantify dishing phenomena:

- First tests campaign has been performed on bare cable around a short planar mandrel (45 mm bending radius, 20 mm straight section) and aimed at identify cable dishing dependence from the winding tension. Dishing is measured by means of a comparator pointing at the middle height of the cable.

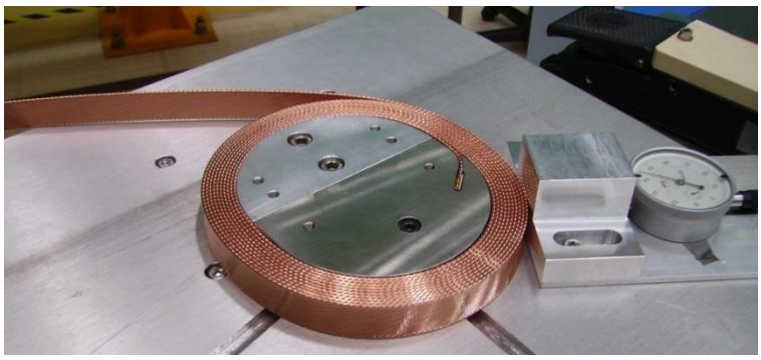

Fig. 7.4.2.

Tests have been performed with winding tensions of 10, 20 and 30 daN on up to 40 turns with no relevant impact on measured dishing. Dishing values up to 0.5-0.6 mm have been measured independently from the winding tension and number of turns.

- Second tests campaign has been carried out using the bending test tools to realize a 20 turns winding with one plane end and one flared end. Bending test tools has been slightly modified in order to allow dishing measurements in the middle of the ends and in one of the straight sections of the winding (Figure 7.4.3).

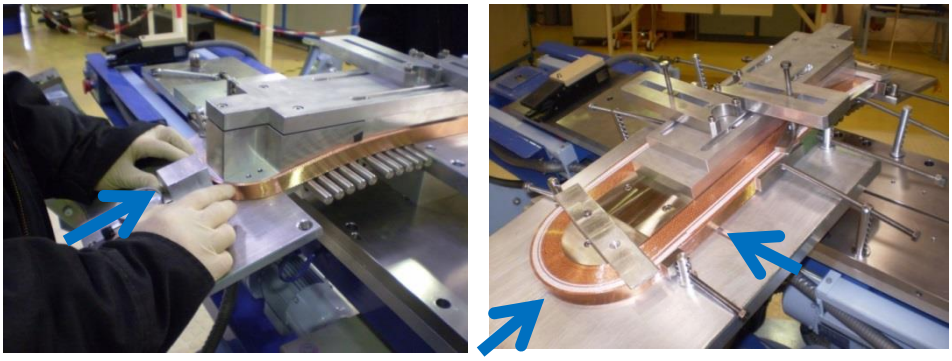

Fig. 7.4.3 – Dishing measurement during a 20 turns winding.

First turns have been realized with bare cable. Then the winding has been pursued for few turns with insulated cable before continuing anew with bare cable: the goal was to investigate the role of cable insulation in reducing or hiding dishing phenomena.

Dishing evolution during winding is reported in the graph on Figure 7.4.4. For comparison, also the curves of two tests carried out on the small planar mandrel are in the graph (short winding 1 and 3).

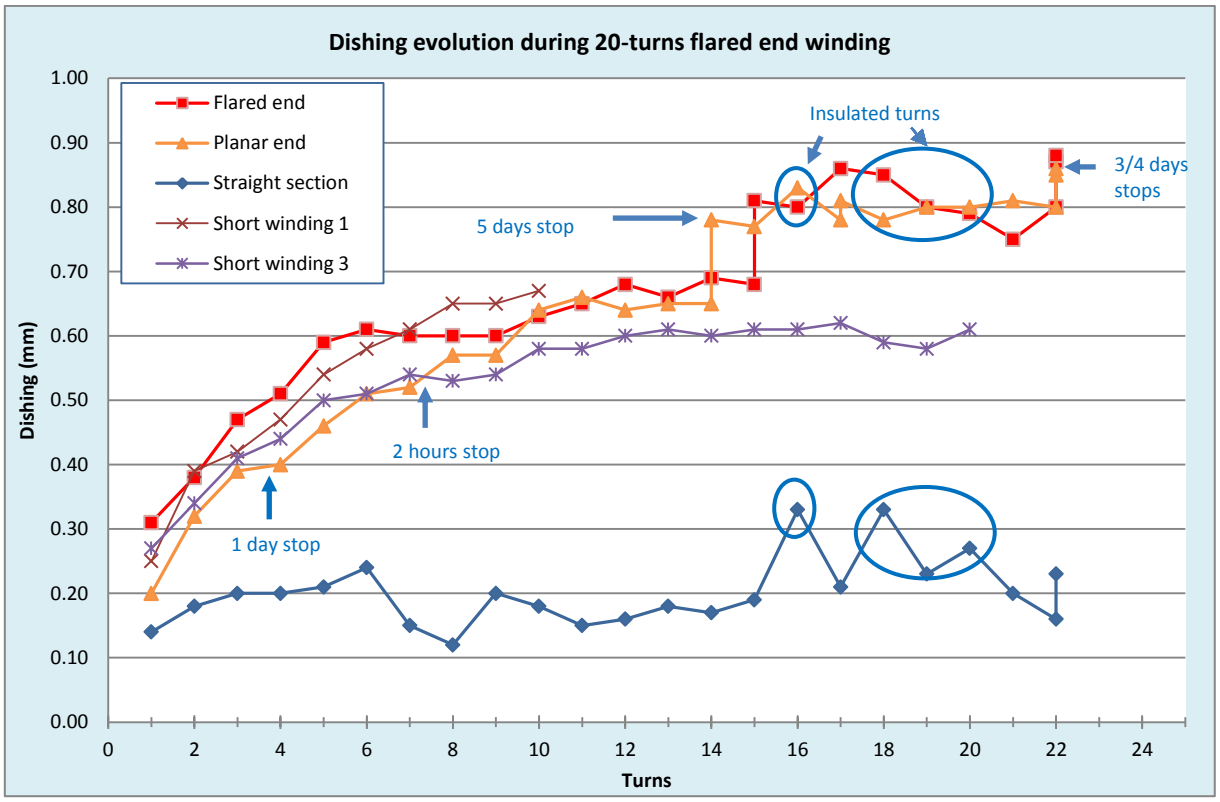

Fig. 7.4.4 – Dishing evolution during 20 turn flared end winding.

Dishing grows in the end parts a little bit more at each turn up to 0.9 mm, on the flared end faster than on the planar end. When the winding is stopped and paused (with cable kept in tension) dishing tends to increase.

Cable insulation masks the dishing of the cable but it does not affect its measurement.

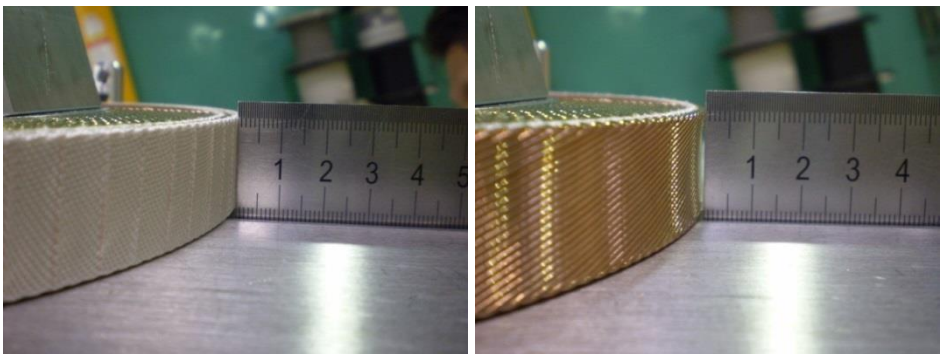

Fig. 7.4.5 – Conductor insulation, on the right, hide to the view the dishing in the cable but the comparator can measure the same dishing value than for the previous non-insulated turn.

7.5 Longitudinal dilatation tests

In order to investigate and measure the dimensional changes along the cable length during the heat treatment necessary for Nb_3Sn composite formation, a special tool has been designed and manufactured to allow the reaction of windings of few conductor turns with different mandrel configurations. During its formation, Nb_3Sn composite grows in volume resulting in an increase of strand and cable straight-sections; as a consequence, Nb_3Sn cable tends to contract in length. If the winding and reaction mandrel does not allow winding contraction, a tensile stress is created inside the Nb_3Sn cable, with a risk of degrading Nb_3Sn superconducting properties.

The dilatation tests mandrels, about 700 mm long and 90 mm wide, are made of 3 different materials: iron, stainless steel, and titanium alloy corresponding to the material candidates for FRESCA2 coils central posts. For each material, different winding configurations may be considered (Figure 7.5.1): a solid one-block mandrel, with no gaps, or a segmented mandrel, with up to three axial gaps in its length. On the end side of the winding, an extra length of 200 mm of cable is left unsupported working as a witness of stress occurrence.

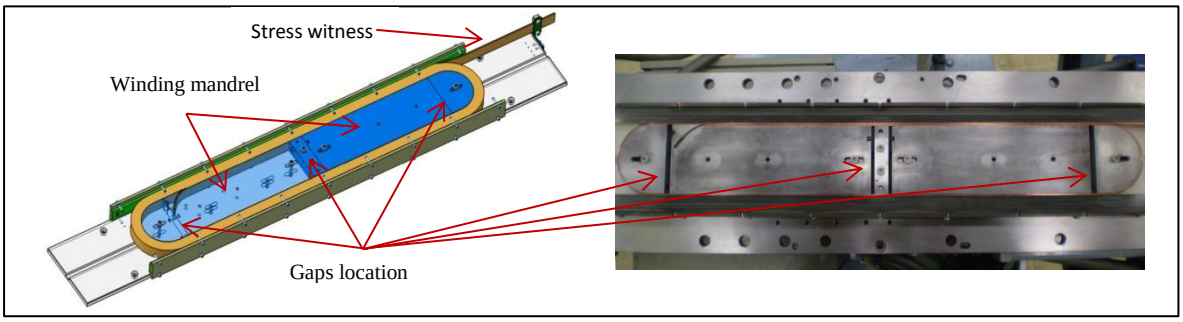

Fig. 7.5.1 – Designed and realized fixture for the dilatation tests.

Both PIT and RRP cables have been tested with this tooling. When wound around a closed mandrel, the winding not able to contract is submitted to a tension stress. This has been observed on all the closed mandrel configurations, independently from the mandrel material: in the non-supported region the cable collapses due du traction stress (Figure 7.5.2). Mandrel material has an impact on the maximal tension value but this is not easily to quantify; we could just observe that for instance in the case of the more expansive stainless steel mandrel the cable is more collapsed than for the less expansive titanium mandrel.

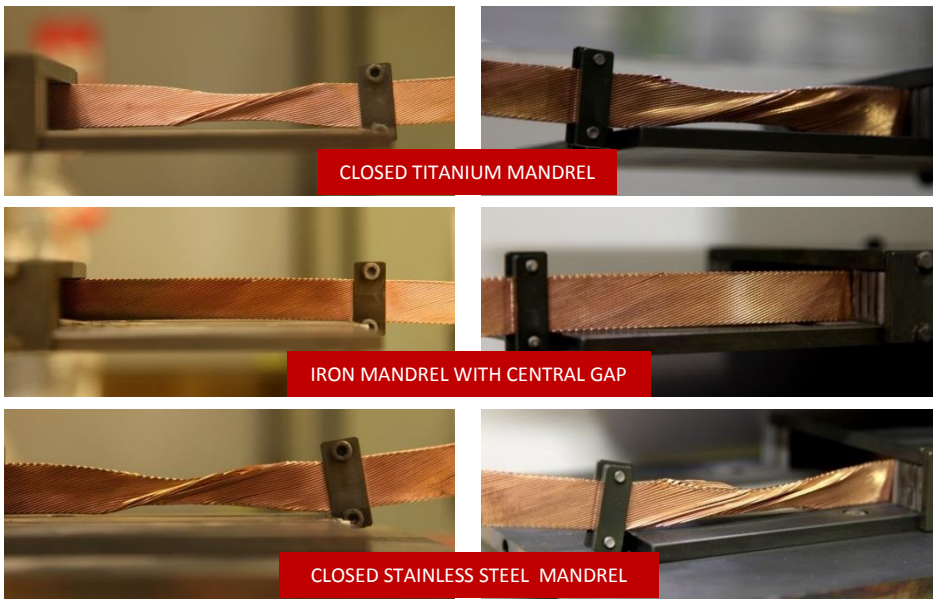

Fig. 7.5.2 – Designed and realized fixture for the dilatation tests.

Cable collapsing behavior under tension stress has been confirmed by traction tests carried out on 200 mm long cable samples. In Figure 7.5.3, traction test results on a non-reacted FRESCA2 cable; strand collapsing started at about 6.5 kN for non-reacted cable and at 3.5 kN for the reacted one.

Fig. 7.5.3 – Traction test on FRESCA2 cable.

Cable contraction seems to be quite independent from the location of the gaps, at least for planar winding.

Dilatation tests with open mandrels allowed identifying a difference in the behavior of PIT and RRP cables: the former one contracts by around 1% due to heat treatment, while the second one contracts by only 0.3%. These values will be taken into account for FRESCA2 coils reaction tooling design.

7.6 Insulation layer forming test

As shown on Figure 5.4.2, the coil pack assembly principle relies on the fabrication of tailored shims that will perfectly fill the space between the coils in order to ensure a good electrical insulation and a homogeneous mechanical support all along the coil.

These tailored shims will be made of fiberglass layers of variable thickness impregnated with epoxy resin. In order to get the perfect shape, they will be fabricated using the coils themselves as the mold.

A forming test, using aluminum plates, has been performed to check this principle. It has been successful.

7.7 Winding test

The full-size coil prototype is being wound using dummy copper cable. This winding operation relies on the winding tooling and procedure described in § 6.1. Figure 7.7.1 gives a view of the test after completion of the first layer. The coil prototype is one deliverable of the EuCARD project.

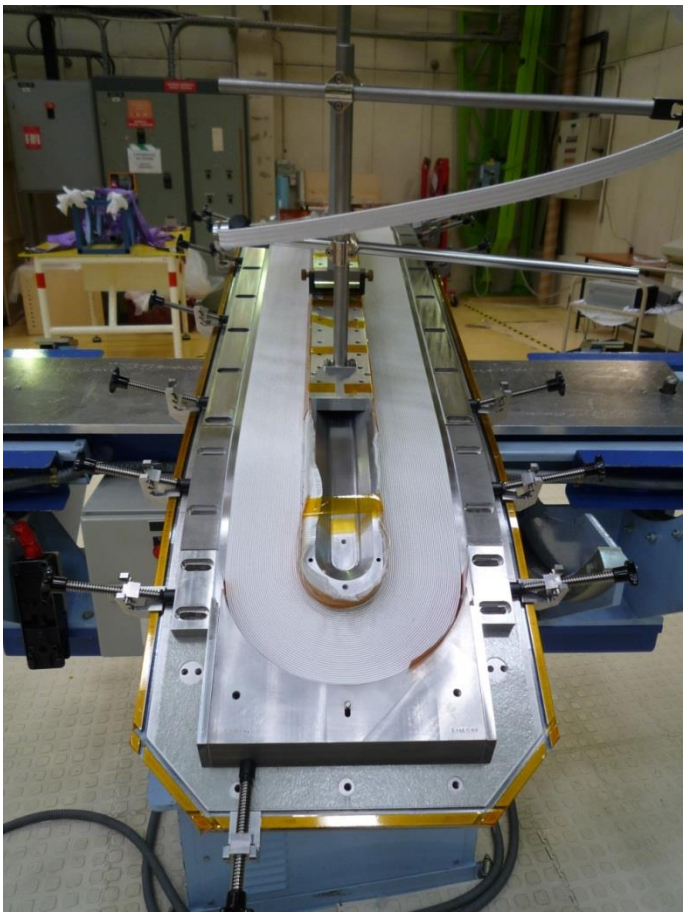

Fig. 7.7.1 – Winding test of full-size copper coil CC3401 (first layer complete).

After completion and analysis, this test will be extensively reported by the collaboration.

7.8 Cold mass nitrogen test

The cool-down test to 77 K with dummy coils will qualify the magnet structure, the assembly and loading procedure, and also validate the Finite Elements Model (FEM). FEM computations show that even with ΔT = 200 K and including pre-tension of the rods, there is 200 MPa margin before any yielding of the aluminum components which are the most sensible to thermal contraction. Therefore, taking this into account a maximum ΔT = 100 K temperature difference between the top and the bottom of each component was selected for the first cool-down test of the magnet structure with dummy coils.

7.8.1 Transport and rotation of the magnet structure

The magnet structure was transported to SM18 (Figure 7.8.1) where is rotated from horizontal to vertical position with the rotating device (Figure 7.8.2).

Fig. 7.8.1 – Magnet structure transported to SM18.

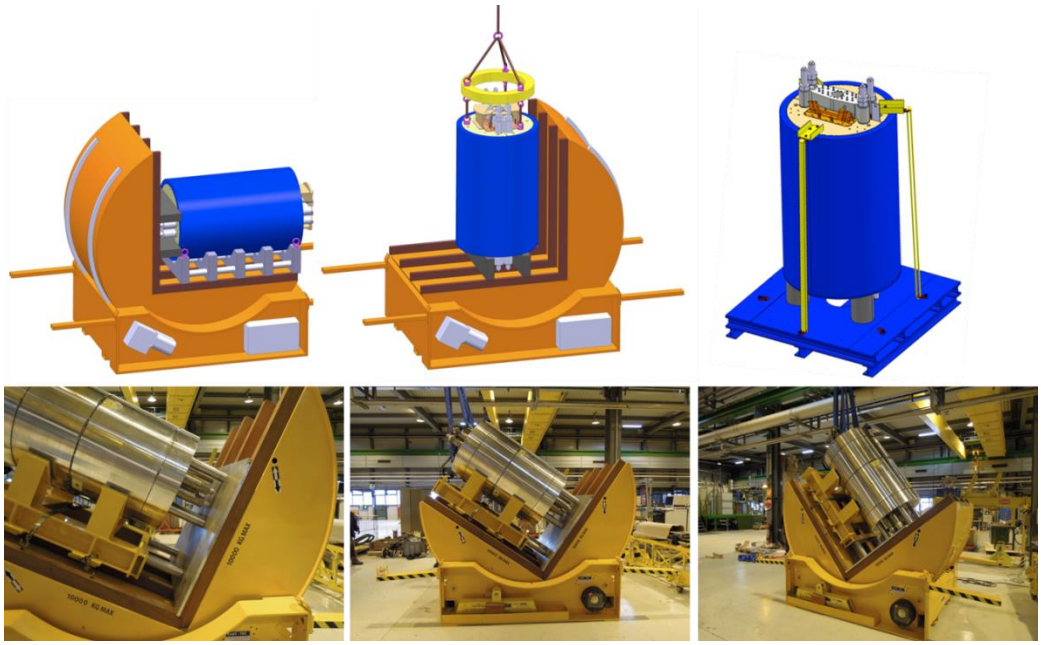

Fig. 7.8.2 – Rotating the magnet assembly.

7.8.2 Instrumentation: temperature sensors

Temperature sensors will be used to control de temperature gradient to ΔT=100K across the components of the magnet structure to limit thermal induce stresses. There are two sensors at the top and bottom of rod, yoke and shell; and top, middle and bottom of dummy coil. The location of temperature sensors is shown in Figure 7.8.3, their configuration in Figure 7.8.4 and one temperature sensor in Figure 7.8.5. A detailed view of one of the temperature sensors is shown in Figure 7.8.6.

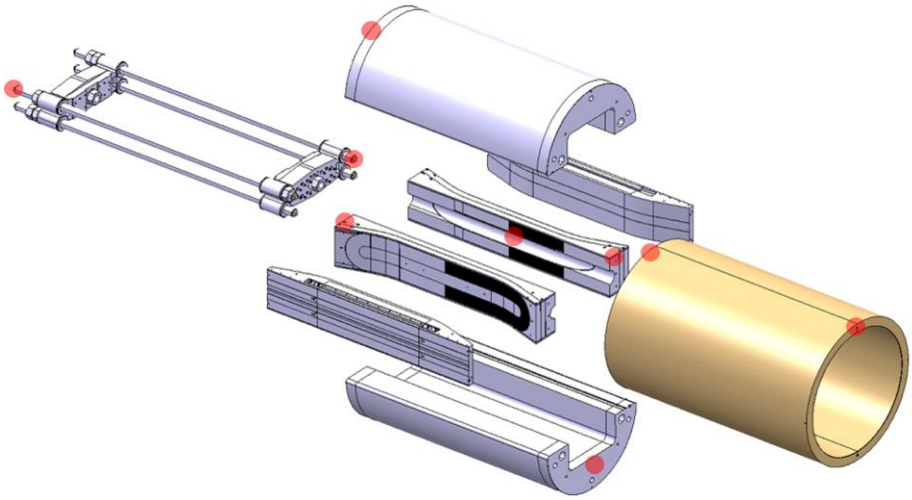

Fig. 7.8.3 – Location of temperature sensors.

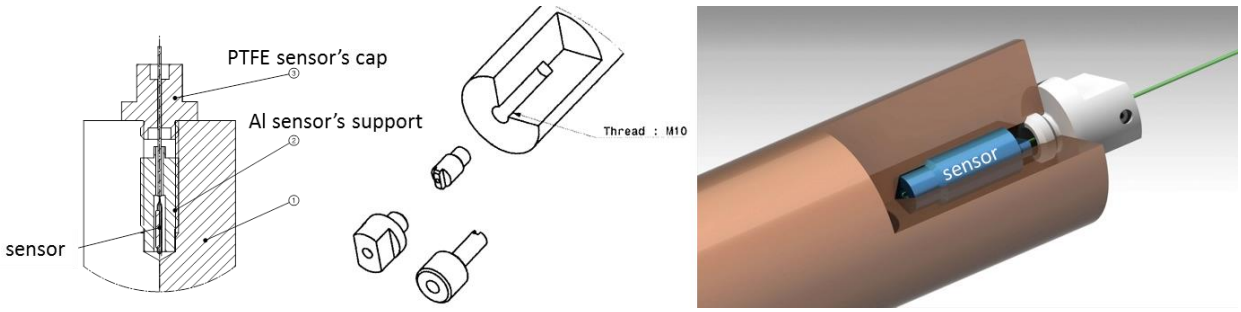

Fig. 7.8.4 – Temperature sensors configuration.

Fig. 7.8.5 – Temperature sensor.

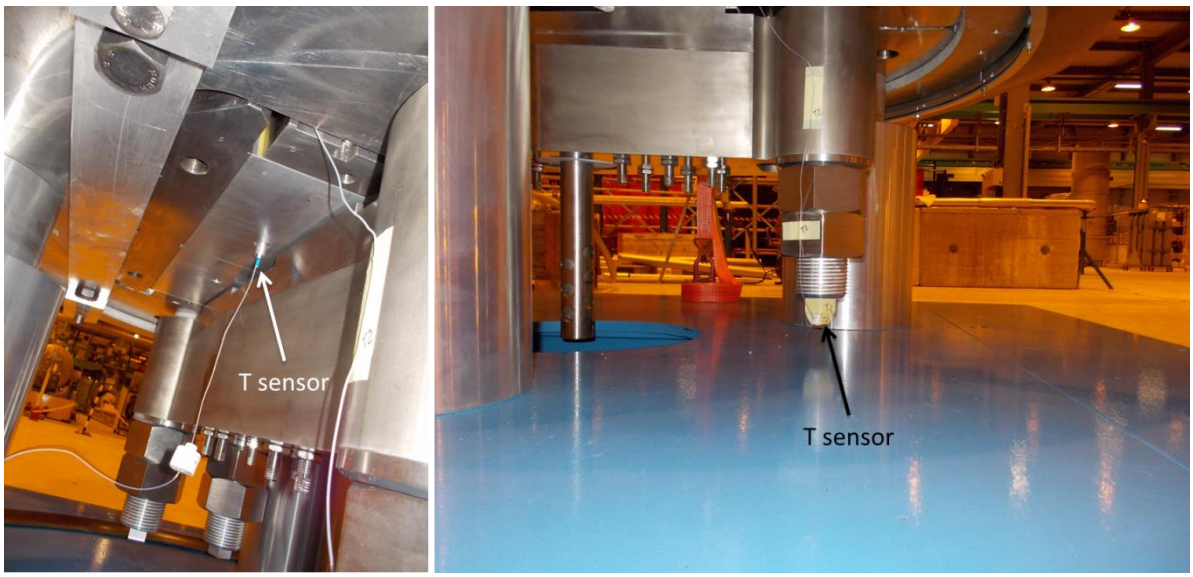

Fig. 7.8.6 – Temperature sensors at the bottom of the magnet structure: dummy and rod.

7.8.3 Instrumentation: external skin

In order to optimize the cooling time of the structure, additional external skin and joints have been assembled surrounding the magnet structure (Figure 7.8.7) to be used as thermal shield in order to limit the free flux space for the nitrogen in between the external skin and the magnet structure. Figure 7.8.8 shows the magnet structure instrumented and ready for the cool-down test.

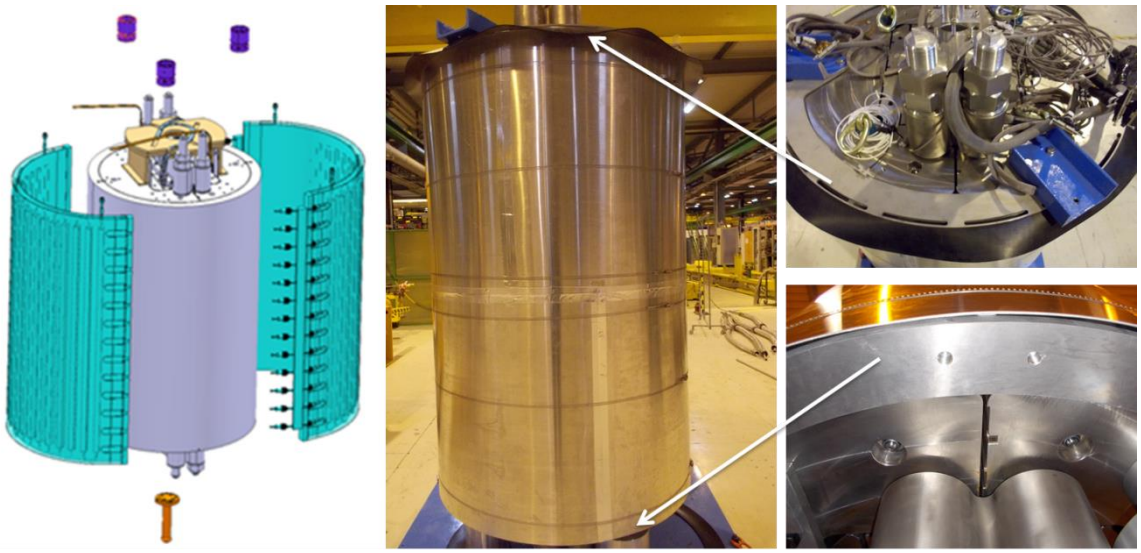

Fig. 7.8.7 – External skin surrounding the structure, and detail of the top and bottom joints.

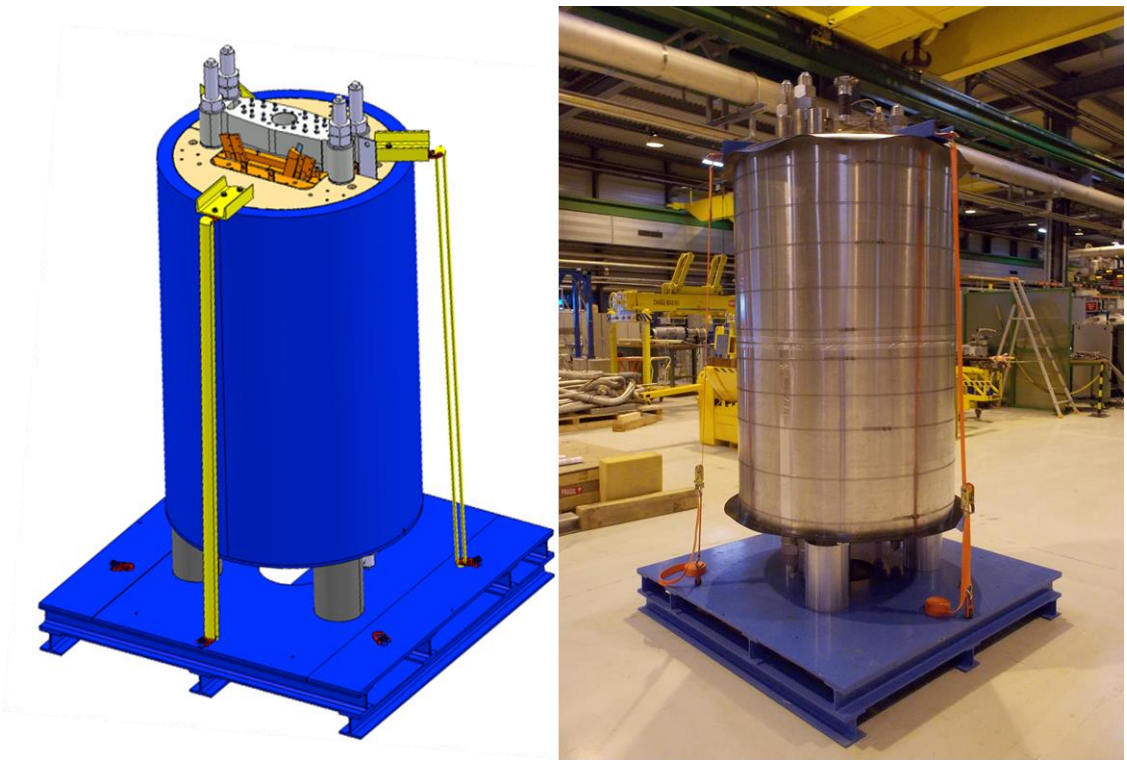

Fig. 7.8.8 – Magnet structure ready for cool-down test.

7.8.4 Facility for the cool-down test

A LN_2 Dewar vessel of Ø1.2m x 4m available at CERN will be used (Figure 7.8.9) for the cooling-down test. The magnet structure will be transported near the vessel and inserted in using a truck crane (Figure 7.8.10). A LN_2 transfer line will be inserted in the dummy aperture. The temperature sensors data acquisition system, cryogenic lines and cryogenic control system are ready. First cool-down test to 77K has been performed successfully.

Fig. 7.8.9 – Vessel of Ø1.2m x 4m for the cool-down test outside of SM18.

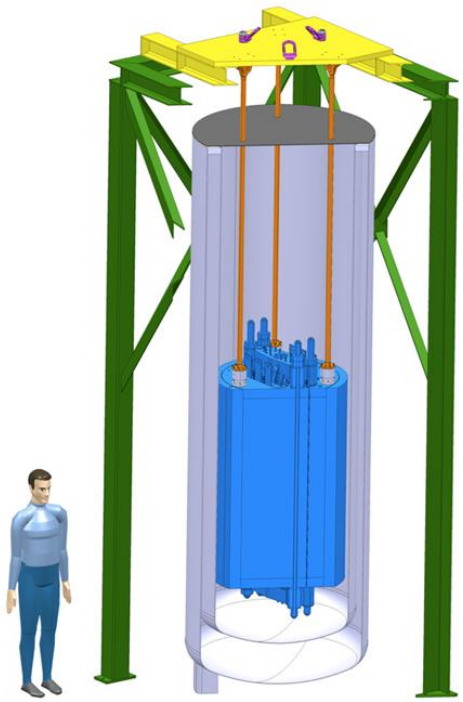

Fig. 7.8.10 – Magnet structure inside the vessel for the LN_2 test.

8. Conclusion

This report presents the design study of the FRESCA2 dipole magnet. This work has been done in the framework of the FP7-EuCARD-WP7-HFM collaboration.

The definition of the superconducting strand and cable and its characterization are described. All the aspects of the magnet study are reported: magnetic, mechanical, thermal design and protection in case of a quench.

Along the study, technological difficulties have emerged. They have led to additional analysis and to several experimental tests, which are extensively described in this document. Winding tests have helped to verify the practical feasibility of our design and to choose between technical options. Experimental test campaign has helped to understand the behavior of Nb_3Sn conductor during high temperature heat treatment and operation. Mechanical and assembly tests have been performed to validate the mechanical structure of the magnet.

In a near future, the winding tests will be completed and the winding tooling will be adapted to the conductor behavior during reaction. Two first Nb_3Sn coils will be assembled with two copper coils to form a magnet that will be inserted in the mechanical support structure. After the cold test of this magnet, two other Nb_3Sn coil will be fabricated to form the final FRESCA2 magnet, which will be cold-tested and qualified.

Acknowledgement

The MDWG wish to acknowledge every people who participated in one way or another in this study, at CERN and at CEA-Saclay: people from the design office and the workshops, and also all the colleagues who provided us with useful ideas and comments along this project.

We would like to stress the essential and constructive role of the ESAC committee members in guiding and advising wisely our decisions. We would also like to thank our colleagues from the EuCARD HFM work package project for the interesting interaction we have had with them. Finally, we would like to acknowledge the work of Shlomo Caspi from Berkeley as a temporary adviser to our project team.

The research leading to these results has received funding from the European Commission under the FP7 Research Infrastructures project EuCARD, grant agreement no 227579.

References

[0.1] EuCARD (grant agreement 227579) task 4 deliberable, “HTc insert design report”, 2013.

[1.1] Gijs De Rijk, "FRESCA2 magnet specification", version 3.1, https://espace.cern.ch/EuCARD/WP7/SWGroup/Shared Documents/FRESCA2_magnet_specification-v3.1.pdf

[1.2] T. Boutboul et al., "Nb_3Sn conductor development and characterization for NED", Journal of Physics: Confrence Series 97, 2008, 012211.

[1.3] P. Manil, F. Regis, J. Rochford, P. Fessia, S. Canfer, E. Baynham, F. Nunio, G. de Rijk, P. Védrine, “Magnetic design and code benchmarking of the SMC (Short Model Coil) dipole magnet”, IEEE Trans. Applied Superconductivity, vol. 20, issue 3, pp. 184-187, 2010.

[1.4] F. Regis, P. Manil, P. Fessia, M. Bajko, G. de Rijk, “Mechanical design of the SMC (Short Model Coil) dipole magnet”, IEEE Trans. Applied Superconductivity, vol. 20, issue 3, pp. 204-207, 2010.

[1.5] M. Bajko, B. Bordini, S. Canfer, G. Ellwood, J. Feuvrier, M. Guinchard, M. Karppinen, C. Kokkinos, P. Manil, A. Milanese, L. Oberli, J. C. Perez, F. Regis, G. de Rijk, “The SMC (Short Model Coil) dipole: an R&D program towards Nb3Sn accelerator magnets”, IEEE Trans. Applied Superconductivity, vol. 22, issue 3, ref. 4002704, 2012.

[1.6] M. Devaux-Bruchon, M. Durante, M. Karppinen, F. Kircher, P. Manil, A. Milanese, L. Oberli, J.C. Perez, J.M. Rifflet, G. de Rijk, F.Rondeaux, E. Todesco, "EuCARD-HFM dipole model design options", EuCARD-REP-2010-002, http://cds.cern.ch/record/1267962/files/EuCARD-REP-2010-002.pdf?version=4

[1.7] P. Manil, “FRESCA2 Dipole Version Tracker v4.4”, internal note, February 2013.

[3.1] L.T. Summers, M.W. Guinan, J.R. Miller and P.A. Hahn, “A model for the prediction of Nb3Sn critical current as a function of field, temperature, strain and radiation damage,” IEEE Trans. Magn., Vol. 27, issue 2, pp. 2041–2044, 1991.

[3.2] B. Bordini, “Self-Field Correction in Critical Current Measurements of Superconducting Wires Tested on ITER VAMAS Barrels”, CERN Internal Note 2010-38, EDMS Nr: 1105765, November 2010.

[4.1] L. Rossi and E. Todesco, “Electromagnetic design of superconducting dipoles based on sector coils”, Phys. Rev. ST Accel. Beams 10, 112401 (2007).

[4.2] L. Rossi and E. Todesco, “Electromagnetic efficiency of block design in superconducting dipoles”, IEEE Trans. Appl. Supercond. 19 (2009) 1186.

[4.3] S. Russenschuck, “Field Computation for Accelerator Magnets: Analytical and Numerical Methods for Electromagnetic Design and Optimization”, Wiley-VCH, March 2010.

[4.4] P. Manil, Magnet Design Working Group #24

[4.5] M. Devaux, Magnet Pre-design Working Group Meeting #9

[4.6] Magnet Design Working Group #2

[4.7] Magnet Design Working Group Meeting #10

[4.8] Vacuumschmelze, http://www.vacuumschmelze.com/index.php?id=1049&L=2, Soft Magnetic Cobalt-Iron-Alloys, VACOFLUX 48 • VACOFLUX 50, VACODUR 50 • VACOFLUX 17, 2001.

[4.9] A. Milanese, Magnet Pre-design Working Group Meeting #10

[4.10] M. Devaux, Magnet Design Working Group #22

[4.11] MDWG, EuCARD-HFM dipole parameters Geometry 3.4, internal note, November 2011.

[4.12] P. Ferracin, et al., “Recent Test Results of the High Field Nb3Sn Dipole Magnet HD2”, IEEE Trans. Appl. Supercond., vol. 20, no. 3, pp. 292-295, June. 2010.

[4.13] G. Ambrosio, et al., “Test Results of the First 3.7 m Long Nb3Sn Quadrupole by LARP and Future Plans,” IEEE Trans. Appl. Supercond. vol. 21, no. 3, pp. 1858-1862, June 2012.

[4.14] E. Todesco, et al., “Design studies for the low-beta quadrupoles for the LHC luminosity upgrade,” IEEE Trans. Appl. Supercond. 23 submitted for publication.

[4.15] H. Félice, et al., “Instrumentation and Quench Protection for LARP Nb3Sn Magnets,” IEEE Trans. Appl. Supercond., vol. 19, no. 3, pp. 2458-2461, June 2009.

[5.1] S. Caspi et al., “The use of pressurized bladders for stress control of superconducting magnets,” IEEE Trans. Appl. Supercond., vol. 11, no. 1, Mar. 2001, pp. 2272-2275.

[5.2] S. Pietrowicz, B. Baudouy, “Numerical study of the thermal behavior of an Nb3Sn high field magnet in He II”, Cryogenics, Volume 53, January 2013, Pages 72-77.

[5.3] De Rapper WM. Estimation of AC loss due to ISCC losses in the HFM conductor and coil, CERN TE-Note-2010-004; 2010.

[5.4] Pietrowicz S, Baudouy B. “Thermal design of an Nb3Sn high field accelerator magnet”, Adv Cryo Eng 57, AIP Conf Proc vol. 1434; 2012. p. 918–5.

[5.5] Baudouy B. Kapitza resistance and thermal conductivity of Kapton in superfluid helium. Cryogenics 2003;43:667–72.

[5.6] Pietrowicz S et al. Thermal conductivity and Kapitza resistance of cyanate ester epoxy mix and tri-functional epoxy electrical insulations at superfluid helium temperature. Cryogenics 2012;52(2–3):100–4.

[5.7] Baudouy B. Kapitza resistance and thermal conductivity of Kapton in superfluid helium. Cryogenics 2003;43:667–72.

[5.8] Baudouy B, Polinski J. Thermal conductivity and Kapitza resistance of epoxy resin fiberglass tape at superfluid helium temperature. Cryogenics 2009;49:138–43.

[5.9] Crycomp, 3.06 version. Florence (SC, USA): Cryodata Inc.

[5.10] Iwamoto A, Maekawa R, Mito T. Kapitza conductance of an oxidized copper surface in saturated He II. Cryogenics 2001;41:367–71.

[5.11] Iwamoto A, Maekawa R, Mito T. Kapitza conductance of an oxidized copper surface in saturated He II. Cryogenics 2001;41:367–71.

[5.12] M. Devaux, F. Debray, J. Fleiter, P. Fazilleau, T. Lécrevisse, C. Pes, J.M. Rey, J.M. Rifflet, M. Sorbi, A. Stenvall, P. Tixador, G. Volpini, “HTS insert Magnet Design Study”, IEEE Transactions of Applied Superconductivity, vol. 22 3, pp 4203605, 2012

[5.13] E. Härö, A. Stenvall, T. Lecrevisse, J-M. Rey, M. Sorbi, M. Devaux, C. Trophime, P. Fazilleau, G. Volpini, P. Tixador, F. Hornung, C. Pes,” Quench Considerations and Protection Scheme of High Field HTS Dipole Insert Coil”, IEEE Transactions of Applied Superconductivity, vol. 23, issue 3 , ref. 4600104, 2013.

[5.14] M. Sorbi, A. Stenvall, Protection working group #3